Ionization-based search for magnetic monopoles with NOvA Far Detector and probing scalar non-standard interaction of neutrinos at P2SO experiment

By

LIPSARANI PANDA

PHYS11201904004

National Institute of Science Education and Research, Bhubaneswar

A thesis submitted to the

Board of Studies in Physical Sciences

In partial fulfillment of requirements

for the Degree of

DOCTOR OF PHILOSOPHY

of

HOMI BHABHA NATIONAL INSTITUTE



May, 2026

Homi Bhabha National Institute[1]

Recommendations of the Viva Voce Board

As members of the Viva Voce Board, we certify that we have read the dissertation prepared by **Ms. Lipsarani Panda** entitled **"Ionization-based search for magnetic monopoles with NOvA Far Detector and probing scalar non-standard interaction of neutrinos at P2SO experiment"** and recommend that it may be accepted as fulfilling the thesis requirement for the award of Degree of Doctor of Philosophy.

S. N.	Composition	Name	Signature with date	In-Person/ Online
1.	Chairman	Prof. Bedangadas Mohanty	30/10/2026	In person
2.	Guide/Convener	Prof. Sanjay Kumar Swain	30/10/2026	In person
3.	Examiner	Prof. Poonam Mehta	Poonam Mehta 30/10/26	In-person
4.	Member - 1	Prof. Prolay Kumar Mal	Oct 30, 2026	In-person
5.	Member - 2	Prof. Amaresh Kumar Jaiswal		In-person
6.	Member - 3	Prof. Prafulla Kumar Behera	P. K. Behera 30/10/26	In Person

---

Final approval and acceptance of this thesis is contingent upon the candidate's submission of the final copies of the thesis to HBNI.

I/We hereby certify that I/we have read this thesis prepared under my/our direction and recommend that it may be accepted as fulfilling the thesis requirement.

Date: 30/10/2026

Place: NISER

Signature
Co-guide (if any)

Signature
Guide

[1] This page is to be included only for final submission after successful completion of viva voce.

STATEMENT BY AUTHOR

This dissertation has been submitted in partial fulfillment of requirements for an advanced degree at Homi Bhabha National Institute (HBNI) and is deposited in the Library to be made available to borrowers under rules of the HBNI.

Brief quotations from this dissertation are allowable without special permission, provided that accurate acknowledgement of source is made. Requests for permission for extended quotation from or reproduction of this manuscript in whole or in part may be granted by the Competent Authority of HBNI when in his or her judgment the proposed use of the material is in the interests of scholarship. In all other instances, however, permission must be obtained from the author.

LIPSARANI PANDA
Lipsarani Panda
Name & Signature of the Student

DECLARATION

I hereby declare that I am the sole author of this thesis in partial fulfillment of the requirements for a postgraduate degree from National Institute of Science Education and Research (NISER). I authorize NISER to lend this thesis to other institutions or individuals for the purpose of scholarly research.

LIPSARANI PANDA
Lipsarani Panda
Name & Signature of the Student

CERTIFICATION ON ACADEMIC INTEGRITY

Undertaking by the Student:

1. I Lipsarani Panda, HBNI Enrolment No. PHYS11201904004 hereby undertake that the Thesis, titled "Ionization-based search for magnetic monopoles with NOvA Far Detector and probing scalar non-standard interaction of neutrinos at P2SO experiment" is prepared by me and is the original work undertaken by me.

2. I also hereby undertake that this document has been duly checked through a plagiarism detection tool and the document is found to be plagiarism free as per the guidelines of the Institute/UGC.

3. I am aware and undertake that if plagiarism is detected in my thesis at any stage in the future, suitable penalty will be imposed as applicable as per the guidelines of the Institute/UGC.

Lipsarani Panda, 30.10.2026
Signature of the Student with date

Endorsed by the Thesis Supervisor:

I certify that the thesis written by the Researcher is plagiarism free as mentioned above by the student.

Signature of the Thesis Supervisor with date

Name: Sanjay Kumar Swain

Designation: Professor

Department/ Centre: School of Physical Science

Name of the CI/ OCC: NISER, Bhubaneswar

List of Publications arising from the thesis

Journal

1. "Ionization-based search for magnetic monopoles using the NOvA Far Detector", S. Abubakar et al. (The NOvA Collaboration), Phys. Rev. D 113, 112014 (2026).

2. "Study of scalar nonstandard interaction at the Protvino to super-ORCA experiment", Dinesh Kumar Singha, Rudra Majhi, Lipsarani Panda, Monojit Ghosh, Rukmani Mohanta, Phys. Rev. D 109, 095038 (2024).

Conference Proceedings

1. "Search for Fast Magnetic Monopoles with NOvA Far Detector", L. Panda and S. Swain for the NOvA Collaboration, Proceedings of the XXV DAE-BRNS High Energy Physics (HEP) Symposium 2022, HEPS 2022, Springer Proceedings in Physics, vol 304, 2024, pp. 1058–1060. doi: 10.1007/978-981-97-0289-3_287

2. "Search for Fast Magnetic Monopoles with NOvA Far Detector", L. Panda and S. Swain for the NOvA Collaboration, Proceedings of the 17th International Conference on Interconnections Between Particle Physics and Cosmology, PPC 2024. Springer Proceedings in Physics, vol 322, pp. 441-444.

Conferences

1. XXV DAE-BRNS High Energy Physics Symposium 2022,
   IISER Mohali, India; Dec. 12 - 16, 2022.
   Poster presentation: "Search for fast magnetic monopoles with NOvA far detector".

2. International Meeting on High Energy Physics (IMHEP-II),
   Institute of Physics (IOP), Bhubaneswar, India; Feb. 16 - 22, 2023.
   Oral presentation: "Search for fast magnetic monopoles with NOvA far detector".

3. American Physical Society (APS) April Meeting 2024,
   California, USA; April 3-6, 2024.
   Oral presentation: "Search for fast magnetic monopoles with NOvA far detector".

4. 17th International Conference on Interconnections between Particle Physics and Cosmology, IIT, Hyderabad, India; October 14-18, 2024.
   Oral presentation: "Search for fast magnetic monopoles with NOvA far detector".

LIPSARANI PANDA
Lipsarani Panda
Name & Signature of the Student

DEDICATIONS

”To my parents, sisters, brother and family”

ACKNOWLEDGEMENTS

I would like to express my heartfelt gratitude to all the people who played an important role throughout my Ph.D. journey with their guidance, support, and encouragement.

First and foremost, I sincerely thank my supervisor, Prof. Sanjay Kumar Swain, for accepting me into his research group and for his constant support throughout the course of this work. I am especially thankful for giving me the opportunity to work on a large international collaboration such as NOvA, as well as on the phenomenological analysis of neutrino oscillations, both of which have provided an invaluable learning experience for me.

I sincerely thank my doctoral committee members: Prof. Bedangadas Mohanty, Prof. Amaresh Kumar Jaiswal, Prof. Prolay Kumar Mal and Prof. Prafulla Kumar Behera, for their invaluable suggestions and feedback during each annual review, which greatly helped in shaping my scientific perspective and approach to research.

I extend my special gratitude to my Fermilab mentor, Dr. Matthew Strait, for his constant support and guidance in the monopole analysis. His valuable insights, encouragement, and patience throughout the course of this work have been extremely helpful for my understanding of the subject. I would also like to thank Prof. Alec Habig, Dr. Martin Frank, and Alex Antoshkin for several insightful discussions and their valuable inputs toward the monopole analysis.

I would also like to express my sincere gratitude to the Analysis and Paper Review Committee for the monopole analysis: Dr. Alex Sousa, Dr. Martin Frank and Dr. Liudmila Kolupaeva, Dr. Yagmur Torun and Sarah Chaote for their invaluable feedback, insightful suggestions, and careful review, all of which greatly shaped and strengthened the work presented in this thesis.

I sincerely thank Dr. Jonathan Paley for serving as my point of contact at Fermilab and for all the support and guidance I received during my stay there. I am also deeply grateful to Tom Weber, Karl Kaess, and Dr. Joshua Barrow for their invaluable guidance and support during the hardware work I contributed to NOvA detectors during my time at Fermilab. Their encouragement and expertise made my experience both enriching and rewarding.

I am deeply grateful to Prof. Rukmani Mohanta, Dr. Monojit Ghosh, Dr. Rudra Majhi,

and Dr. Dinesh Singha for giving me the opportunity to work on the phenomenological aspects of neutrino oscillations. Their continuous support and numerous discussions have greatly helped me in understanding this new area of physics.

I am thankful to my lab members, Dr. Tribeni Mishra, Dr. Chandiprasad Kar, Dr. Prafulla Saha, Dr. Aloke Kumar Das, Dr. Priyanka Sadangi, Amit, Kuldeep, Sneh, Sandeep, Rahul, Divya, Subrajit, Vatsal and Manas, for their constant encouragement, scientific discussions and for the many happy moments we shared during different outings and dinners. I would like to offer my special thanks to Rahul, Divya, and Subrajit for all the wonderful memories we created together through travelling, cooking, and countless conversations, especially during the final stage of my Ph.D. I am also sincerely grateful to my other friends at NISER: Ritwika, Subhadip, Debamalya, Sadaf and Soumik for their support.

I extend my special thanks to the colleagues I met at Fermilab. I am especially grateful to Dr. Biswaranjan Behera for his constant support throughout my Ph.D. journey. I would also like to thank my friends Barnali, Prachi, Bhumika, Shivam, Ishwar, Sayeed, and Prameet for making my stay at Fermilab truly memorable with their friendship and support. My deepest gratitude goes to Daniel for his unwavering support and encouragement during some of the most difficult times.

I express my heartfelt gratitude to my dearest friends, Swayam, Swayang, Mama, and Snigdha, who stood by me and supported me emotionally throughout these years. Their encouragement, understanding, and belief in me gave me the strength and motivation to continue during difficult times. This journey would not have been possible without their constant support and companionship.

Finally, I would like to express my deepest gratitude to my family, my parents, my sisters, my brother, and all my family members, for being the strongest source of love, strength, and support throughout my life. Their endless sacrifices, patience, encouragement, and unwavering belief in me gave me the courage to pursue my dreams even during the most difficult times. No words can truly express how grateful I am for their unconditional love and constant faith in me.

ABSTRACT

The first part of this thesis focuses on the search for magnetic monopoles, which remain among the most intriguing and elusive phenomena in modern physics. Although they are strongly motivated by theory and have been the subject of intensive experimental investigations for many decades, no particle with an isolated magnetic charge has yet been detected. Magnetic monopoles emerge naturally in various extensions of the Standard Model, particularly in grand unified theories (GUTs). The Monopoles predicted by GUTs are expected to be extremely massive, with typical masses around 10^{16} GeV, placing them far beyond the production capabilities of any foreseeable particle accelerator. Such particles could, however, have been generated in the early Universe and might persist today as relics within the cosmic-ray flux, which strongly motivates experimental searches for magnetic monopoles in cosmic radiation.

The NOvA Far Detector (FD), though primarily designed for neutrino oscillation studies, offers remarkable sensitivity for magnetic monopoles. In this thesis, we present a search for highly ionizing magnetic monopoles in the cosmic-ray flux using a 2,713-day dataset collected between 2015 and 2025 with the NOvA FD, a 14-kiloton segmented detector situated at the Earth's surface in Minnesota, United States. This analysis is sensitive to monopoles in a wide range of speeds $7 \times 10^{-4} < \beta < 0.995$, and can probe monopole masses up to 2×10^5 GeV for the fastest monopoles. No monopole signal is observed. Due to the large geometric acceptance of the detector and the minimal overburden, we obtained the most stringent flux limits to date in several regions of monopole speed and mass. For heavy monopoles with masses exceeding 10^{13} GeV that can reach the detector either from above or by traversing the Earth from below, We set a 90% confidence level upper limit on the flux of $\phi_{90\%} < 2 \times 10^{-16}\,\mathrm{cm^{-2}\,s^{-1}\,sr^{-1}}$ for monopole velocities in the range $0.005 < \beta < 0.8$. Over the same velocity interval, we also obtain a limit of $\phi_{90\%} < 8 \times 10^{-16}\,\mathrm{cm^{-2}\,s^{-1}\,sr^{-1}}$ for lighter monopoles with masses above 10^8 GeV that can reach the detector from above.

The second part of this thesis investigates the phenomenon of scalar non-standard interactions (NSI) in the context of the P2SO experiment and compares its sensitivity with that of DUNE. In particular, we examine the ability of these two experiments to constrain the

diagonal scalar NSI parameters, namely η_{ee}, $\eta_{\mu\mu}$, and $\eta_{\tau\tau}$, and analyze the impact of these parameters on the determination of the neutrino mass ordering, the octant of θ_{23}, and the CP violating phase δ_{CP}.

Our analysis reveals that the parameter Δm^2_{31} plays a nontrivial role when estimating bounds on $\eta_{\mu\mu}$ and $\eta_{\tau\tau}$ under the assumption that scalar NSI are absent in nature. We find that the sensitivities of P2SO and DUNE to constraining $\eta_{\mu\mu}$ and $\eta_{\tau\tau}$ are comparable, while DUNE exhibits a slightly better sensitivity to η_{ee}. Assuming the presence of scalar NSI in nature, we observe that the sensitivities to the neutrino mass ordering and to CP violation are predominantly affected by η_{ee}, whereas the octant sensitivity is primarily influenced by $\eta_{\mu\mu}$ and $\eta_{\tau\tau}$. These sensitivities can be either enhanced or degraded relative to the standard three-flavor oscillation scenario, depending on the relative signs of the scalar NSI parameters. With regard to the precision of the atmospheric mixing parameters, we find that the precision in the measurement of θ_{23} is significantly deteriorated in the presence of $\eta_{\mu\mu}$ and $\eta_{\tau\tau}$.

Contents

List of Figures 1

List of Tables 7

Chapter 1 Introduction to Magnetic Monopoles 9

1.1 Historical Background of Magnetic Charges 9
1.2 Magnetic Monopoles in Classical Electrodynamics 11
1.2.1 Extension to Magnetic Monopoles 12
1.2.2 Duality Symmetry Between Electric and Magnetic Fields 12
1.2.3 Field of a Static Magnetic Monopole 13
1.3 Dirac's Quantum Mechanical Approach to Magnetic Monopoles 14
1.4 Magnetic Monopoles in Grand Unified Theories 17
1.4.1 Properties of GUT Monopoles 18
1.5 Experimental Searches for Magnetic Monopoles 20
1.5.1 Searches in Cosmic Flux 20
1.5.2 Astrophysical and Cosmological Constraints on Monopole Flux . . 26
1.5.3 Monopole Searches at Colliders 29

Chapter 2 The NOvA Far Detector 33

2.1 NOvA Experimental Configuration 33
2.2 The Far Detector 34
2.2.1 The PVC Cell 34
2.2.2 Liquid Scintillator 36
2.2.3 Wavelength Shifting Fiber 37
2.2.4 Photodetector 38
2.2.5 PVC Extrusion Module 39
2.2.6 Front End Electronics 41
2.3 The Data Acquisition 44

2.3.1 The DAQ Data Formats . . . 45
2.3.2 DAQ Procedure . . . 47
2.3.3 Triggering . . . 47
2.4 Detector Calibration . . . 48
2.4.1 Attenuation Calibration . . . 48
2.4.2 Absolute Calibration . . . 50

Chapter 3 Simulation of Magnetic Monopoles 52

3.1 Isotropic Monopoles Generator . . . 53
3.2 Energy Loss Model . . . 56
3.2.1 Monopoles with $\beta \geq 0.1$ . . . 58
3.2.2 Monopoles with $\beta \leq 0.01$ . . . 59
3.2.3 Detector Response to Slow Signals . . . 59
3.2.4 Intermediate Velocity Region $(0.01 < \beta < 0.1)$ . . . 61
3.3 Light Yield by Magnetic Monopoles . . . 61
3.3.1 Ionization and Birks' Quenching Effect . . . 62
3.3.2 Cherenkov Radiation from Magnetic Monopoles . . . 63
3.4 Simulation of Photon Transport . . . 64
3.5 Simulation of Electronics Readout . . . 65
3.6 Overlay with Cosmics . . . 67
3.6.1 Event Display of Simulated Monopole Event . . . 67
3.7 Delta Rays and Crosstalk by Fast Monopoles . . . 69
3.7.1 Production of Delta Rays . . . 69
3.7.2 Crosstalk by Fast Monopoles . . . 72
3.8 Simulation of Background . . . 73

Chapter 4 The Ionization-Based Monopole Trigger 76

4.1 Ionization-Based Trigger . . . 76
4.1.1 Slicing . . . 77
4.1.2 Trigger Selection . . . 79
4.2 Trigger Efficiency . . . 82

4.3 Data Set and Live Time 84

Chapter 5 The Analysis Strategy 85

5.1 Reconstruction 85
5.1.1 3D Track Reconstruction 86
5.1.2 Reconstruction of Energy Deposition and Velocity 86
5.2 Reconstruction Performance 87
5.3 Reconstruction Validation 89
5.3.1 Reconstructed and True Track Length 89
5.3.2 Energy Deposition 90
5.4 Event Selection 90
5.4.1 Preselection Criteria 91
5.4.2 Final Selection Criteria 94
5.4.3 Overall Selection Efficiency 98
5.5 Estimation of Background in Signal Region 99
5.5.1 Cosmogenic Muon Bundles 99
5.5.2 Sideband Study 101
5.5.3 Estimation of Background for $\beta < 0.03$ 104
5.5.4 Validation of Background Estimates 106
5.6 Observation of Data in the Signal Region 106

Chapter 6 Results 109

6.1 Accessible Solid Angle 109
6.2 Projected Surface Area 112
6.3 Efficiency Factorization 113
6.4 Calculation of Flux Limit 113

Chapter 7 Neutrino Oscillation 118

7.1 Neutrinos in Standard Model 118
7.2 Neutrino Production and Detection 120
7.3 Evidence of Neutrino Flavor Oscillations 122
7.4 Neutrino Oscillation in Vacuum 124

7.4.1 Two Flavor Formalism . . . 125
7.4.2 Three Flavor Formalism . . . 126
7.5 Neutrino Oscillation in Matter . . . 129
7.6 Measurement of Oscillation Parameters . . . 131
7.7 Open Questions in the Neutrino Oscillation Sector . . . 133

Chapter 8 Probing Scalar Non-Standard Interactions at the P2SO Experiment 136

8.1 Introduction to Non-Standard Interaction . . . 136
8.1.1 Vector NSI Formalism . . . 137
8.1.2 Scalar NSI Formalism . . . 139
8.2 Simulation and Experimental Setup . . . 142
8.2.1 Experimental Setups . . . 142
8.2.2 GLoBES Simulation and Statistical Framework . . . 144
8.3 Oscillation Probabilities in the Presence of Scalar NSI . . . 146
8.4 Sensitivity to Scalar NSI . . . 149
8.5 Impact of Scalar NSI on Event Rates and Precision Measurements . . . 152
8.5.1 Effect on Event Spectra . . . 152
8.5.2 Effect on Precision Measurement of θ_{23} and Δm^2_{31} . . . 154
8.5.3 Sensitivity to Mass Ordering . . . 156
8.5.4 Sensitivity to CP Violation . . . 157
8.5.5 Sensitivity for Octant of θ_{23} . . . 159
8.6 Conclusion . . . 161

Chapter 9 Summary 163

References 166

List of Figures

1.1 Unification of the fundamental forces: at energies exceeding 100 GeV, the electromagnetic and weak interactions combine into the electroweak force, and they are further predicted to unify with the strong interaction at the GUT scale, approximately 10^{15} GeV. Figure adapted from Ref. [1]. 17

1.2 Upper bounds on the monopole flux with $\beta = 10^{-3}$ as a function of the catalysis cross section σ_{cat}. Figure is adapted from Ref. [2]. 25

1.3 The 90% CL upper limits on the flux of GUT monopoles as a function of velocity for magnetic charge $g = g_D$. The Parker bound is given by Equation 1.46, whereas the extended Parker bound (EPB) is defined by Equation 1.47. This figure is taken from Ref [2]. 28

1.4 Upper limits on the monopole production cross section derived from collider searches. All limits are quoted at the 95% CL, except for those from the E882 experiment, which are reported at the 90% CL. Dashed curves represent constraints obtained from indirect searches for monopoles trapped in beam pipe and other detector materials. This figure is taken from Ref [2]. . 30

2.1 Schematic of the NOvA detectors. Each detector uses a right-handed coordinate system centered on the front face with z along the length, y upward, and x across the width. The inset illustrates the internal structure of the detectors, where cells are arranged in alternating vertical and horizontal orientations. 33

2.2 Schematic of a PVC cell (L = 15 m, W = 3.9 cm, D = 6.6 cm) filled with liquid scintillator and a looped WLS fiber. 35

2.3 One NOvA detector cell with a looped WLS fiber shown in green. 37

2.4 Absorption and emission spectra of the dye in the WLS fiber. 38

2.5 Prototype NOvA APD installed on a carrier board. 38

2.6 Schematic diagram of (a) 16-cell extrusion module, (b) PVC module assembly with the end-plate located at the bottom and the fiber manifold positioned at the top. Vertical and horizontal modules have this same configuration [3]. 40
2.7 Schematic illustration of the front-end ASIC and the ADC used in the NOvA experiment. Signals from individual APD pixels are amplified, pulse-shaped, and then multiplexed in groups of 8 channels into a single ADC. 42
2.8 Digitized ADC samples fitted with the ASIC response function. The four labeled points correspond to the values that would be read out in DCS mode [4]. 44
2.9 Schematic overview of the NOvA DAQ system. 45
2.10 (a) Example attenuation fit for a detector cell using cosmic-ray data. (b) Detector response as a function of distance before and after calibration, demonstrating the removal of position dependence. 49
2.11 Corrected detector response per unit path length as a function of distance from the stopping point for (a) data and (b) simulation. 50
2.12 Simulated energy loss per unit length (dE/dx) as a function of distance from the stopping point. 50

3.1 Surfaces of simulated monopoles 54
3.2 The coordinates used for isotropic generation of monopoles. 55
3.3 Simulated event distributions as functions of (a) ϕ and (b) $\cos^2\theta$. The figures indicate that the simulated events are uniformly distributed in ϕ over the interval 0 to 2π, and uniformly distributed in $\cos^2\theta$ over the interval 0 to 1. 56
3.4 Energy loss plot from Groom's review 57
3.5 The time of traversal for monopoles to cross the FD as a function of their velocity and path length. 59
3.6 The collection rate of scintillation photons by the WLS fiber, as determined using a custom simulation [5]. 64

3.7 EVD of the simulated monopole with $\beta = 0.1$, overlaid with SNEWS cosmic activity. Individual hits are color-coded according to their ADC values. The monopole-induced hits appear as the two prominent red tracks in the EVD, corresponding to hits with comparatively high ADC values. 68
3.8 Transverse range a delta rays can travel produced from a monopole. 69
3.9 Simulation of monopole bundle of radius 2 cm (a) The entry points of the bundle on the surface of the detector, (b) The trajectory of the bundle in the FD, (c) Event display for monopole bundle of radius 2 cm. 71
3.10 Simulation of crosstalk 73
3.11 Simulated two-muon potential background 74
3.12 Simulated 5-muon potential background 74

4.1 Schematic flow of data processing before trigger decision. 78
4.2 Trigger efficiency as a function of monopole velocity. 83

5.1 Tracker performance vs. true velocity: (a) completeness in tracks and (b) purity in tracks. 88
5.2 Comparison of track length: (a) The relative difference between reconstructed and true track length, obtained by dividing their difference by the true track length, as a function of the true velocity, and (b) the absolute difference between reconstructed and true track length as a function of the true track length. The kink observed in this plot is associated with the dimensions of the FD. 89
5.3 Comparison of dE/dx and energy deposition vs. β 90
5.4 Distributions of the: (a) time difference between the first and the last hits, (b) log dE/dx, (c) mean ADC, (d) reconstructed track length. For each distribution here, all other selection requirements are imposed except for the variable shown in that plot. 92

5.5 Distributions of (a) off-track width and (b) width difference for data and the simulated signal sample. In each panel, the simulated event distribution is normalized in area to match the data. The left (right) distribution corresponds to events that pass the trigger and selection criteria 1–4 and 6 (1–5). The dashed vertical line with an arrow indicates the cut value of the variable; this cut is not applied to the events shown in the distributions. . . 95

5.6 Distributions of mean ADC for data and simulated signal events, shown for events with (a) $\beta_{\text{reco}} \geq 0.03$, and (b) $\beta_{\text{reco}} < 0.03$. In each plot, the simulated event distribution is area normalized to the data for visual comparison. In each case, trigger and selection requirements 1–6 have been applied. These plots are used to define the signal region. The dashed vertical line with an arrow indicates the cut value of the variable; note that this cut is not applied to the distribution shown. 96

5.7 Overall efficiency as a function of monopole velocity. 99

5.8 Illustration of the background estimation method: (a) the 2D distribution of mean ADC vs. width difference is partitioned into three distinct bands. In Band 1, the corresponding 1D mean ADC distribution is fitted with an exponential decay function, which is then extrapolated to Bands 2 and 3; and (b) indicate the normalization factor associated with the Band 1, as well as the validation and signal regions. 102

5.9 Distribution of the sideband sample used to estimate the background for $\beta \geq 0.03$: (a) presents the 2D distribution of events in Band 1, and (b) shows the corresponding 1D distribution of the mean ADC, which is fitted with an exponential function of the form defined in Equation 5.4. 103

5.10 Distribution of the sideband sample used to estimate the background for $\beta < 0.03$: (a) presents the 2D distribution of events in Band 1, and (b) shows the corresponding 1D distribution of the mean ADC, which is fitted with an exponential function of the form defined in Equation 5.4. 105

5.11 2D distributions of simulated events (represented as colored heatmaps) overlaid with unblinded fast-monopole–triggered data (red markers) for (a) $\beta \geq 0.03$ and (b) $\beta < 0.03$. No data events are observed within the signal region, which is indicated by the dotted box. 107

6.1 The solid curve shows the Earth's density profile as given in Ref. [6]; in this study, we adopt the simplified approximation indicated by the solid line. 110

6.2 Stopping power of the monopole in the five media it passes through before reaching the detector, Earth's mantle and core, detector overburden, scintillator, and atmosphere, as a function of β. The stopping power formulas used in this study is based on the Equations 3.8 and 3.10, with a smooth linear interpolation used in the intermediate velocity range. 111

6.3 (a) Solid angle coverage as a function of monopole velocity and mass. The coverage 4π means a monopole can arrive from any direction and still reach the detector, and (b) solid angle coverage as a function of shows monopole mass for specific monopole speeds, $\beta = 10^{-4}$, 10^{-3}, 10^{-2}, 10^{-1}, 5×10^{-1}, 8×10^{-1}, and 9×10^{-1}. 111

6.4 Flux limit as a function of (a) monopole velocity and mass, and (b) monopole velocity β for fixed monopole masses. This figure provides a graphical representation of the data listed in Table 6.1. 115

6.5 Upper limits on magnetic monopole flux for several experiments. In each region, the experiment with the strongest mass limit (least overburden) is shown above the others [7, 8, 9, 10, 11, 12]. Results from our search are shown in the regions labeled "This work." We report the most stringent limit, $\phi_{90\%} < 8 \times 10^{-16}$ cm^{-2}s^{-1}sr^{-1}, in the range $0.005 < \beta < 0.8$, corresponding to monopoles with masses greater than 10^9 GeV for all speeds, and greater than 10^7 GeV for $\beta > 0.1$. In the same range of β, for higher-mass monopoles capable of traversing the Earth, we set a flux limit $\phi_{90\%} < 2 \times 10^{-16}$ cm^{-2}s^{-1}sr^{-1}, corresponding to monopoles with masses greater than 10^{15} GeV and 10^{13} GeV for $\beta > 0.1$. 116

7.1 Overview of the particles of the Standard Model, grouped into fermions (quarks and leptons) and bosons (gauge bosons and the Higgs boson). Image adapted from the wikipedia [13]. 119
7.2 The impact of matter on the $\nu_\mu \to \nu_e$ oscillation probability for both neutrinos and antineutrinos in NOvA, illustrated for normal and inverted mass orderings, assuming $\delta_{CP} = 0$. Figure adapted from Ref. [14]. 131

8.1 Electron neutrino appearance (disappearance) probability as a function of energy for P2SO experiment in upper (lower) panel. 146
8.2 Electron neutrino appearance (disappearance) probability as a function of neutrino energy for DUNE experiment in upper (lower) panel. 147
8.3 Allowed values of Δm^2_{31} at 3σ CL when scalar NSI is fitted in the theory with the standard three flavour scenario in the data. 149
8.4 Bounds on the scalar NSI diagonal parameters ($\eta_{ee}, \eta_{\mu\mu}$ and $\eta_{\tau\tau}$) from DUNE and P2SO experiments. 151
8.5 Number of neutrino events as a function of neutrino energy in the DUNE experiment for (a) the appearance channel and (b) the disappearance channel. 153
8.6 Allowed region between $\sin^2\theta_{23} - \Delta m^2_{31}$ at 3σ CL in standard and in presence of scalar NSI parameters for DUNE and P2SO experiment. 154
8.7 Mass hierarchy sensitivity of the scalar NSI diagonal parameters ($\eta_{ee}, \eta_{\mu\mu}$ and $\eta_{\tau\tau}$) for the DUNE and P2SO experiments. 156
8.8 CPV sensitivity of the scalar NSI diagonal parameters ($\eta_{ee}, \eta_{\mu\mu}$ and $\eta_{\tau\tau}$) for DUNE and P2SO experiment. 158
8.9 Octant sensitivity of the scalar NSI diagonal parameters ($\eta_{ee}, \eta_{\mu\mu}$ and $\eta_{\tau\tau}$) for DUNE and P2SO experiments. 159

List of Tables

2.1 Constituents of the liquid scintillator in the NOvA detector, along with their functions and mass percentages (%). 36

3.1 The β values of simulated monopoles. 53
3.2 Properties of the NOvA scintillator used in the energy loss calculation. . . . 58

5.1 Summary of preselection criteria applied for track rejection in both signal and background samples. 93
5.2 Selection efficiencies for monopole bundles. In the first column, β represents the monopole velocity, and the values given in centimeters correspond to the maximum transverse ranges of the generated delta rays, which are equal to the radius of the monopole bundle within the custom simulation. . 97
5.3 Selection efficiencies with crosstalk 98

6.1 90% CL upper limits on the magnetic monopole flux in units of $10^{-16}\text{cm}^{-2}\text{s}^{-1}\text{sr}^{-1}$. *Heavy* denotes monopoles with masses above 10^{16} GeV that are capable of traversing the entire Earth. 114

7.1 Best-fit values of neutrino oscillation parameters from NuFIT 6.0 assuming normal mass ordering [15]. 133

8.1 The systematic uncertainties included in our analysis are listed here. "norm" denotes the normalization uncertainty, "Sig" refers to the signal, and "Bkg" refers to the background. 145
8.2 Oscillation parameter values with their corresponding 1σ errors considered in our analysis [16]. 148
8.3 Sensitivity limits on the scalar NSI parameters at 3σ CL from DUNE and P2SO experiment. 151

8.4 Appearance channel event difference for P2SO and DUNE for $\delta_{CP}^{\text{true}} = 90^o$. These events corresponds to 3 years running of P2SO and 6.5 year running of DUNE. 157

Chapter 1

Introduction to Magnetic Monopoles

This chapter is organized as follows. Section 1.1 presents the historical background of magnetic monopoles. Sections 1.2 and 1.3 provide a theoretical overview of the prediction of magnetic monopoles within the framework of classical and quantum mechanics, respectively. The emergence of magnetic monopoles in Grand Unified Theories (GUTs) is discussed in Section 1.4. Finally, Section 1.5 reviews in detail the experimental efforts to detect magnetic monopoles through novel detection techniques, both in cosmic-ray flux and in collider-based searches.

1.1 Historical Background of Magnetic Charges

Unlike electric charges, isolated magnetic charges, called magnetic monopoles, have not been observed experimentally; instead, magnetism always appears as paired north and south poles. In 1269, Petrus Peregrinus of Maricourt performed some of the early experiments with magnets. He introduced the term *polus* to describe the two ends of a magnet and observed that repeatedly cutting a magnet always produces smaller pieces with their own north and south poles, rather than isolated magnetic charges. From these observations he concluded that magnetic monopoles do not occur in nature as separate entities [17]. Further insights into magnetism came from navigation studies. In 1581, Robert Norman discovered the magnetic dip angle, demonstrating that the Earth's magnetic field influences the orientation of a compass needle. His observations were consistent with a field that resembled that of a dipole [18]. In 1600, William Gilbert published his landmark work *De Magnete*, in which he argued that the Earth behaves like a giant magnet [19]. This is often regarded

as the beginning of the scientific study of magnetism.

A series of experiments and theoretical advances by André-Marie Ampère and Michael Faraday showed that magnetic effects arise fundamentally from electric currents and from changing electric fields [20, 21]. This new understanding was later brought together and expressed in a unified way by James Clerk Maxwell in his electromagnetic field equations [22]. In Maxwell's classical theory, magnetic fields are always produced by electric currents or by time-varying electric fields, and truly isolated magnetic charges do not appear. Although Maxwell's equations are usually written under the assumption that magnetic charges do not exist, their mathematical form never rules them out. Even the existence of magnetic charge would restore symmetry in Maxwell's equations, a possibility first noted by Pierre Curie, when he proposed the existence of magnetic monopoles [23].

A major breakthrough occurred in 1931, when Paul Dirac showed that quantum mechanics not only allows for the possibility of magnetic monopoles but that if such objects exist, they would naturally explain why electric charges are always quantized in nature [24].

Magnetic monopoles are also predicted in GUTs. In 1974, 't Hooft and Polyakov demonstrated that monopoles arise naturally as topological solitons in certain gauge theories. In these models, monopoles are expected to have formed during symmetry breaking phase transitions in the early universe [25, 26]. Later developments in unification, including superstring theory and various higher dimensional models, also point to the existence of monopoles [27]. Given that many different theoretical frameworks predict the existence of magnetic monopoles, yet no experiment has confirmed their existence, it is essential that each time we probe a new high-energy regime we carry out dedicated searches for monopoles.

1.2 Magnetic Monopoles in Classical Electrodynamics

In classical electrodynamics, the fundamental sources of the electromagnetic field are electric charges and electric currents. In 1860, James Clerk Maxwell unified electricity and magnetism by formulating a set of equations that describe how electric and magnetic fields are generated and how they evolve. In modern high-energy physics, it is common to work in natural units $\hbar = c = 1$. In this convention, Maxwell's equations in vacuum can be written as follows:

$$\nabla \cdot \mathbf{E} = \rho_e, \tag{1.1}$$

$$\nabla \cdot \mathbf{B} = 0, \tag{1.2}$$

$$\nabla \times \mathbf{E} = -\frac{\partial \mathbf{B}}{\partial t}, \tag{1.3}$$

$$\nabla \times \mathbf{B} = \mathbf{J}_e + \frac{\partial \mathbf{E}}{\partial t}. \tag{1.4}$$

Here, **E** is the electric field, **B** the magnetic field, ρ the charge density, and **J** the current density.

Equation 1.2 states that the divergence of the magnetic field **B** vanishes everywhere, which expresses that there are no magnetic charges acting as sources or sinks of magnetic field lines. Instead, magnetic field lines always form closed loops or extend to infinity without starting or ending anywhere.

The asymmetry in Maxwell's equations is due to the existence of electric charges and the apparent absence of isolated magnetic charges. If magnetic monopoles were found to exist, the equations would become more symmetric between the electric and magnetic fields.

1.2.1 Extension to Magnetic Monopoles

In this section, we extend classical electrodynamics to include magnetic monopoles, yielding a more symmetric formulation of electromagnetism. To incorporate magnetic monopoles, consider the magnetic charge density ρ_m and the magnetic current density $\mathbf{J}_m$, analogous to the electric charge density ρ_e and the electric current density $\mathbf{J}_e$. The Maxwell equations then take the symmetrized form:

$$\nabla \cdot \mathbf{E} = \rho_e, \tag{1.5}$$

$$\nabla \cdot \mathbf{B} = \rho_m, \tag{1.6}$$

$$\nabla \times \mathbf{E} = -\frac{\partial \mathbf{B}}{\partial t} - \mathbf{J}_m, \tag{1.7}$$

$$\nabla \times \mathbf{B} = \mathbf{J}_e + \frac{\partial \mathbf{E}}{\partial t}. \tag{1.8}$$

In this generalized framework, electric and magnetic sources appear on an equal footing. The divergence equations allow flux to originate or terminate at isolated points, while the curl equations contain both electric and magnetic currents.

1.2.2 Duality Symmetry Between Electric and Magnetic Fields

In vacuum, in the absence of electric charges and currents, Maxwell's equations exhibit an exact symmetry under exchange of electric and magnetic fields,

$$-\mathbf{E} \leftrightarrow \mathbf{B}. \tag{1.9}$$

However, in real physical cases, this symmetry is explicitly broken because of the presence of only electric sources. By introducing both electric and magnetic charges and currents, one can restore this symmetry under an electromagnetic duality rotation by an angle θ:

$$\mathbf{E} \rightarrow \mathbf{E}\cos\theta + \mathbf{B}\sin\theta, \tag{1.10}$$

$$\mathbf{B} \rightarrow -\mathbf{E}\sin\theta + \mathbf{B}\cos\theta. \tag{1.11}$$

To make this duality an exact symmetry of the full theory and not just of the equations without sources, the sources themselves must transform in the same way as the fields.

$$\rho_e \leftrightarrow \rho_m, \qquad J_e \leftrightarrow J_m. \tag{1.12}$$

In this more complete picture, the magnetic charges behave just like electric charges; they can start or end magnetic field lines, the same way that electric charges start or end electric field lines. Similarly, a magnetic current can produce an electric field in much the same way that an electric current produces a magnetic field.

1.2.3 Field of a Static Magnetic Monopole

Consider a static point-like magnetic charge g located at the origin. The generalized Gauss's law for magnetism becomes

$$\nabla \cdot \mathbf{B} = g\,\delta^{(3)}(\mathbf{r}). \tag{1.13}$$

By spherical symmetry, the magnetic field must be radial,

$$\mathbf{B}(\mathbf{r}) = \frac{g}{4\pi}\frac{\mathbf{r}}{r^3}. \tag{1.14}$$

The total magnetic flux through a spherical surface that encloses the monopole is

$$\oint \mathbf{B} \cdot d\mathbf{S} = g, \tag{1.15}$$

demonstrating that the magnetic charge acts as a source of magnetic flux. The magnetic field of a monopole is formally analogous to the electric field of a point charge,

$$\mathbf{E}(\mathbf{r}) = \frac{e}{4\pi}\frac{\mathbf{r}}{r^3}. \tag{1.16}$$

Thus, the magnetic charge produces an inverse-square radial field identical in structure to Coulomb's law. This symmetry highlights the natural extension of classical electrodynamics to include magnetic monopoles.

1.3 Dirac's Quantum Mechanical Approach to Magnetic Monopoles

In quantum mechanics, electromagnetic interactions are described in terms of scalar and vector potentials, ϕ and $\mathbf{A}$, rather than directly through the electric and magnetic fields $\mathbf{E}$ and $\mathbf{B}$. The fields are obtained from the potentials via the following.

$$\mathbf{E} = -\nabla\phi - \frac{\partial \mathbf{A}}{\partial t}, \qquad \mathbf{B} = \nabla \times \mathbf{A}. \tag{1.17}$$

However, expressing the magnetic field as the curl of a vector potential appears to exclude the possibility of magnetic charge. This follows from a basic identity of vector calculus:

$$\nabla \cdot (\nabla \times \mathbf{A}) = 0, \tag{1.18}$$

which implies

$$\nabla \cdot \mathbf{B} = 0. \tag{1.19}$$

As a result, magnetic field lines cannot begin or end, ruling out the existence of magnetic monopoles.

In 1931, however, Dirac proposed an elegant explanation to resolve this apparent inconsistency [24]. He demonstrated that a vector potential corresponding to a magnetic monopole can be defined at the cost of introducing a singular line extending from the monopole to spatial infinity, commonly referred to as the *Dirac string*. Dirac illustrated this construction using an idealized solenoid that is extremely long and very thin, carrying a magnetic flux Φ. Outside the solenoid, the magnetic field is zero everywhere, except very

close to its two ends, while within the solenoid, the magnetic field is confined to its interior. If the solenoid length is considered to be much greater than its diameter, then, near one end, the magnetic field pattern looks just like the field created by a magnetic monopole. The corresponding effective magnetic charge associated with that end is then determined by the total magnetic flux that passes through the solenoid, which can be expressed as:

$$g = \Phi. \tag{1.20}$$

Mathematically, this configuration can be idealized as a single magnetic monopole located at one end point of an infinitesimally thin and arbitrarily long Dirac string. In this construction, the magnetic field takes the radial form

$$\mathbf{B}(\mathbf{r}) = g\frac{\mathbf{r}}{4\pi r^3}, \tag{1.21}$$

while a corresponding vector potential can be written as

$$\mathbf{A}(\mathbf{r}) = \frac{g}{4\pi r}\frac{\mathbf{r}\times\hat{\mathbf{k}}}{r-\mathbf{r}\cdot\hat{\mathbf{k}}}, \tag{1.22}$$

where $\hat{\mathbf{k}}$ is a unit vector along the direction of the string [28].

Consider an electrically charged particle of charge e moving in the vector potential $\mathbf{A}$ of a magnetic monopole with charge g. In quantum mechanics, the presence of the electromagnetic potential modifies the phase of the particle's wavefunction:

$$\psi(\mathbf{r}) \to \psi(\mathbf{r})\exp\left(ie\int_{\mathcal{C}}\mathbf{A}\cdot d\ell\right). \tag{1.23}$$

If the charged particle moves around a closed loop enclosing the Dirac string, the acquired total phase is

$$\Delta\phi = e\oint\mathbf{A}\cdot d\ell. \tag{1.24}$$

Using Stokes' theorem, this becomes

$$\Delta\phi = e\int(\nabla\times\mathbf{A})\cdot d\mathbf{S} = e\int\mathbf{B}\cdot d\mathbf{S}. \tag{1.25}$$

For a monopole enclosed by the surface,

$$\int \mathbf{B} \cdot d\mathbf{S} = g, \tag{1.26}$$

so that

$$\Delta\phi = eg. \tag{1.27}$$

The Dirac string of any magnetic monopole with a non-zero magnetic charge g would therefore generate a non-zero difference in the complex phase. Quantum mechanics, however, requires that the wavefunction be single-valued since two complex numbers whose phases differ by an integer multiple of 2π are physically indistinguishable. Therefore, the phase shift must be an integer multiple of 2π:

$$eg = 2\pi n, \qquad n \in \mathbb{Z}, \tag{1.28}$$

under which condition the Dirac string becomes unobservable and the electrically charged particle is sensitive only to the magnetic field of the monopole. Therefore, in quantum mechanics, the requirement that the string remain unobservable leads to a nontrivial constraint on electric and magnetic charges, known as Dirac quantization condition,

$$eg = 2\pi n, \qquad n \in \mathbb{Z}. \tag{1.29}$$

If there are several different kinds of electrically charged particles, then in order for the Dirac string to remain completely unobservable, the electric charge of every type of particle must satisfy Equation 1.29. This can only happen if the charge of any particle is an integer multiple of a basic unit of charge that satisfies Equation 1.29. Because we know from experiments that electric charge is actually quantized, Dirac showed that the existence of a single magnetic monopole anywhere in the universe would give a simple and elegant explanation for this quantization [24].

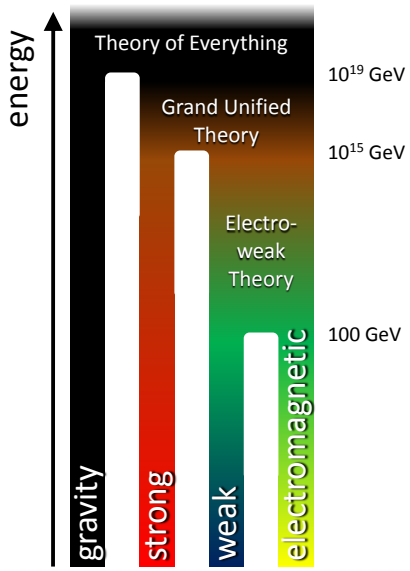


Figure 1.1: Unification of the fundamental forces: at energies exceeding 100 GeV, the electromagnetic and weak interactions combine into the electroweak force, and they are further predicted to unify with the strong interaction at the GUT scale, approximately 10^{15} GeV. Figure adapted from Ref. [1].

1.4 Magnetic Monopoles in Grand Unified Theories

GUTs aim to unify the strong, weak, and electromagnetic interactions into a single gauge group on extremely high energy scales (see Figure 1.1), typically around 10^{15}–10^{16} GeV [29]. At the energy scales of the early universe, the theory possesses a gauge symmetry. As the universe expands and cools, this large symmetry is spontaneously broken into smaller gauge groups, which correspond to the known fundamental forces. In recent decades, magnetic monopoles have drawn much interest due to their natural emergence in GUTs as stable, finite energy solutions associated with spontaneous symmetry breaking.

The first explicit finite-energy monopole configuration in a non-Abelian gauge theory was independently constructed by 't Hooft and Polyakov in 1974 [25, 26]. In this frame-

work, the $SU(2)$ symmetry is spontaneously broken to a residual $U(1)$ symmetry that can be identified with electromagnetism. In this broken symmetry phase, the theory admits a static, finite energy solution that corresponds to a magnetic monopole.

In contrast to the Dirac monopole, this configuration is completely regular and does not require the introduction of a singular Dirac string. At distances much larger than the monopole core, the associated magnetic field takes the asymptotic form

$$\mathbf{B} = \frac{g}{4\pi}\frac{\mathbf{r}}{r^3}, \tag{1.30}$$

which corresponds to the field of a point magnetic charge.

Any unified theory in which the electromagnetic U(1) is part of a larger gauge group that is broken by the Higgs mechanism will necessarily admit monopole-like field configurations [30]. In particular, a wide range of GUT models predict the existence of supermassive magnetic monopoles, with masses of order 10^{16} GeV, generated during symmetry breaking phase transitions in the early universe [27]. The properties of these monopoles are governed by the structure of the underlying gauge group and by the specific characteristic of its spontaneous symmetry breaking.

However, these supermassive GUT monopoles are far too heavy to be created in any current or foreseeable particle accelerator, since their production would demand extremely high energy. This limitation has motivated extensive experimental searches for monopoles in cosmic radiation using novel detector techniques, as discussed in more detail in Section 1.5.

1.4.1 Properties of GUT Monopoles

Mass

Magnetic monopoles predicted by GUTs are expected to be extremely massive because their mass is determined by the scale of symmetry breaking. A simple dimensional estimate

gives [27]

$$M_M \sim \frac{M_X}{\alpha}, \tag{1.31}$$

where M_X represents the mass scale of the heavy gauge bosons associated with the unified theory and α is the unified gauge coupling constant. This leads to monopole masses typically of order

$$M_M \sim 10^{16}\ \text{GeV (approximately 10 ng in SI units)}. \tag{1.32}$$

Charge

Another important property of monopoles is their large magnetic charge. Using the Dirac quantization condition defined in Equation 1.29 [24], the corresponding fundamental magnetic charge is given by

$$g_D = \frac{2\pi}{e} = \frac{e}{2\alpha}. \tag{1.33}$$

where α is the fine structure constant. Within this framework, the ionization strength associated with the Dirac magnetic charge g_D is equivalent to that of a particle that carries charge approximately $g_D/e = 1/(2\alpha) \simeq 68.5$ times the elementary electric charge.

Coupling Constant

In the presence of a magnetic monopole with magnetic charge g, the strength of the interaction between the monopole and the electromagnetic field is characterized by the monopole coupling constant. It is convenient to introduce a dimensionless monopole coupling constant α_m, defined in analogy with the fine structure constant $\alpha = e^2/(4\pi)$,

$$\alpha_m \equiv \frac{g^2}{4\pi}. \tag{1.34}$$

Using the Dirac quantization condition with $n = 1$, one finds

$$\alpha_m = \frac{1}{4\pi}\left(\frac{2\pi}{e}\right)^2 = \frac{\pi}{e^2} = \frac{1}{4\alpha} \approx 34.259, \tag{1.35}$$

The coupling α_m is large, indicating that the monopoles, if they exist, would interact strongly with magnetic fields.

1.5 Experimental Searches for Magnetic Monopoles

Since Dirac first demonstrated that a single magnetic charge could explain the observed quantization of electric charge, and with subsequent predictions of GUT monopoles, the search for these exotic particles has motivated an extensive and dedicated experimental effort over many decades. In this section, we summarize the main approaches used to search for magnetic monopoles, focusing on direct searches for GUT monopoles in cosmic fluxes, astrophysical and cosmological constraints on their flux, and accelerator-based production of intermediate mass monopoles.

1.5.1 Searches in Cosmic Flux

The energy required to produce GUT monopoles far exceeds the capabilities of existing or foreseeable accelerators, including the Large Hadron Collider (LHC). In particular, the required energies are estimated to be at least a trillion times greater than what can be achieved at the LHC [1]. As a result, it is widely believed that such monopoles could only have been produced in the early universe under extreme conditions [31]. Due to their expected stability, these relic monopoles may still persist today and could be observed as part of the cosmic radiation.

A variety of experimental strategies have been developed to search for such monopoles in cosmic flux. Among direct detection techniques, the most prominent include the induction method, ionization-based measurements, and searches for monopoles via catalysis of proton decay.

1. Cabrera's Monopole Event with Induction Detector

One of the most direct methods for detecting magnetic monopoles is based on electromagnetic induction. When a monopole traverses a superconducting loop, it induces a persistent current proportional to its magnetic charge. This technique was first demonstrated by Cabrera to detect magnetic monopoles using a superconducting detector [7].

To understand the principle of this detector, let us consider a magnetic monopole of charge g, moving with velocity v along the axis of a superconducting ring of radius r. Maxwell's equation in the presence of a magnetic current density is

$$\nabla \times \mathbf{E} + \frac{\partial \mathbf{B}}{\partial t} = -\mathbf{J}_m. \tag{1.36}$$

Integrating over a surface bounded by the ring and applying Stokes' theorem gives

$$\oint \mathbf{E} \cdot d\mathbf{l} + \frac{d\Phi}{dt} = -g\,\delta(t). \tag{1.37}$$

Since the contour lies within a superconducting loop, $\mathbf{E} = 0$, leading to

$$\frac{d\Phi}{dt} = -g\,\delta(t). \tag{1.38}$$

and,

$$\Phi(t) = -g\,\theta(t). \tag{1.39}$$

The total flux consists of the monopole contribution Φ_g and the induced supercurrent contribution, $\Phi_g = -LI(t)$, where $I(t)$ is the induced supercurrent and L the self-inductance of the ring. For a monopole moving along the symmetry axis:

$$\Phi_g(t) = \frac{g}{2}\left[1 - 2\theta(t) + \frac{\gamma v t}{\sqrt{(\gamma v t)^2 + r^2}}\right]. \tag{1.40}$$

The induced current is therefore:

$$I(t) = \frac{g}{2L}\left[1 + \frac{\gamma v t}{\sqrt{(\gamma v t)^2 + r^2}}\right]. \tag{1.41}$$

A magnetic charge g traversing a path that passes through the ring produces a net change in flux of two flux quanta, whereas a trajectory that does not intersect the ring results in no net flux change. The corresponding current is measured using a superconducting quantum interference device, which is capable of detecting extremely small variations in magnetic flux. This leads to a characteristic quantized signal associated with the passage of a monopole.

In 1982, Cabrera reported a single event consistent with the expected monopole signal, exhibiting a flux change close to the Dirac prediction. However, no subsequent experiments have confirmed similar events, and this observation remains unverified. Despite this, the superconducting induction method is still considered one of the most robust approaches for monopole searches, since the signal depends solely on the magnetic charge and is independent of the monopole's velocity, mass or energy loss mechanisms. Another important advantage of this technique is its sensitivity to monopoles with very low velocities.

However, the primary drawback of the superconducting induction approach is the achievable size of the detectors. It is technically challenging to construct systems large enough to probe the extremely low monopole fluxes expected in cosmic radiation. Because magnetic monopoles are anticipated to be extraordinarily rare, experimental searches demand very large detection volumes, often in combination with novel detection techniques and high exposure.

2. Ionization-based Searches

A widely used approach is based on the ionization energy loss of monopoles traversing matter. Due to their large magnetic charge, monopoles are expected to produce significant ionization and excitation, leaving distinctive signatures in detector materials. The energy loss is velocity dependent: magnetic monopoles with velocities in the interval $10^{-3} \leq \beta < 1$ predominantly dissipate energy via intense ionization. In the lower velocity range $10^{-4} < \beta <$

10^{-3}, they produce little ionization in the medium; however, they can still excite atoms and thus generate a detectable signal. Large-scale experiments using ionization-based detection techniques include scintillation detectors, Cherenkov detectors, nuclear track detectors and hybrid systems, which are described below.

Scintillation Detectors

Scintillation detectors measure the energy deposited by charged particles through light emission. Magnetic monopoles are expected to produce large ionization losses, resulting in intense light signals compared to minimum-ionizing particles. Experiments such as Monopole, Astrophysics and Cosmic Ray Observatory (MACRO) have used large arrays of scintillators to search for monopoles through energy deposition and time-of-flight measurements [9]. The NuMI Off-axis ν_e Appearance (NOvA) experiment, which is the main focus of this thesis, also uses scintillation detectors to search for magnetic monopoles over an extensive range of monopole speed [32, 33].

Cherenkov Detectors

Cherenkov detectors identify particles traveling faster than the phase velocity of light in a medium. The emission angle is given by:

$$\cos\theta_C = \frac{1}{\beta n}. \tag{1.42}$$

Relativistic monopoles produce enormous Cherenkov radiation as a result of their large effective charge. Large neutrino detectors such as IceCube [34] and Baikal [35] have performed dedicated searches using this technique.

Nuclear Track Detectors

Nuclear track detectors (NTDs) are passive solid-state detectors widely used in the search

for highly ionizing particles, including magnetic monopoles. When a highly ionizing particle passes through, it leaves invisible damage along its path. By chemically etching the plastic, these damaged zones grow into small cone shaped pits that can be seen with a microscope. The size and shape of the pit depend on how much energy the particle loses and how fast it moves, so different particles can be distinguished. Due to their high sensitivity to large ionization and low background, NTDs are particularly well suited for detecting slow-moving monopoles with large magnetic charge. They have been extensively used in experiments such as the MACRO and the Monopole and Exotics Detector at the LHC (MoEDAL) [36], where large-area detector arrays provide significant exposure for rare event searches.

To detect particles over a wide range of velocities, experiments such as MACRO used a combination of several detection methods, including scintillation counters, streamer tubes, and NTDs. The liquid scintillation counters measured the energy deposited by the particles and also recorded their arrival times. The limited streamer tubes served as tracking devices, allowing reconstruction of the trajectory of each particle as it passed through the detector. Finally, the NTDs registered permanent damage tracks produced by particles that ionize matter very strongly.

This multi-component design enabled searches for monopoles from relativistic to very slow velocities, with strong background rejection. Although no confirmed monopole events were observed, such experiments have set stringent limits on the monopole flux [9].

3. Catalysis of Proton Decay

An additional method for detecting magnetic monopoles is based on their ability to catalyze nucleon decay, known as the Rubakov-Callan effect [37, 38]. In certain GUT models [39, 40], monopoles can induce baryon number violating interactions when traversing matter, effectively triggering proton decay with a potentially large cross section.

In this framework, when a nucleon approaches the monopole, it can decay into lighter particles, for example:

$$p \to e^+ + \pi^0, \quad \text{or} \quad p \to \mu^+ + K^0, \tag{1.43}$$

while the monopole itself remains unchanged. As a result, a single monopole can catalyze multiple nucleon decays along its trajectory, producing a sequence of localized energy depositions approximately aligned along a straight path.

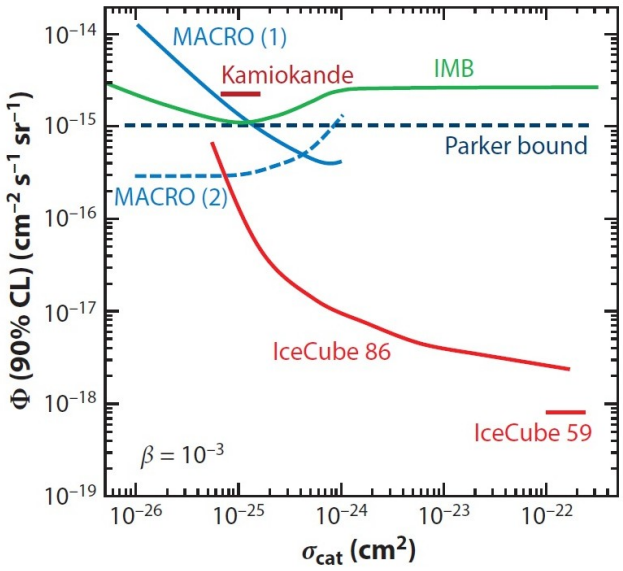


Figure 1.2: Upper bounds on the monopole flux with $\beta = 10^{-3}$ as a function of the catalysis cross section σ_{cat}. Figure is adapted from Ref. [2].

Despite extensive experimental efforts, no confirmed evidence of monopole-induced nucleon decay has been observed, and several experiments have instead reported stringent upper limits on monopole flux as a function of the cross section of nucleon decay, as illustrated in Figure 1.2.

Early proton decay experiments such as Soudan 1 [41], IMB [42], and Kamiokande [43] searched for such correlated event sequences and established limits on the monopole flux via the catalysis mechanism. The MACRO experiment [44] then performed a dedicated

search using its streamer tube subsystem, and the absence of candidate events was used to set stringent limits on both the monopole flux and the catalysis parameters.

In large neutrino telescopes, monopole-induced nucleon decays would generate Cherenkov radiation along the monopole trajectory, producing a characteristic pattern in the detector. Early searches were performed by the Baikal [35] experiment, while more recent searches by the IceCube [45] collaboration, including a dedicated slow-particle trigger in the DeepCore subdetector, have placed improved upper limits on the flux of non-relativistic monopoles.

An indirect search has also been carried out by the Super-Kamiokande [46] experiment, which looked for neutrino signals arising from proton decay catalyzed by monopoles captured in the Sun. This analysis set upper limits on the monopole flux of the order

$$\Phi_M \left(\frac{\sigma_0}{1\ \text{mb}}\right) < 6.3 \times 10^{-24} \left(\frac{\beta}{10^{-3}}\right)^2 \text{cm}^{-2}\,\text{s}^{-1}\,\text{sr}^{-1}, \tag{1.44}$$

at 90% Confidence Level (CL).

1.5.2 Astrophysical and Cosmological Constraints on Monopole Flux

Astrophysical considerations impose stringent constraints on the possible abundance of magnetic monopoles. In particular, the fact that monopoles have not been detected in cosmic-ray experiments sets direct upper bounds on their flux, whereas the presence of large-scale magnetic fields throughout the Universe imposes strong indirect constraints.

One of the most important theoretical limits is the *Parker bound*, which arises from the requirement that galactic magnetic fields persist on cosmological timescales [47]. Magnetic monopoles propagating through such fields experience a force

$$\mathbf{F} = g\mathbf{B}, \tag{1.45}$$

which accelerates them along the direction of the magnetic field. As a result, monopoles

gain kinetic energy at the expense of the magnetic field, effectively generating a magnetic current that drains energy from the field.

If the monopole flux were sufficiently large, this continuous energy extraction would lead to a rapid dissipation of the galactic magnetic field. However, observations indicate that the Milky Way possesses a magnetic field of the order of a few μG that has been sustained over billions of years. This implies that the rate at which monopoles extract energy must be smaller than the rate at which the field is regenerated by astrophysical processes.

From this argument, Parker derived an upper bound on the monopole flux in the Galaxy, given approximately by

$$\Phi_M \lesssim 10^{-15}\,\mathrm{cm}^{-2}\,\mathrm{s}^{-1}\,\mathrm{sr}^{-1}, \tag{1.46}$$

for monopoles with typical galactic velocities. The strength of this bound depends on the monopole mass: for very heavy monopoles ($M \sim 10^{17}\,\mathrm{GeV}$), gravitational effects dominate their dynamics, weakening the constraint, while lighter monopoles are more efficiently accelerated by magnetic fields and are therefore more tightly constrained.

A more stringent constraint, known as the *extended Parker bound* and derived by requiring the persistence of a primordial seed magnetic field [48], takes the form

$$\Phi_M \lesssim 1.2 \times 10^{-16} \left(\frac{M}{10^{17}\,\mathrm{GeV}} \right) \,\mathrm{cm}^{-2}\,\mathrm{s}^{-1}\,\mathrm{sr}^{-1}\,. \tag{1.47}$$

Experimental searches for monopoles in cosmic radiation have reached sensitivities approaching and, in some cases, surpassing the Parker bound. The current experimental limits on monopole flux as a function of velocity are shown in Figure 1.3.

Large underground detectors such as MACRO have provided some of the most stringent constraints over a wide range of monopole velocities [9], placing strong limits on the abundance of relic magnetic monopoles. These results are complemented by a variety of experiments that used different detection techniques and target materials.

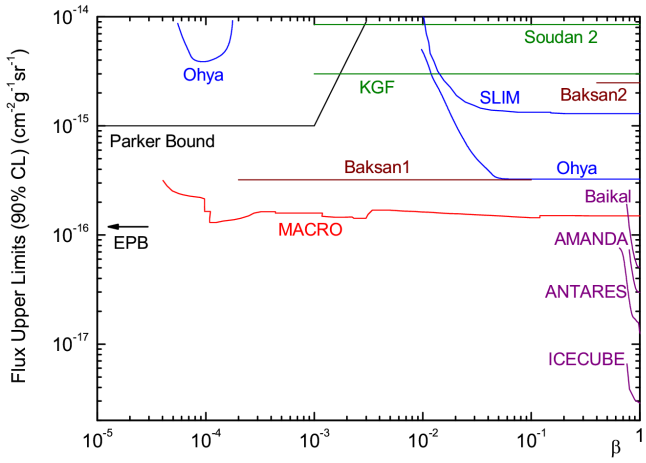


Figure 1.3: The 90% CL upper limits on the flux of GUT monopoles as a function of velocity for magnetic charge $g = g_D$. The Parker bound is given by Equation 1.46, whereas the extended Parker bound (EPB) is defined by Equation 1.47. This figure is taken from Ref [2].

Experiments such as Ohya [49] in Japan used extensive arrays of NTDs, while Baksan [50] in Russia used liquid scintillation counters. Tracking calorimeters, including Soudan 2 [51] in the United States and the Kolar Gold Fields (KGF) experiment [52]in India, provided additional sensitivity through detailed reconstruction of highly ionized tracks. The Search for Light Monopoles) (SLIM) experiment [8] at high altitude used a large NTDs array to search for intermediate-mass monopoles over an extended exposure period, further improving the coverage of accessible velocity ranges.

In parallel, large Cherenkov detectors originally designed for neutrino detection have also played an important role in monopole searches. Experiments including Baikal [53], Antarctic Muon And Neutrino Detector Array (AMANDA) [54], Astronomy with a Neutrino Telescope and Abyss environmental Research (ANTARES) [55], and IceCube [56] use the intense Cherenkov radiation generated by relativistic monopoles passing through transparent media such as water or ice.

A key challenge in these searches is the substantial background produced by cosmic-

ray muons. Implementing dedicated trigger strategies along with specific event selection criteria in experiments significantly enhances the sensitivity to monopole-induced signals.

1.5.3 Monopole Searches at Colliders

Although it is unrealistic for GUT monopoles to be produced at colliders, the possibility of lighter, intermediate-mass monopoles remains open. Such monopoles could be produced at current collider energies; however, their production cross sections are highly uncertain due to the non-perturbative nature of the interaction and are therefore strongly model dependent [57].

In addition, electroweak monopoles have been proposed within extensions of the Standard Model, with masses potentially accessible at existing collider energies, providing further motivation for dedicated experimental searches [58, 59, 60, 61].

Searches for monopoles at colliders differ significantly from conventional searches for new particles. In contrast to most hypothetical particles, which decay quickly, monopoles are predicted to be long lived and strongly ionizing because of their large magnetic charge. As a result, they are expected to produce clear, distinctive signals in detectors, such as heavily ionizing tracks or persistent currents if they become trapped in matter.

A wide range of collider experiments have searched for monopoles in different collision environments, including e^+e^-, ep, $p\bar{p}$, and pp interactions, and have reported upper limits on the monopole production cross section, as presented in Figure 1.4. These searches have primarily relied on scintillation counters, wire chambers, and NTDs, as well as indirect methods such as searching for trapped monopoles in detector material.

At the highest energies currently available, searches have been performed in pp collisions at the LHC. The A Toroidal LHC Apparatus (ATLAS) experiment has conducted dedicated searches for highly ionizing particles, looking for characteristic large energy deposits in the detector. No candidate events were observed, and the upper limits on the

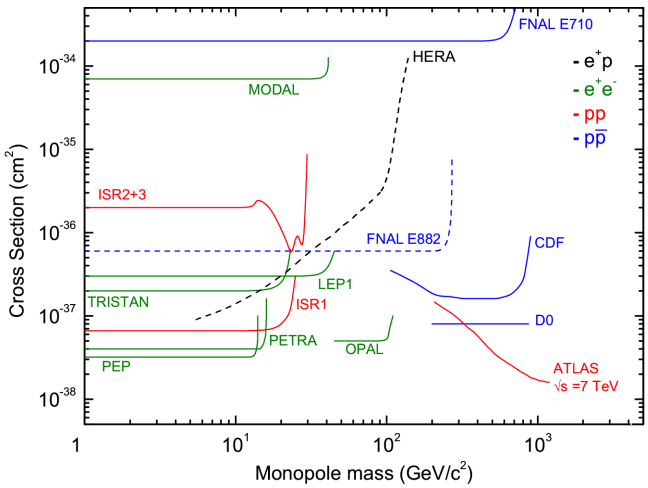


Figure 1.4: Upper limits on the monopole production cross section derived from collider searches. All limits are quoted at the 95% CL, except for those from the E882 experiment, which are reported at the 90% CL. Dashed curves represent constraints obtained from indirect searches for monopoles trapped in beam pipe and other detector materials. This figure is taken from Ref [2].

production cross section at a CL of 95% were set in the range of 16–145 fb for monopole masses between 200 and 1200 GeV [62]. The MoEDAL experiment at the LHC searches for highly ionizing particles such as magnetic monopoles using plastic NTDs around the LHCb interaction point, providing a passive and complementary detection method to the general purpose LHC detectors. It has set 95% CL limits on monopoles with masses up to about 4 TeV and charges up to $10\,g_D$, with production cross-section sensitivities of order 1 fb, and has not observed evidence of monopole production [63].

Searches have also been conducted in $p\bar{p}$ collisions at $\sqrt{s} = 1.96$ TeV in the Fermilab Tevatron. The CDF collaboration [64] searched for monopoles using drift chambers and time-of-flight scintillators, excluding monopole production cross sections above 0.2 pb for masses in the range $200 < M < 700$ GeV. The D0 collaboration [65] performed complementary searches by looking for high-energy photon pairs that could arise from virtual monopole loops. NTDs were also used in the E710 experiment [66] at Fermilab.

Earlier searches were carried out on e^+e^- colliders. At LEP, the OPAL experiment [67] searched for monopole pair production through the process

$$e^+e^- \to \gamma^* \to M\bar{M}, \tag{1.48}$$

using tracking detectors to identify highly ionizing tracks. No signal was observed and a CL upper limit of 95% of 0.05 pb was set for monopole masses in the range $45 < M < 104$ GeV. Additional searches in LEP included the MODAL experiment [68], which used CR39 NTDs, and other studies using Lexan detectors at the OPAL interaction point. Similar NTD-based searches were also performed in previous colliders e^+e^- such as TRISTAN (KEK) [69], PETRA (DESY) [70], and PEP (SLAC) [71].

Indirect searches have also been performed on the HERA e^+p collider by the H1 collaboration [72, 73], which investigated potentially trapped monopoles in the aluminum beam tube exposed to collisions at $\sqrt{s} = 300$ GeV. Similarly, the E882 experiment searched for monopoles trapped in the material surrounding the CDF and D0 detectors [74]. These studies involved passing samples through superconducting coils coupled to SQUID magnetometers, where a trapped monopole would induce a persistent current.

Despite extensive searches across multiple collider platforms, no confirmed evidence for magnetic monopole production has been found. Collider experiments continue to provide important constraints on intermediate-mass monopoles and complement cosmic-ray searches by probing controlled high-energy environments.

In summary, despite their strong theoretical motivation, magnetic monopoles have yet to be confirmed experimentally. Over the past decades, broad and complementary experimental efforts have been developed, including induction methods, ionization-based techniques, and nucleon decay catalysis searches, to probe both the monopoles predicted by GUT theories and lighter monopole candidates. Experimental efforts remain ongoing, targeting monopoles in cosmic radiation as well as those that might be produced at particle

colliders.

One such ongoing effort is the search for magnetic monopoles using the NOvA Far Detector. Due to its large size and location on the surface, the Far Detector possesses remarkable sensitivities for magnetic monopoles. This thesis focuses on this search, and in subsequent chapters we present a detailed description of the detector, the simulation framework, and the analysis strategy used to identify potential monopole signals.

Chapter 2

The NOvA Far Detector

This chapter provides a detailed technical overview of the NOvA Far Detector. The experimental setup and its physics objectives are presented in Section 2.1. A detailed description of the Far Detector and its constituent elements is given in Section 2.2, followed by an explanation of the data acquisition system and trigger scheme in Section 2.3. The chapter concludes with a discussion of the detector calibration procedure in Section 2.4.

2.1 NOvA Experimental Configuration

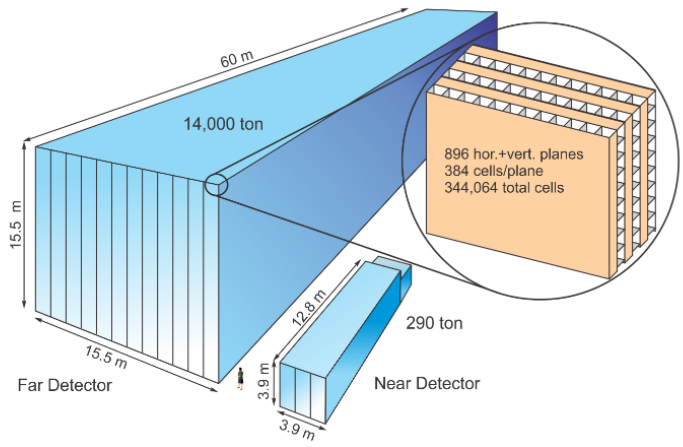


Figure 2.1: Schematic of the NOvA detectors. Each detector uses a right-handed coordinate system centered on the front face with z along the length, y upward, and x across the width. The inset illustrates the internal structure of the detectors, where cells are arranged in alternating vertical and horizontal orientations.

The NOvA experiment is a long-baseline neutrino oscillation experiment based at Fermilab, designed to probe the fundamental neutrino properties, including the neutrino mass ordering, leptonic mixing angles, and possible CP violation in the lepton sector. NOvA uses

two functionally identical, highly segmented detectors, known as the Near Detector (ND) and the Far Detector (FD). Each detector is constructed from planes of extruded polyvinyl chloride (PVC) cells that are filled with liquid scintillator. These planes are arranged in an alternating pattern of horizontal and vertical orientations, which enables three-dimensional (3D) reconstruction of the interactions. The ND, with a mass of 300 t, is located approximately 100 meters underground at Fermilab. The FD, considerably larger at 14 kt, is located on the surface near Ash River, Minnesota, at a distance of about 810 km from Fermilab. A schematic representation of the detector configuration is presented in Figure 2.1.

The FD is shielded by an overburden equivalent to 3.6 m of water, resulting in exposure to a cosmic ray flux of approximately 150 kHz. The overburden serves to shield the detector from cosmic rays and is constructed from concrete combined with a layer of loose barite (barium sulfate). Together, this system is equivalent to 9.86 feet of earth shielding. Because of its surface location with little overburden and large surface area, the FD offers exceptional sensitivity to relic magnetic monopoles. In this work, we analyze more than seven years of data collected by the FD in a search for highly ionizing monopoles. As a result, the remainder of this thesis will focus on the FD.

2.2 The Far Detector

The FD has an overall dimension of 15.5 m $\times$ 15.5 m $\times$ 59.8 m. It contains 896 planes with alternating horizontal and vertical orientations, with 384 PVC cells per plane, for a total of 344,064 detector cells.

2.2.1 The PVC Cell

It serves as the basic structural element of the FD: a rigid rectangular PVC cell containing liquid scintillator and a wavelength shifting (WLS) fiber. This setup is shown in Figure 2.2. Each PVC cell is 15 m long, 3.9 cm wide, and 6.6 cm deep, and is filled with liquid scintil-

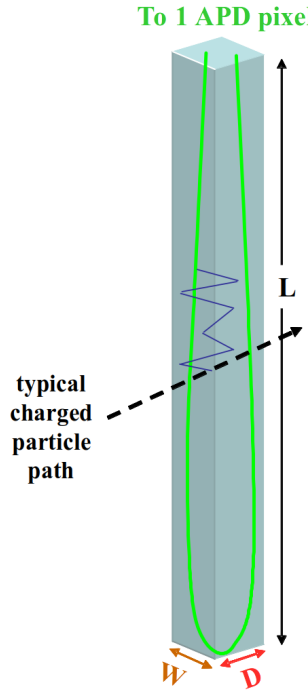


Figure 2.2: Schematic of a PVC cell (L = 15 m, W = 3.9 cm, D = 6.6 cm) filled with liquid scintillator and a looped WLS fiber.

lator.

When a charged particle passes through the cell, it produces scintillation light in the liquid. This light reflects multiple times inside the rectangular cell, until it is absorbed by the WLS fiber. The fiber runs the full length of the cell twice and is looped at the bottom, so the collected light is guided in both directions to the readout end (top of the PVC cell shown in Figure 2.2). In effect, the configuration behaves like two fibers in the cell, each with an almost perfectly reflecting end at the bottom, allowing nearly four times as much light to be collected as with a single non-reflecting fiber. At the readout end, both ends of the looped fiber are coupled to a single pixel of a 32-pixel array, where the light is converted into an electronic signal.

To further improve the efficiency of light collection, the PVC is doped with titanium

Component	Purpose	Mass Fraction
Mineral oil	Solvent	94.63%
Pseudocumene	Scintillator	5.23%
PPO	Wavelength-shifter	0.14%
bis-MSB	Wavelength-shifter	0.0016%
Stadis-425	Anti-static	0.001%
Tocopherol (vit. E)	Anti-oxidant	0.001%

Table 2.1: Constituents of the liquid scintillator in the NOvA detector, along with their functions and mass percentages (%).

dioxide (TiO_2), which improves its reflectivity by approximately 1%. Given that scintillation photons typically undergo, on average, eight reflections before entering the WLS fiber, this incremental increase in reflectivity results in an overall enhancement of roughly 8% in the detected light yield [3].

2.2.2 Liquid Scintillator

Approximately 63% of the FD mass is composed of liquid scintillators contained in the PVC cells, which corresponds to approximately three million gallons. The composition of the scintillator is summarized in Table 2.1. The scintillator is primarily mineral oil doped with 5% pseudocumene (1,2,4-trimethylbenzene), which serves as the main scintillating component and emits light with spectrum peaks between 360 and 390 nm. To better align with the absorption characteristics of the WLS fibers, additional chemical dopants are included to shift this emission into the 400–450 nm range.

Liquid scintillators of this kind typically suffer a $\sim$20% loss in light yield when exposed to oxygen. In NOvA, such a reduction is expected due to the gradual diffusion of oxygen through the PVC walls. However, the impact on detector performance is small because the scintillation light in each cell is collected locally by the WLS fiber over a short path length of approximately 1 m. To further limit degradation, the scintillator is mixed with tocopherol (vitamin E) as an antioxidant.

In addition, the liquid scintillator is strongly nonconductive and can accumulate net electric charge via triboelectric effects during flow, which in turn can cause spark discharges between the liquid and its container. To address this issue, the scintillator mixture includes Stadis-425, an antistatic additive that increases the conductivity to a safe range.

2.2.3 Wavelength Shifting Fiber

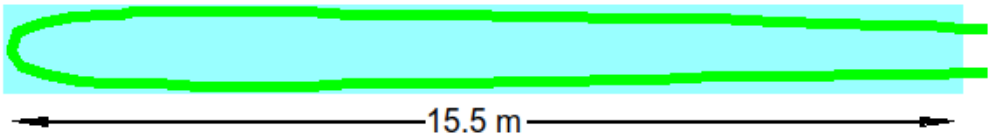


Figure 2.3: One NOvA detector cell with a looped WLS fiber shown in green.

The WLS fiber has a length of about 33.5 m and a diameter of 0.7 mm, and is looped at one end of the PVC cell, as shown in Figure 2.3. At the other end of the cell, both fiber ends are connected to a single APD pixel.

The fiber consists of a polystyrene core (refractive index n = 1.59) doped with 300 ppm of R27 dye, which serves as a wavelength shifter. It is surrounded by an acrylic inner cladding (n = 1.49) and an outer fluorinated polymer cladding (n = 1.42). Double cladding, with refractive indices lower than that of the core, enhances light capture through total internal reflection and improves transmission efficiency. In addition, both cladding layers are insoluble in pseudocumene, providing a double barrier against scintillator penetration into the fiber core and thus ensuring long–term fiber performance in the detector environment.

The charged particle primarily produces scintillation light in the blue region. This light is collected by the WLS fiber, where the fluorescent dye shifts it from blue (400–450 nm) to green (490–550 nm). A portion of the light emitted by the dye is trapped within the

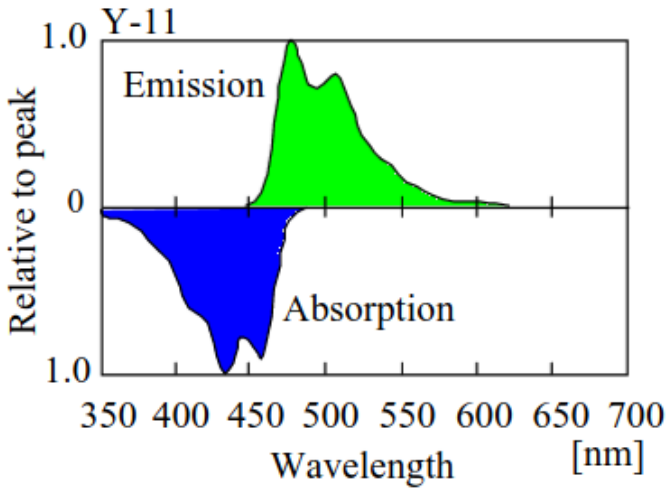


Figure 2.4: Absorption and emission spectra of the dye in the WLS fiber.

fiber by total internal reflection. As light travels through the fiber, much of the shorter-wavelength component (< 500 nm) is reabsorbed due to the overlap between the absorption and emission spectra of the dye (see Figure 2.4), while the longer-wavelength component is only weakly attenuated. Therefore, a photodetector with high quantum efficiency at these red wavelengths is required, which is exactly where APD performs best.

2.2.4 Photodetector

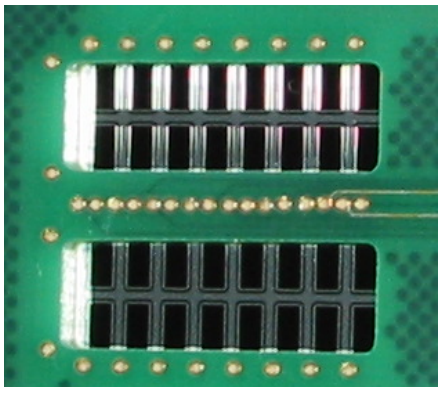


Figure 2.5: Prototype NOvA APD installed on a carrier board.

The photodetectors used in the NOvA experiment are the APDs, which are arranged in 32-pixel arrays (see Figure 2.5) and each pixel is designed to accommodate light from two fiber ends. The 32 channels correspond directly to the 32 cells of a single PVC extrusion module, ensuring a compact and efficient readout architecture.

A major advantage of using APDs is their high quantum efficiency and relatively uniform spectral response. In the wavelength range relevant for the emission of the WLS fiber (approximately 500–550 nm), the quantum efficiency of the NOvA APDs reaches about 85%. This high efficiency allows the use of long scintillator cells without a significant loss of signal, thereby reducing the total number of readout channels required. These features make APDs particularly well suited for large-scale, high-granularity detectors such as NOvA.

The working principle of an APD is based on the conversion of incident photons into an electrical signal followed by internal amplification. Incoming light is absorbed in the depletion (collection) region, where it generates electron–hole pairs. Under the influence of an applied electric field, the electrons drift toward the high-field p–n junction. In this region, the electric field is sufficiently strong to initiate impact ionization, resulting in avalanche multiplication of charge carriers. The gain of the device depends on the electric field strength and the mean free path between ionizing collisions, both of which are sensitive to temperature.

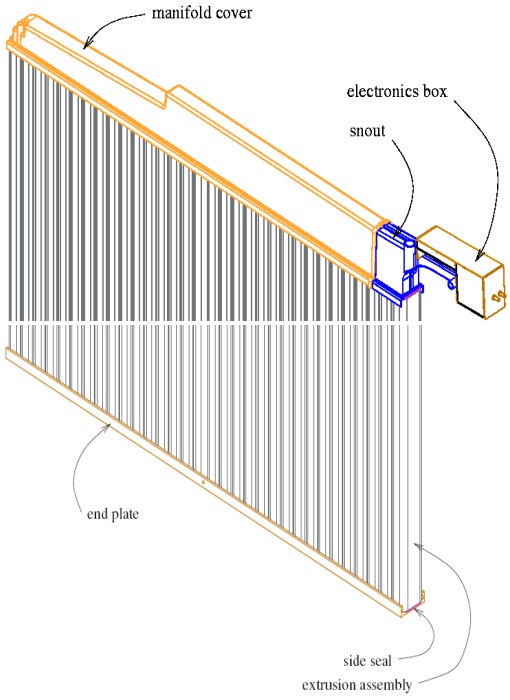
2.2.5 PVC Extrusion Module

The PVC extrusion modules form the fundamental building blocks of the NOvA detectors, providing both mechanical support and defining the detector geometry. In the FD, approximately 4.5 kilotons of PVC are used, accounting for about 30% of the total detector mass.

Each PVC extrusion has a cellular structure, with 16 cells formed in a single extrusion, as illustrated in Figure 2.6a. Detector modules are built by bonding two such 16-cell extru-



(a)



(b)

Figure 2.6: Schematic diagram of (a) 16-cell extrusion module, (b) PVC module assembly with the end-plate located at the bottom and the fiber manifold positioned at the top. Vertical and horizontal modules have this same configuration [3].

sions together to create a 32-cell unit, as illustrated in Figure 2.6b. These modules are then arranged into planes, with consecutive planes alternating between vertical and horizontal orientations (see Figure 2.1). All extrusions in the FD have a length of about 15 m. The WLS fiber is inserted along the length of each cell to collect scintillation light. Therefore, each module consists of a 32-cell extrusion assembly, an end plate, and a fiber manifold. In total, approximately 13,000 such modules are used in the Far Detector.

In each module, WLS fibers coming from 32 cells pass through the fiber manifold, and the two fiber ends from every cell are optically connected to one pixel of a 32-pixel APD array. The manifold serves several important functions: it guides the fibers to the connectors, protects them from excessive bending, shields them from external backgrounds, such as cosmic rays, and provides the interface to the APD readout system. Identical manifold designs are used for both vertical and horizontal modules.

2.2.6 Front End Electronics

The primary role of the front-end boards (FEBs) is to receive the light signals detected by the APDs and convert them into digital information. This involves amplifying the signals, determining their amplitude and timing, and providing this information to the data acquisition (DAQ) system, which is discussed in more detail in the following section. The FEBs operate continuously and record data without the need for an external trigger.

To enhance the sensitivity to the small signals from long WLS fibers in the FD, NOvA designed a custom application specific integrated circuit (ASIC). Each of the 32 APD pixel outputs is connected to an individual low-noise preamplifier, which increases the small current signals while preserving its shape. The amplified signals are then sent through a pulse-shaping stage that broadens and smooths the waveform, making it easier to distinguish it from electronic noise. Following this shaping, signals from sets of eight channels are multiplexed, sequentially merged into a single output stream, and sent to an external commercial

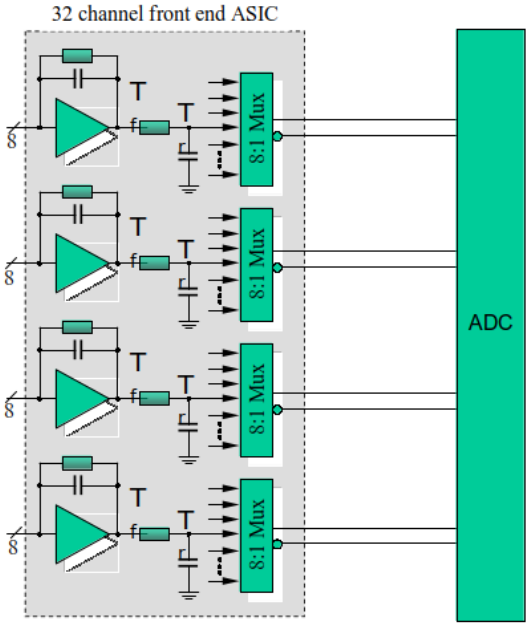


Figure 2.7: Schematic illustration of the front-end ASIC and the ADC used in the NOvA experiment. Signals from individual APD pixels are amplified, pulse-shaped, and then multiplexed in groups of 8 channels into a single ADC.

Analog to Digital Converter (ADC). A schematic representation of the layout is shown in Figure 2.7. The analog signals are digitized by the ADC with high precision, ensuring that even very low-amplitude pulses are captured for subsequent digital processing.

In addition to the front-end ASIC and the ADC, a field programmable gate array (FPGA) is used to perform digital signal processing. The FPGA plays a central role in extracting useful information from the raw signals by suppressing noise and reconstructing both the timing and amplitude of the detected signals. In particular, a dual correlated sampling (DCS) technique is applied to reduce low-frequency noise. Signals that exceed a predefined threshold are identified as physical hits, time-stamped, and transmitted to the DAQ system for further processing.

Noise Suppression with DCS Technique

The FEB operate with a clock period of 15.625 ns. Each channel is digitized once every 32 clock cycles, corresponding to a sampling interval of 500 ns. As a result, each APD channel produces a sequence of ADC measurements, denoted as ADC_i, at regular 500 ns intervals. To suppress noise, the FPGA computes the DCS value using two samples defined as

$$DCS_i = ADC_{i+3} - ADC_i, \tag{2.1}$$

where the samples are spaced by three intervals, corresponding to 1500 ns.

If the calculated DCS_i exceeds a channel-dependent threshold, typically in the range of 40–50 ADC counts, the signal is identified as a valid hit and the corresponding data segment is called a *nanoslice*. A nanoslice contains the information about a hit, recording its time, series of ADC samples, cell ID, and cell status.

Signal Processing

To extract the timing and amplitude of each nanoslice, the ADC samples are fitted with a known pulse shape, producing the pulse's peak ADC and time. The amplified signal is modeled by the function

$$A(t) = \text{Norm}\, F\, I \left[\frac{e^{-(t-t_0)/F}}{(I-F)(F-R)} - \frac{e^{-(t-t_0)/I}}{(I-F)(I-R)} + \frac{e^{-(t-t_0)/R}}{(I-R)(R-F)} \right] + B, \tag{2.2}$$

where R = 420 ns is the rise time, F = 10, 373 + 2.4 ADC ns is the fall time, I = 112, 557 ns is pre-amplifier fall time, t_0 is the cell hit start time, B is the average noise baseline of the channel, and Norm is an overall normalization constant proportional to the energy deposition of the hit and related to the position of the hit in the cell.

At least four ADC sample points are required to perform this fit. While using more samples would typically enhance the quality of the fit and improve parameter resolution, constraints from DAQ bandwidth and available data storage prevent recording additional

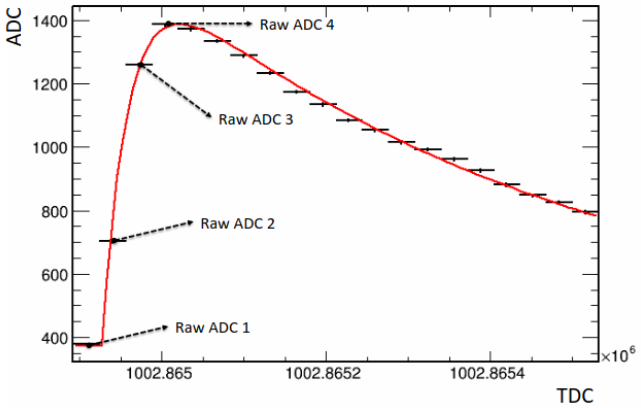


Figure 2.8: Digitized ADC samples fitted with the ASIC response function. The four labeled points correspond to the values that would be read out in DCS mode [4].

samples. Of the four ADC samples, one corresponds to the baseline, and the remaining three are positioned along the response curve, as shown in Figure 2.8.

2.3 The Data Acquisition

The main role of the NOvA DAQ system [75, 76] is to collect data from all APD channels and turn them into a continuous stream that can be processed and stored. Figure 2.9 presents a schematic overview of this system.

The nanoslices produced by the FEBs are sent to the data concentrator modules (DCMs), which ensure that only signals above a certain threshold are passed on. Each DCM takes serial data from up to 64 FEBs, merges and formats these data into packets, and sends them to the buffer nodes. The DAQ system then uses an intermediate buffer stage, where data can be held temporarily while trigger decisions are made.

Online trigger processors look at the buffered data stream, using accurate time stamps to find clusters of hits that are likely to come from interesting physical events. Only data that pass these trigger conditions are kept for long-term storage and further offline analysis.

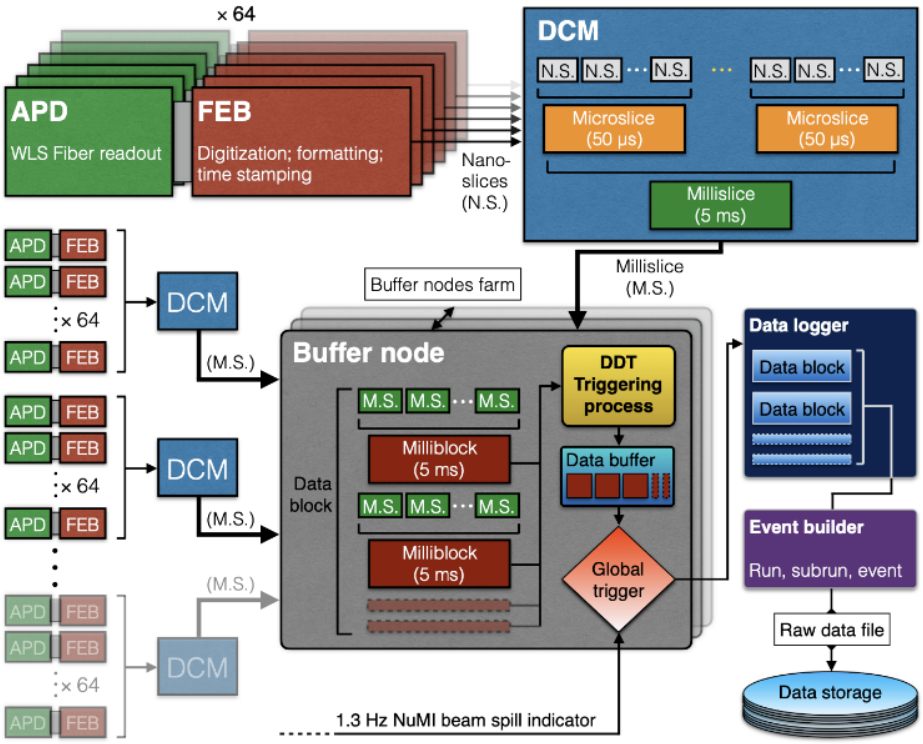


Figure 2.9: Schematic overview of the NOvA DAQ system.

2.3.1 The DAQ Data Formats

The NOvA experiment uses a structured raw data format built as a hierarchical sequence of distinct data blocks produced at successive stages of the DAQ chain, as illustrated in Figure 2.9. The overall layout of these data formats is characterized in terms of the basic data unit defined at each processing stage. The higher-level formats enclose the lower-level units in a compact form, and their ordering can be described as follows.

- Nanoslice – the data format generated by a FEB that includes both pulse height and timing details. This format is used to send data to the DCM.
- Microslice – this represents a 50 μs set of individual nanoslices in the DCM to produce a properly synchronized time window that is approximately 5 µs in length.

- Millislice – the millislice consists of a block containing approximately 8–9 kB of microslices, organized in the format needed to transfer data between the DCMs and the buffer nodes.

- MilliBlock – the collection of milslices acquired from all DCMs over a 5 ms time, i.e., 5 ms of full detector activity.

- Data Block – the trigger condition is applied, and data satisfying the corresponding selection criteria are aggregated into data blocks. These data blocks are assigned unique identifiers in terms of run, sub-run, and event numbers, formatted into raw data files, and ultimately transferred to the designated long-term storage system.

- Trigger – This information specifies the trigger type, the origin of the trigger, the time at which it was generated, and the corresponding time window of interest.

- Event – An event is a data structure that captures the detector's activity over a defined time interval. The length of this interval is determined by the specific trigger that starts the event acquisition. A fully defined event includes the entire set of trigger-related metadata, the corresponding timing information, and all data blocks falling within the trigger's time window of interest.

- Subrun – A subrun is a segment of data within a run. A new subrun begins whenever the largest data stream reaches 1 GB within a one-hour period. If no stream reaches 1 GB during that hour, a new subrun is still started at the end of the hour.

- Run – A run is a stored collection of events recorded over a given time interval, along with basic information about the detector and the data-taking configuration. Once 64 subruns have been created within a single run, a new run is automatically initiated.

2.3.2 DAQ Procedure

Each FEB gathers nanoslices from its 32 channels, and the data from as many as 64 FEBs are digitized and transmitted to a DCM in 50 µs microslices. A DCM then combines the microslices from up to 64 FEBs into a single millislice, representing 5 ms of data for that DCM. Aggregating the millislices from all DCMs yields a milliblock, which captures the full detector readout over a 5 ms window. This milliblock is transferred from the DCMs to a set of buffer nodes: the first 5 ms of data from every DCM go to one node, the next 5 ms to a second node, and so on. After each node has received one milliblock, the cycle restarts, and new milliblocks overwrite the oldest ones. Each buffer node examines its milliblocks using data-driven trigger conditions to determine whether they should be retained. If a milliblock satisfies the trigger, the responsible buffer node stores it permanently.

2.3.3 Triggering

The FD is located on the Earth surface with little overburden and records data continuously; as a result, long-term storage of the resulting large data volume is expensive. To guaranty that only interesting physics events are permanently saved, NOvA uses a series of triggers that decide which segments of the detector readout to be retained. In NOvA, triggering is designed as an integral part of the DAQ system. Two main categories of triggers are used [76, 77]:

- Global triggers represent a set of trigger configurations that use timing conditions as their primary selection criterion. The main trigger in this category is the NuMI trigger, which records 550 μs of data generated from the neutrino beam. Similarly, a cosmic pulse trigger is set up to acquire 550 μs of data at a frequency of 10 Hz. The resulting cosmic-ray-induced data are then used for detector calibration and to estimate background in specific physics analyses.

- Data-driven triggers (DDTs) are sets of software-based trigger algorithms that continuously analyze the data and, once certain predefined criteria are met, decide whether the associated events should be stored permanently. Within the FD, a wide variety of DDTs is used, for instance, for magnetic monopoles, supernovae, and several other dedicated triggers. The monopole triggers, which search for signatures of highly ionizing particles in the cosmic flux, are discussed in more detail in Chapter 4.

2.4 Detector Calibration

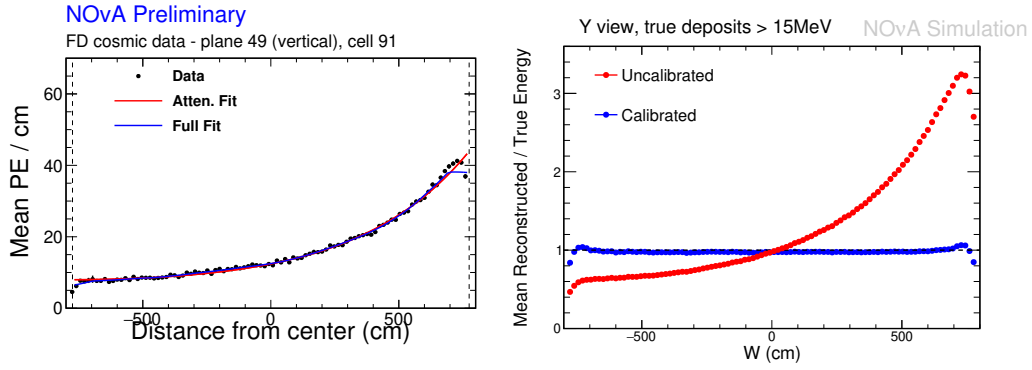
The purpose of detector calibration is to convert the measured electronic signals into physically meaningful energy units. The overall calibration procedure consists of two main steps: attenuation calibration and absolute calibration.

The attenuation calibration corrects for position dependent variations in the detector response, ensuring that the same amount of deposited energy produces a uniform signal regardless of where it occurs within the detector. After this step, the detector response is expressed in terms of corrected photoelectrons (PECorr). The absolute calibration then determines a global conversion factor that translates this position corrected response into an energy scale in units of GeV.

Cosmic ray muons are used as a natural and abundant calibration source. Their energy loss in matter is well understood and provides a reliable reference for calibrating the detector response.

2.4.1 Attenuation Calibration

As light travels along the WLS fibers toward the APD, part of it is gradually lost. As a result, signals originating farther from the readout end appear weaker than those produced nearby. The attenuation calibration corrects for this effect so that the detector response becomes independent of position.



(a) (b)

Figure 2.10: (a) Example attenuation fit for a detector cell using cosmic-ray data. (b) Detector response as a function of distance before and after calibration, demonstrating the removal of position dependence.

This calibration is performed using through-going cosmic ray muons, which deposit nearly uniform energy as they traverse the detector. First, well reconstructed muon tracks are selected, and the associated hits are identified. For each hit, the signal is expressed as the number of photoelectrons per unit path length (PE/cm), and studied as a function of the distance from the readout end of the fiber, denoted by W. This procedure is carried out on a channel-by-channel basis to accurately characterize the light attenuation in each detector cell.

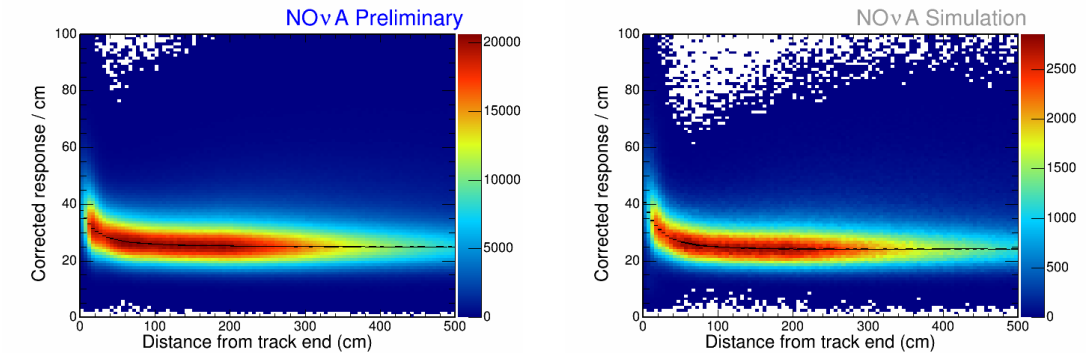
To ensure consistency, the measured signal is normalized by the path length of the track within each cell. This accounts for variations arising from different track angles, reconstruction effects, or inactive channels, and improves the stability and sharpness of the signal distribution used for calibration.

The attenuation behavior is modeled using an empirical function that accounts for light traveling along both directions of the fiber:

$$y = C + A\left(\exp\left(\frac{W}{X}\right) + \exp\left(-\frac{L+W}{X}\right)\right), \tag{2.3}$$

where, y denotes the measured signal (PE/cm), W is the distance from the readout end and L is the total length of the cell. The parameters C, A, and X are obtained from the fit, with X representing the effective attenuation length of the fiber. Figure 2.10a presents the fit to cosmic-ray data for cell 91 in plane 49. Once these corrections are applied, the detector response is uniform over the entire cell length, as shown in Figure 2.10b.

2.4.2 Absolute Calibration



(a) (b)

Figure 2.11: Corrected detector response per unit path length as a function of distance from the stopping point for (a) data and (b) simulation.

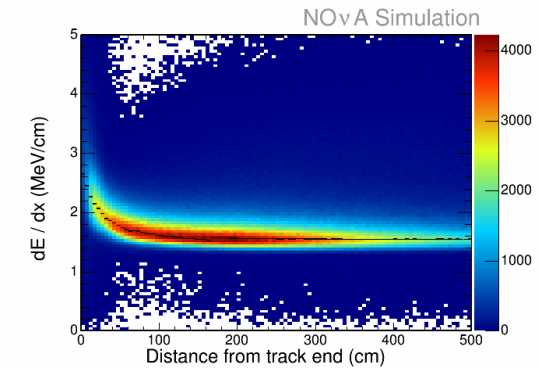


Figure 2.12: Simulated energy loss per unit length (dE/dx) as a function of distance from the stopping point.

Once the attenuation correction is applied, the detector response is uniform across all

positions. The goal of absolute calibration is to convert this corrected response (PECorr) into an energy scale expressed in GeV.

For this purpose, stopping cosmic muons are used, as they deposit a well understood amount of energy before coming to rest. Their energy loss follows the Bethe–Bloch description, making them a reliable standard for calibration. Stopping muons are identified by the presence of a decay electron at the end of their track, arising from the decay

$$\mu^- \rightarrow e^- + \bar{\nu}_e + \nu_\mu. \tag{2.4}$$

To minimize variations in energy loss, only hits within a defined segment of the track are considered. Figure 2.11 shows PECorr/cm as a function of the distance from the end of the track for both the data and the simulation. Similarly, Figure 2.12 displays the simulated energy loss per unit length, dE/dx in GeV/cm, as a function of the distance from the end of the track. From these plots, it is evident that for cosmic muons with typical energies, the energy loss remains approximately constant in the region 100–200 cm from the track end. This region is therefore chosen as the optimal interval for studying energy deposition, providing a reliable reference for calibration. Additional selection criteria are applied to ensure accurate reconstruction of the track and its geometry.

The calorimetric energy scale is then obtained from the ratio of dE/dx to PECorr/cm as follows:

$$\text{Calorimetric energy scale} = \frac{\left(\frac{dE}{dx}\right)_{\text{truth}}}{\left(\frac{\text{PECorr}}{\text{cm}}\right)_{\text{reco}}} = \text{GeV/PECorr}. \tag{2.5}$$

This factor provides the final conversion between the detector response and the physical energy scale in GeV. Once applied, it allows all recorded signals in the detector to be directly interpreted in terms of deposited energy, completing the calibration procedure.

Chapter 3

Simulation of Magnetic Monopoles

To evaluate the sensitivity of this search, it is essential to understand, through detailed simulation, how effectively the FD can detect magnetic monopole signatures. The Monte Carlo (MC) simulation within the FD is implemented in several stages that replicate the full chain from event generation to detector readout. This chapter outlines the entire simulation pipeline and is organized as follows. The analysis begins by generating monopole events with specified kinematic properties, as described in Section 3.1. These monopoles are then propagated through the detector geometry using Geant4, which simulates their interactions with detector materials and the resulting energy deposition, as detailed in Section 3.2. This is followed by a discussion of how light production is modeled in a liquid scintillator. The light yield and the custom electronics simulation used to model photon transport and the performance of front-end readout are discussed in Sections 3.3, 3.4, and 3.5.

Because the FD is located on the Earth's surface, the simulation also incorporates realistic detector conditions by overlaying unbiased cosmic-ray data with the simulated monopole events. The event visualization tools are then used to highlight the distinctive features of these overlaid monopole events, as presented in Section 3.6. The simulation of additional effects that have the tendency to affect the monopole selection efficiency, such as delta-ray production and crosstalk induced by fast monopoles, are discussed in Section 3.7. Finally, the simulation of potential background processes is described in Section 3.8.

β Values			
1.00000000e-04	1.00000000e-03	1.00000000e-02	1.00000000e-01
1.25892541e-04	1.25892541e-03	1.25892541e-02	1.25892541e-01
1.58489319e-04	1.58489319e-03	1.58489319e-02	1.58489319e-01
1.99526231e-04	1.99526231e-03	1.99526231e-02	1.99526231e-01
2.51188643e-04	2.51188643e-03	2.51188643e-02	2.51188643e-01
3.16227766e-04	3.16227766e-03	3.16227766e-02	3.16227766e-01
3.98107171e-04	3.98107171e-03	3.98107171e-02	3.98107171e-01
5.01187234e-04	5.01187234e-03	5.01187234e-02	5.01187234e-01
6.30957344e-04	6.30957344e-03	6.30957344e-02	6.30957344e-01
7.94328235e-04	7.94328235e-03	7.94328235e-02	7.94328235e-01

Table 3.1: The β values of simulated monopoles.

3.1 Isotropic Monopoles Generator

In the NOvA simulation framework, magnetic monopoles are generated under the assumption of an isotropic angular distribution, consistent with the lack of prior information on any preferred incoming direction. For each simulated monopole, an entry point is assigned by choosing a random location on a randomly selected surface of the FD. This procedure ensures that the simulated events are uniformly distributed on all detector surfaces. Monopoles are generated at 40 logarithmically spaced values of β between 10^{-4} and 0.8, with ten points per decade (see Table 3.1), and 10^5 monopoles simulated in each β. The simulated monopoles carry a single Dirac magnetic charge, g_D and no electric charge. Their mass is fixed at 10^{16} GeV, sufficiently large that they can be treated arbitrarily heavy, so that energy losses in the detector medium do not induce any appreciable change in their velocity. Figure 3.1 presents the distribution of the simulated monopole events on each surface of the detector. Due to their smaller geometric dimensions relative to the other four faces, the front and end surfaces of the detector register a reduced number of events. In addition, because monopoles do not stop inside the detector, their entry and exit points are distributed in a similar way over the entire surfaces.

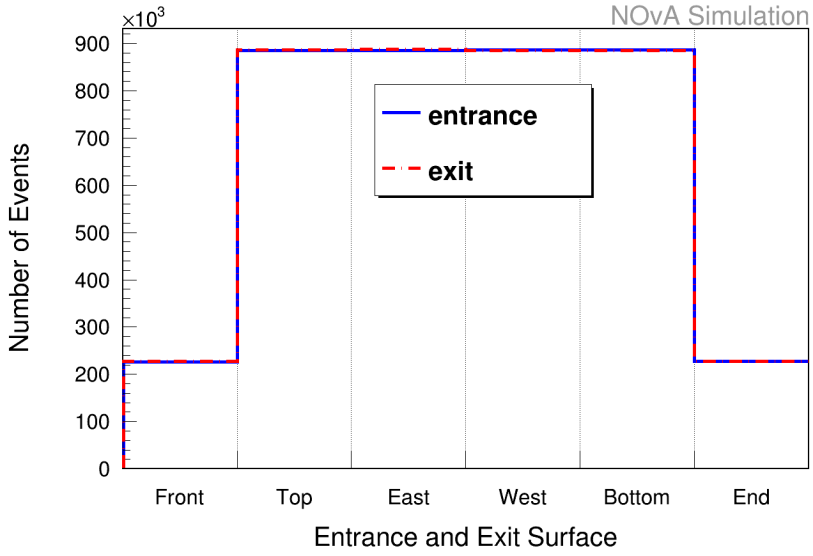


Figure 3.1: Simulated monopole distribution at each surface. The blue solid line represents the distribution of entry points of events on all the surfaces, and the red dashed line represents the exit points.

The monopole flux intensity is defined as

$$I(x, y, \theta, \phi) = \frac{dR}{dA_p \, d\Omega}, \tag{3.1}$$

where dA_p denotes an infinitesimal area element whose normal vector is aligned with the monopole propagation direction, and $d\Omega = \frac{dA_p}{r^2} = \sin\theta \, d\theta \, d\phi$ represents the differential solid angle on a sphere of radius r centered at the interaction point. Here, I is the intensity and dR is the differential rate at which the monopoles cross dA_p. Now consider a detector surface element dA with a normal vector $\vec{n}$, while the incoming monopoles move along a direction characterized by the normal vector $\vec{n_p}$ (the normal of dA_p). By projecting dA onto dA_p, one obtains the relation $dA_p = dA \, \vec{n} \cdot \vec{n_p}$, as illustrated in Figure 3.2. The associated rate can then be expressed as

$$dR = I(x, y, \theta, \phi) \, dA \, (\vec{n} \cdot \vec{n_p}) \, \sin\theta \, d\theta \, d\phi. \tag{3.2}$$

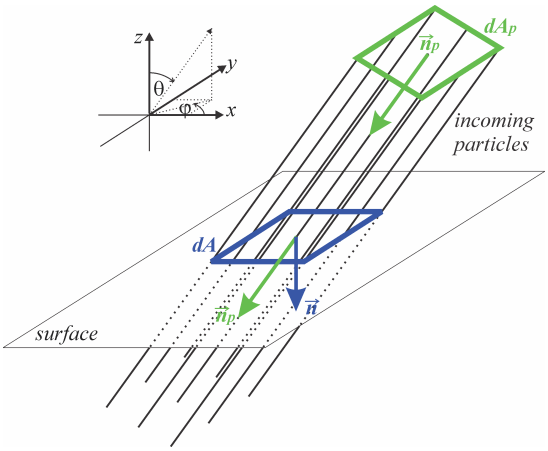


Figure 3.2: The coordinates used for isotropic generation of monopoles.

For an isotropic monopole flux, each direction (or, equivalently, each infinitesimal element of the solid angle) has the same intensity. Thus, we can substitute $I(x, y, \theta, \phi)$ with a constant intensity I_0 that is independent of (x, y, θ, ϕ). Using the coordinate system shown in Figure 3.2 and focusing on the top face of the FD, the normal outward surface is $\vec{n} = (0, 0, -1)$, while the direction of propagation of the monopole can be written as $\vec{n_p} = (\sin\theta\cos\phi,\ \sin\theta\sin\phi,\ \cos\theta)$. Their scalar product is therefore $\vec{n} \cdot \vec{n_p} = -\cos\theta$, and the corresponding particle rate, integrated over $\pi/2 \leq \theta' \leq \theta$ and $0 \leq \phi' \leq \phi$, is

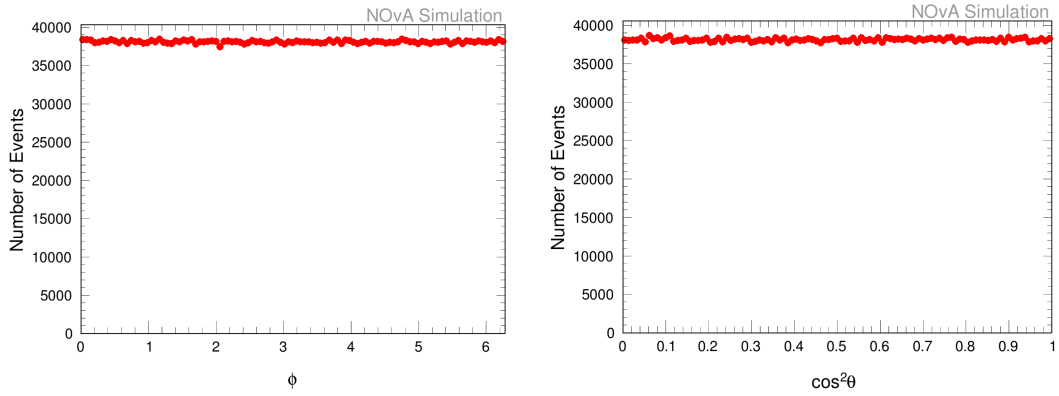
$$R(\theta, \phi) = -AI_0 \int_{\pi/2}^{\theta} \int_{0}^{\phi} \cos\theta' \ \sin\theta' \, d\theta' \, d\phi', \tag{3.3}$$

with $\pi/2 \leq \theta \leq \pi$ and $0 \leq \phi \leq 2\pi$, ensuring that only monopoles traveling downward are taken into account. As a result, the cumulative distribution as a function of zenith angle is

$$P(\theta) = \frac{R(\pi/2 \leq \theta' \leq \theta)}{R_{\text{total}}} = \cos^2\theta, \tag{3.4}$$

and similarly for the azimuthal angle

$$P(\phi) = \frac{\phi}{2\pi}\,. \tag{3.5}$$



(a) (b)

Figure 3.3: Simulated event distributions as functions of (a) ϕ and (b) $\cos^2\theta$. The figures indicate that the simulated events are uniformly distributed in ϕ over the interval 0 to 2π, and uniformly distributed in $\cos^2\theta$ over the interval 0 to 1.

To generate random angles according to these distributions, we start from random numbers that are uniformly distributed between 0 and 1. By equating the cumulative probabilities to these uniform variables, we define $P(\theta) = \cos^2\theta = u_1 \in (0,1)$ and $P(\phi) = \phi/(2\pi) = u_2 \in (0,1)$, where u_1 and u_2 are independent uniform random variables. This uniquely specifies the zenith angle and the azimuthal angle.

$$\theta = \arccos(-\sqrt{u}), \tag{3.6}$$

$$\phi = 2\pi u, \tag{3.7}$$

and the corresponding distributions of θ and ϕ are presented in Figure 3.3.

3.2 Energy Loss Model

The energy loss model for magnetic monopoles used in this analysis follows the framework established by Ahlen and Kinoshita [79, 80] for both high- and low-β monopoles. Because of their large effective magnetic charge, magnetic monopoles are expected to deposit extremely large amounts of energy as they traverse matter. Figure 3.4 (adapted from

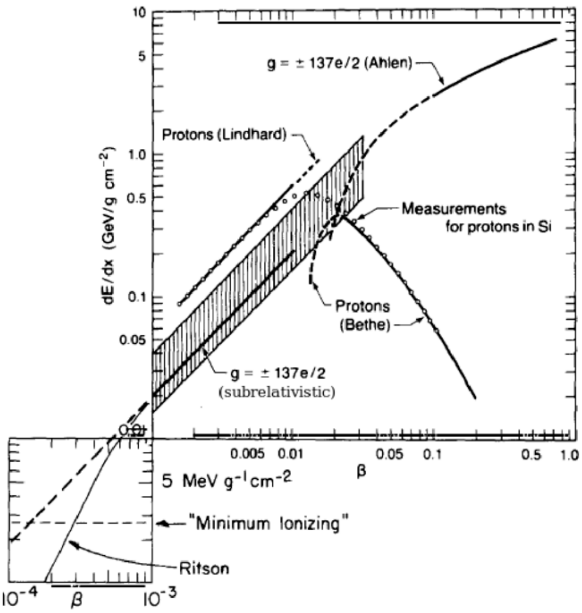


Figure 3.4: Energy loss in silicon for monopoles with $g = \pm 137e/2$ as a function of the monopole's velocity, adapted from Groom's review [78]. The shaded band surrounding the solid curve at low velocities indicates the theoretical uncertainty in the predicted energy deposition.

Groom's review [78]) illustrates how the energy loss of a monopole depends on its velocity. As it moves through a medium, a monopole predominantly loses energy by ionizing and exciting the atoms and molecules along its trajectory. This energy loss mechanism arises from the interaction between the electric field induced by the moving magnetic charge and the electrons in the material. For velocities $\beta \geq 0.1$, the stopping power is described by a Bethe-Bloch expression, modified by Ahlen for a monopole carrying magnetic charge $g = 137e/2$ [79]. In the low-velocity region, $\beta \leq 0.01$, the stopping power is calculated using the Ahlen-Kinoshita formalism [80].

In these two limiting regimes, the primary contribution to energy loss is well understood: ionization processes dominate for $\beta \gtrsim 0.1$, while atomic excitation processes are most important for $\beta \lesssim 0.01$. In the intermediate velocity interval, both processes play significant

roles, and neither can be ignored; thus, an interpolation between the two regimes is carried out to obtain a continuous and physically reliable representation of the stopping power.

The following sections present these theoretical energy loss models in detail, explain how they are implemented in the NOvA simulation framework, and outline the correction procedures taken into account to accurately reproduce the detector's response to a slowly moving particle.

3.2.1 Monopoles with $\beta \geq 0.1$

For magnetic monopoles with velocities $\beta > 0.1$, the energy loss in the NOvA scintillator is more accurately modeled by the Ahlen expression [79]:

$$\left(\frac{dE}{dx}\right)_1 = \frac{4\pi N_e g^2 e^2}{m_e c^2}\left[\ln\frac{2m_e c^2\beta^2\gamma^2}{I} + \frac{K(|g|)}{2} - \frac{1}{2} - \frac{\delta}{2} - B(|g|)\right]. \tag{3.8}$$

In this formula, N_e is the electron density, δ is the density-effect correction, $B(|g|) = 0.248$ is the Bloch correction, and $|g| = 137e/2$ is the magnitude of the monopole's magnetic charge. The term $K(|g|) = 0.406$ corresponds to the QED correction for $|g| = 137e/2$ [79]. The density-effect correction δ is computed using Sternheimer's approach and is written as

$$\delta = \begin{cases} \ln(\beta^2\gamma^2) - 2\ln\left(\frac{I}{\hbar\omega_p}\right) + a(X_1 - X)^m - 1, & X_0 < X < X_1 \\ \ln(\beta^2\gamma^2) - 2\ln\left(\frac{I}{\hbar\omega_p}\right) - 1, & X > X_1 \\ 0, & X < X_0 \end{cases} \tag{3.9}$$

where $X = \log_{10}(\beta\gamma)$. The values of N_e, I, X_0, X_1, a, and m appropriate for the NOvA liquid scintillator are summarized in Table 3.2.

Density (g cm^{-3})	N_e (cm^{-3})	I (eV)	m	a	X_0	X_1
0.853	2.93×10^{23}	56.4	3	0.367	0.2	2

Table 3.2: Properties of the NOvA scintillator used in the energy loss calculation.

3.2.2 Monopoles with $\beta \leq 0.01$

For slowly moving magnetic monopoles with velocities $\beta < 0.01$, the stopping power in the NOvA scintillator is more accurately described by the Ahlen-Kinoshita formalism [80]. In this regime, the stopping power formula is given by

$$\left(\frac{dE}{dx}\right)_2 = \frac{2\pi N_e g^2 e^2 \beta}{m_e c v_F}\left[\ln\left(\frac{2m_e v_F \Lambda}{\hbar}\right) - \frac{1}{2}\right], \tag{3.10}$$

where N_e represents the electron number density in the medium, g is the monopole's magnetic charge, and e denotes the elementary electric charge. The quantity $\Lambda = 5.3 \times 10^{-9}$ cm is identified with the Bohr radius. The Fermi velocity v_F of the electrons is then defined as

$$v_F = \frac{\hbar}{m_e}(3\pi^2 N_e)^{1/3}, \tag{3.11}$$

3.2.3 Detector Response to Slow Signals

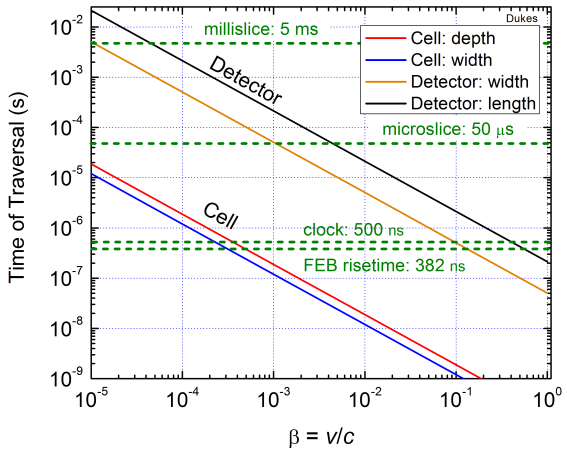


Figure 3.5: The time of traversal for monopoles to cross the FD as a function of their velocity and path length.

NOvA detectors are designed primarily to measure the energy deposited by relativistic particles. However, magnetic monopoles are expected to pass through the FD with velocities that can be substantially lower than the speed of light. Figure 3.5 shows the time a monopole needs to traverse the FD as a function of its velocity; for a monopole with $\beta < 0.01$, it takes more than 20 μs to cross the entire detector length, which is much slower than the speed of light particles. To study how the detector responds to these slow, highly ionizing particles, a dedicated test-stand was carried out. In this configuration, APDs using the standard NOvA readout electronics were subjected to LED light pulses that were carefully adjusted to replicate the anticipated signatures of magnetic monopole–induced signals. The time structure of the pulses was selected to match the time it would take a monopole to cross a single cell, and the pulse intensities were set to reproduce the predicted energy loss of monopoles over a range of possible velocities.

The measured detector response was observed to agree well with simulations of the readout electronics, consistent with a 10% systematic uncertainty assigned to the test-stand measurement. To conservatively allow for the possibility that the detector response to slow signals has been overestimated, the expected signal is decreased by 10% for monopoles with velocities $\beta \leq 0.01$. For monopoles with $\beta \geq 0.1$, a smaller correction of 3% is applied to account for theoretical uncertainties in the energy loss modeling [79]. In the intermediate region $0.01 < \beta < 0.1$, a smooth linear interpolation is performed to connect these two regimes.

To characterize this decrease in energy loss, we start from the nominal stopping power $\left(\frac{dE}{dx}\right)_1$ and $\left(\frac{dE}{dx}\right)_2$, defined in Equations 3.8 and 3.10, respectively. Imposing a 3% reduction in Equation 3.8 yields the corresponding effective energy loss.

$$\left(\frac{dE}{dx}\right)_{\text{fast}} = 0.97 \left(\frac{dE}{dx}\right)_1 . \tag{3.12}$$

Similarly, implementing a 10% reduction in Equation 3.10 gives the effective energy loss

in the slow regime,

$$\left(\frac{dE}{dx}\right)_{\text{slow}} = 0.90 \left(\frac{dE}{dx}\right)_{2}. \tag{3.13}$$

The reduced stopping power expressions given in Equations 3.12 and 3.13 are incorporated into Geant4 [81] within the NOvA simulation framework to describe the energy loss of magnetic monopoles for velocity regimes $\beta > 0.1$ and $\beta < 0.01$, respectively.

3.2.4 Intermediate Velocity Region $(0.01 < \beta < 0.1)$

For monopoles in the range $0.01 < \beta < 0.1$, a consistent expression of energy loss can be obtained by interpolating between the two regimes $\beta > 0.1$ and $\beta < 0.01$. This procedure yields a continuous and consistent formula for the monopole energy loss rate across the transition from relativistic to non-relativistic regimes, thereby removing any unphysical discontinuities in the predicted signal. The interpolation is given by

$$\left(\frac{dE}{dx}\right)_{\text{int}} = \frac{(\beta - 0.01)\,(dE/dx)_{fast} + (0.1 - \beta)\,(dE/dx)_{slow}}{(\beta - 0.01) + (0.1 - \beta)} \tag{3.14}$$

where $(dE/dx)_{fast}$ denotes the reduced energy loss for monopoles with $\beta \geq 0.1$, as defined in Equation 3.12, and $(dE/dx)_{slow}$ denotes the reduced energy loss for monopoles with $\beta \leq 0.01$, as defined in Equation 3.13.

3.3 Light Yield by Magnetic Monopoles

Magnetic monopoles passing through the liquid scintillator produce light primarily through scintillation, triggered by ionization, and through Cherenkov radiation. Once the energy deposition within the PVC cells has been simulated using Geant4, the resulting deposited energy must be converted into the corresponding scintillation light yield.

For an ideal scintillator with a linear response, the light yield along the particle track would be directly proportional to the local energy loss per unit length. However, for sufficiently large stopping powers (high dE/dx), organic scintillators exhibit substantial recom-

bination and quenching effects that reduce the effective light yield. The following sections present a detailed description of this quenching mechanism for the monopole signal in the FD.

3.3.1 Ionization and Birks' Quenching Effect

Due to their large magnetic charge, monopoles deposit substantially more energy in the detector medium than conventional electrically charged particles, as expressed in Equations 3.8 and 3.10. For such strongly ionizing particles, the scintillation light is suppressed as a consequence of quenching phenomena occurring within the scintillator material. This behavior is described by the empirical relation known as Birks' law [82], given by

$$\frac{dL}{dx} = L_0 \frac{\frac{dE}{dx}}{1 + k_B \frac{dE}{dx}} \tag{3.15}$$

where $\mathrm{d}L/\mathrm{d}x$ represents the light yield per unit track length, $\mathrm{d}E/\mathrm{d}x$ is the specific energy loss, L_0 denotes the scintillation efficiency in the absence of quenching, and k_B is the Birks constant, which characterizes the strength of the scintillation quenching effect.

When Birks' empirical quenching description is extended to include a second order term in the stopping power, the resulting formula is known as the Birks-Chou model [83]. In differential form, it is expressed as

$$\frac{dL}{dx} = L_0 \frac{\frac{dE}{dx}}{1 + k_B \frac{dE}{dx} + k_C \left(\frac{\mathrm{d}E}{\mathrm{d}x}\right)^2} \tag{3.16}$$

where k_C denotes the second order quenching parameter, known as the Chou constant.

A dedicated test stand [84] was constructed to make precise measurements of the Birks constant and thus determine the light yield of the NOvA scintillator for strongly ionizing particles. In this setup, a neutron source generated recoil protons in a small sample of NOvA scintillator, and the resulting scintillation light was collected with photosensors. A timing system recorded the neutron time-of-flight to the scintillator, and the energies of the corre-

sponding protons were determined. The light output from these protons was then calibrated by comparison with the detector response to well characterized gamma-ray sources. By varying the Birks constant in the light response model until the predicted yield agreed with the observed signal, its value was determined to be $(1.155 \pm 0.065) \times 10^{-2}$ g cm^{-2} MeV^{-2}. Birks' law implies that the scintillation signal saturates and ceases to increase significantly beyond $\beta \approx 0.1$ even as the energy loss increases.

3.3.2 Cherenkov Radiation from Magnetic Monopoles

In addition to the scintillation photons generated through ionization processes, magnetic monopoles with sufficiently high velocities can also emit Cherenkov radiation when their velocity exceeds the Cherenkov threshold in the medium. The equivalent Frank-Tamm formulation [85] for magnetic monopoles predicts that the Cherenkov photon yield is significantly enhanced relative to that of an electrically charged particle. In particular, a monopole carrying a magnetic charge g produces $(gn/e)^2$ times more Cherenkov photons than a particle carrying an electric charge e traveling at the same speed in a medium with refractive index n [86].

The NOvA scintillator has a refractive index that depends on wavelength; at 400 nm it is 1.47, which implies a Cherenkov threshold of $\beta \approx 0.68$ for magnetic monopoles. Once above this threshold, a magnetic monopole carrying magnetic charge g_D is expected to generate $\mathcal{O}(10^4)$ times more light than a typical cosmic muon in the FD. For monopoles with $\beta > 0.68$, the overall light output receives contributions from both ionization energy loss and Cherenkov emission. A magnetic monopole traversing the FD is therefore expected to leave a very bright track with an approximately uniform light yield along its trajectory.

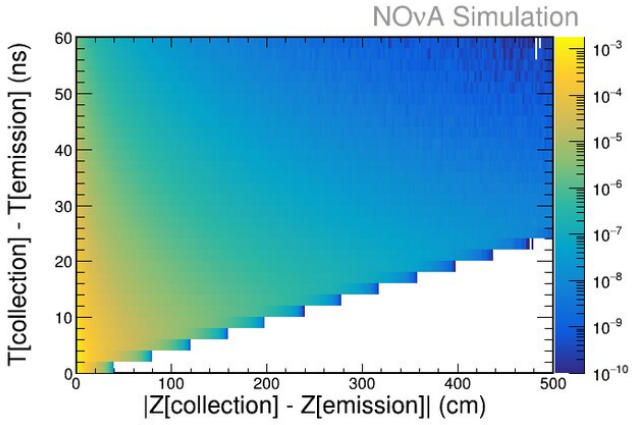


Figure 3.6: The collection rate of scintillation photons by the WLS fiber, as determined using a custom simulation [5].

3.4 Simulation of Photon Transport

A complete optical simulation of light production and transport using Geant4 through the detector cell, the WLS fiber, and their detection in the APD is computationally expensive. Therefore, the simulations of these procedures are performed with custom simulation tools developed specifically for the NOvA detectors. Since the detectors are composed of many identical readout cells, the simulation framework precomputes the photon transport a single time and stores the outcome as parameterized templates. These templates are then applied uniformly throughout the detector, greatly reducing the computational load while maintaining an accurate representation of the optical response [5]. The parameterization includes three main components: the collection of scintillation photons by the WLS fiber, the transport of light along the fiber, and the response of the APD to the incident photons.

The custom simulation models the collection of scintillation photons by the WLS fiber by taking into account the measured scintillation spectrum of the liquid scintillator, the average reflectivity of the PVC cell walls, and the absorption properties of the WLS fibers. This simulation produces a template for the photon collection rate as a function of both the

distance along the cell between the point of collection and its point of origin (ΔZ), and the difference between the time of emission and the time of collection (ΔT), as illustrated in Figure 3.6.

Once the photons are captured by the fiber, they must travel along it to reach the APD at the readout end. The simulation models this transport by accounting for photon propagation along both directions of the fiber loop. As photons travel through the fiber, some are lost as a result of attenuation, which reduces the number that reach the APD. Also, there is a variation in travel times due to different paths of the photons along the fiber. By combining these effects, the simulation determines the expected number of detected photoelectrons as a function of time for each energy deposition in the detector.

Finally, the overall light yield of the detector is determined by the conversion between visible deposited energy and the number of produced scintillation photons. To perform this calibration using the cosmic-ray muons passing through the detector, we follow the same procedure discussed in Section 2.4.

3.5 Simulation of Electronics Readout

The goal of electronics simulation is to transform the distribution of photoelectrons as a function of time obtained from the photon transport stage into digitized signals similar to that observed in the detector readout system. This process models the operation of the front-end electronics, including an ASIC responsible for pulse shaping, an ADC that digitizes the shaped analog signals, and an FPGA that performs real-time processing.

Once photoelectrons are produced at the APDs, their signals are first shaped in time to form a smooth pulse. This behavior is represented by a response function with rise time R and fall time F, defined as

$$f(t) = \frac{F}{F-R}\left(e^{-(t-t_0)/F} - e^{-(t-t_0)/R}\right), \tag{3.17}$$

where t_0 denotes the time at which the photoelectron is detected by the APD.

Following the shaping stage, the analog signal is converted into digital units (ADC counts). This conversion depends on the detector gain and the electronics response, and can be written as

$$\text{ADC} = \frac{N_{\text{pe}}\, M_{\text{APD}}\, f(t)}{M_{\text{FEB}}}, \tag{3.18}$$

where, M_{APD} is the gain of the APD, which amplifies the initial number of photoelectrons N_{pe} into a larger number of electrons. The function $f(t)$ describes the shaping function defined in Equation 3.17. Finally, M_{FEB} denotes the gain of the FEB, which converts multiplied electrons into ADC counts. For the FD, $M_{\text{FEB}} = 53$ and $M_{\text{APD}} = 150$. The ADC output reaches saturation at a maximum value of 4095. Overall, this simulation step produces a time-dependent digital signal for each energy deposition, closely matching the behavior observed in the detector. After this, a baseline and electronic noise are added to reproduce realistic detector conditions.

For charged particles moving well below the speed of light and in particular for very slow magnetic monopoles, the resulting pulse shape is strongly modified. Specifically, the rise time of the amplified pulse increases, because the monopole may require more than 382 ns to cross the detector, as illustrated in Figure 3.5. The FEB response to such a slow particle, for which the time spent inside the cell is no longer negligible, can be modeled as the superposition of the responses to many fast particles hitting the same cell over a uniform and continuous time interval assuming the particle's velocity remains constant within the cell.

To reduce the amount of data, a zero-suppression procedure is applied to retain only significant signals. This is achieved using the DCS method introduced earlier in Section 2.2.6, where signals exceeding a predefined threshold are identified as valid hits. In the detector readout, these thresholds are set on a channel-by-channel basis using periodic calibrations,

while in the simulation they are taken from recorded detector conditions. This ensures that the simulation closely matches the response of the actual DAQ system.

3.6 Overlay with Cosmics

After propagating through the full simulation chain in the NOvA simulation framework, as outlined in the previous sections, we arrive at this stage with a fully simulated event that contains a monopole. However, the effect of cosmic-ray-induced activity in the FD, arising from its surface location, has not yet been included and needs to be taken into account.

Because the FD operates at the surface and is subject to a high flux of cosmic rays (around 150 kHz), we merge each simulated monopole event with 5 ms of minimum-bias FD data (i.e., data recorded and written to permanent storage without any event selection) in order to accurately reproduce the cosmic-induced activity in the FD during a possible magnetic monopole passage. The resulting sample thus contains events in which both the simulated monopole signal and the typical detector activity are present. The cosmic events used for this overlay are taken from data collected with the Supernova Early Warning System (SNEWS) trigger. These minimum-bias data are taken to be free of monopole signals, and the simulated monopole events are overlaid on them to reproduce the expected full detector response to a monopole passage in FD. This method has two main benefits: it eliminates systematic uncertainties related to modeling cosmic and electronic noise hits, and it reduces the required computing resources. The information needed to distinguish hits originating from the simulation from those coming from the SNEWS data is retained.

3.6.1 Event Display of Simulated Monopole Event

The event display (EVD) is a visualization tool for representing detector events. The EVD displays individual events in a graphical layout designed for easy interpretation. In Figure 3.7, the display shows a 5 ms time window of cosmic-ray–induced activity overlaid

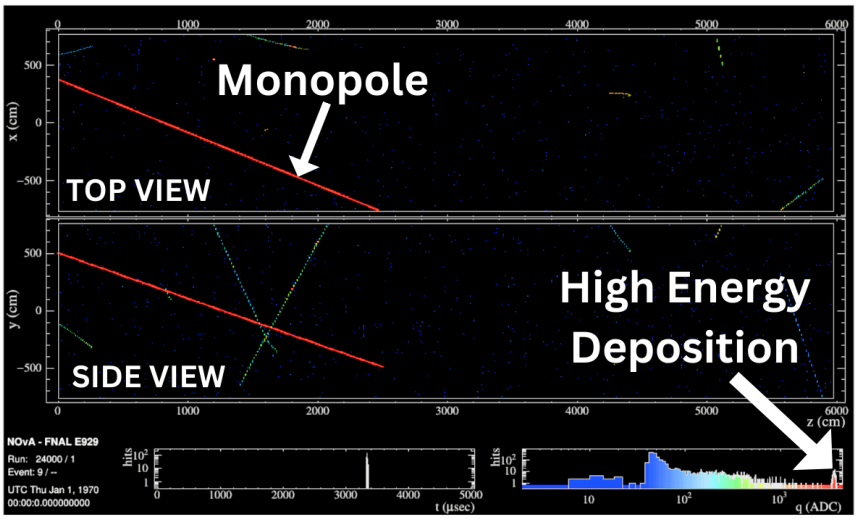


Figure 3.7: EVD of the simulated monopole with $\beta = 0.1$, overlaid with SNEWS cosmic activity. Individual hits are color-coded according to their ADC values. The monopole-induced hits appear as the two prominent red tracks in the EVD, corresponding to hits with comparatively high ADC values.

with a simulated magnetic monopole event with $\beta = 0.1$. The top panel shows the detector in the XZ plane (top view), and the bottom panel shows it in the YZ plane (side view). Two smaller panels at the bottom show the distributions of hit time and ADC counts. In this example, the hits are colored based on their ADC values such that increasing ADC values are represented by a color gradient spanning from blue to red. The long, straight track composed of red hits corresponds to the monopole candidate, which has high ADC values because it is highly ionizing.

A magnetic monopole traversing the FD is expected to produce a long, straight, bright, and uniform light output along its trajectory. This characteristic distinguishes monopoles from the dominant background of cosmic rays, which can be either minimally ionizing and relatively uniform in their energy deposition, as in the case of low-energy muons, or strongly ionizing and irregular hits, such as high-energy muons, protons, gamma rays, etc.

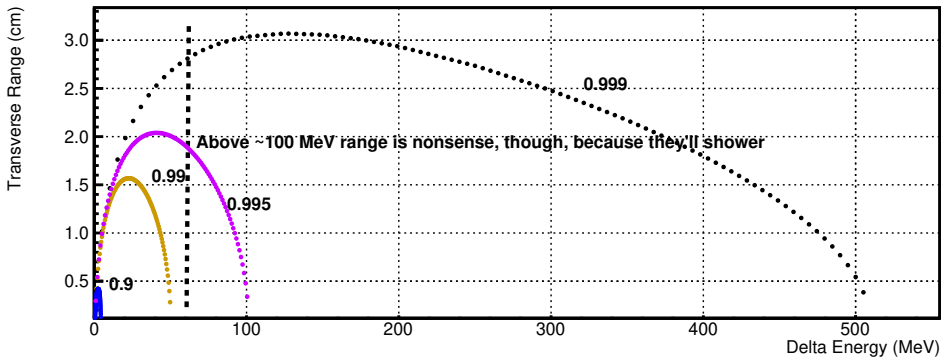


Figure 3.8: Transverse range a delta rays can travel produced from a monopole.

3.7 Delta Rays and Crosstalk by Fast Monopoles

As the monopole's speed increases, effects such as the production of intense delta rays and optical crosstalk cause the apparent monopole track to broaden, making it harder to distinguish from the irregular tracks produced by cosmic rays. These effects start to play a significant role around $\beta \approx 0.68$, making their investigation particularly relevant. At higher monopole velocities, the secondary electrons, or *delta rays*, acquire more energy and can propagate over several centimeters into adjacent detector cells. Furthermore, monopoles traveling above the Cherenkov threshold emit large amounts of light, which can induce optical crosstalk, where light originating in one cell is erroneously recorded by a different APD pixel. Therefore, both mechanisms contribute to a broadening of the reconstructed track. We simulated these processes to quantify their influence on the detection efficiency of our analysis, which is described in more detail in Chapter 5.

3.7.1 Production of Delta Rays

To estimate how far delta rays propagate transversely, we used the NIST ESTAR tables [87] for paraffin wax, which is a good approximation for the NOvA liquid scintillator because of its similar composition. These tables provide a relationship between the kinetic energy

of the electrons and their range in the medium. For a fixed monopole energy, delta rays are produced with a spectrum of energies and emission angles. For each pair of monopole energy and delta ray energy, we calculate the emission angle of the delta ray and obtain its corresponding range from the ESTAR tables. The transverse range is then obtained by projecting this range perpendicular to the monopole trajectory. By scanning the delta ray energies for each monopole energy, we obtain the corresponding angles and ranges, and hence determine the maximum transverse distance reached by the delta rays, as shown in Figure 3.8.

Monopoles with $\beta \gtrsim 0.68$ generate a large number of delta rays, and explicitly simulating all of these secondary electrons for such fast monopoles is computationally expensive. To handle this more efficiently, we adopt a simplified approach in which the intense ionization is modeled within a cylindrical region around the monopole track. The radius of this cylinder is taken to be the maximum transverse range of delta rays expected for a given monopole velocity. The approximation is well motivated, as within this volume the combined contribution from the monopole together with the high density of delta rays will completely saturate any detector channel.

Instead of explicitly tracking each delta ray, we approximate this effect using a "monopole bundle" where multiple monopoles are distributed in a circular pattern around a central trajectory and propagated in parallel through the FD. Each monopole in the bundle is assigned $\beta = 0.8$, which is above the Cherenkov threshold and sufficient to produce a saturated detector response. In this way, the bundle effectively reproduces the combined effect of the monopole and its associated delta ray cloud within the cylindrical region. This approach allows us to capture the essential physics while avoiding the need to simulate every individual delta ray.

For example, Figure 3.8 shows that delta rays produced by a monopole with $\beta = 0.995$ can reach a transverse distance of approximately 2 cm. Therefore, we model this scenario

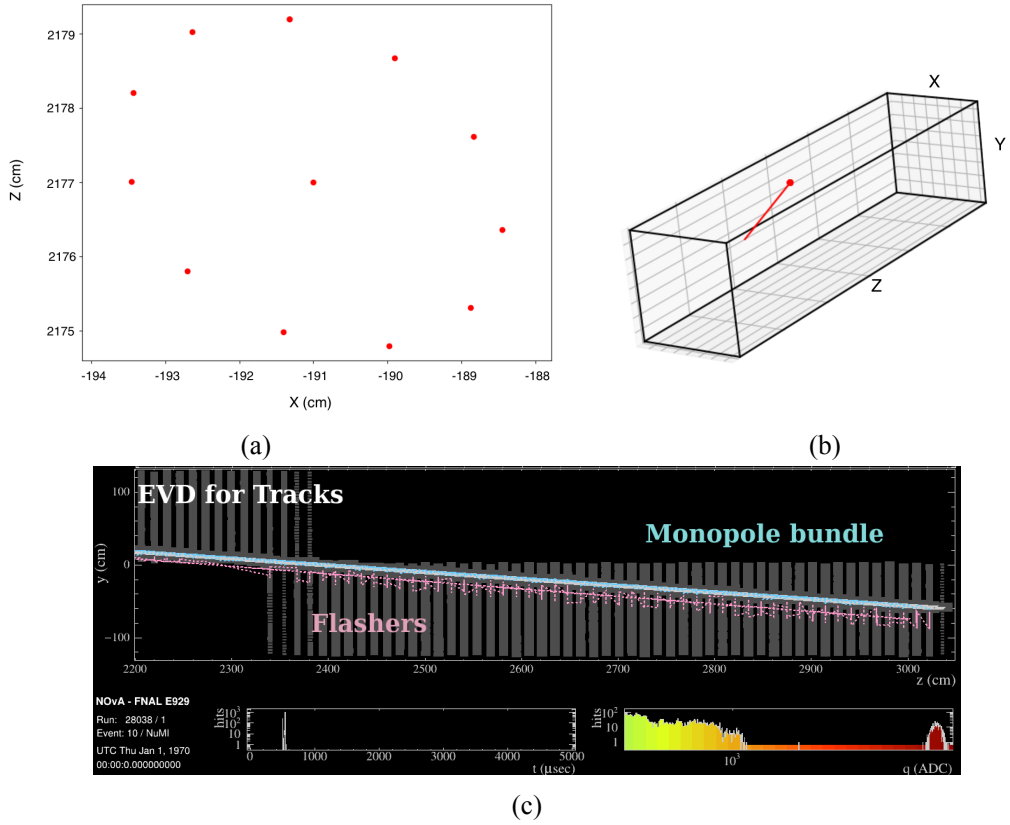


Figure 3.9: Simulation of monopole bundle of radius 2 cm (a) The entry points of the bundle on the surface of the detector, (b) The trajectory of the bundle in the FD, (c) Event display for monopole bundle of radius 2 cm.

using a monopole bundle with a radius of about 2 cm around the central monopole trajectory. A cross-sectional view of this configuration at the detector surface is shown in Figure 3.9a, with the corresponding EVD provided in Figure 3.9c. If such a configuration satisfies all analysis selection criteria (outlined in Chapter 5), it implies that a real monopole with $\beta = 0.995$, along with its associated delta rays, would also be efficiently selected. A similar procedure is followed for lower velocities. For example, a monopole with $\beta = 0.99$ produces delta rays with a maximum transverse range of about 1.5 cm, which is modeled using a bundle of corresponding radius to evaluate the selection efficiency. The reconstruc-

tion of these delta rays and their influence on the overall detection efficiency are examined in more detail in Chapter 5.

3.7.2 Crosstalk by Fast Monopoles

Monopoles traveling above the Cherenkov threshold produce intense light. In most regions of the detector this does not lead to any issues. However, near the detector boundaries where light is guided to the APDs, the WLS fibers from each cell of the 32-cell intrusion module pass through a common optical volume, called the manifold (see Section 2.2.5). This region is enclosed in black plastic, which reflects very little scintillation light and is meant to suppress the collection of light originating there. However, the Cherenkov light emitted by monopoles is so intense that it can significantly illuminate some or all of the fibers in this region, creating spurious hits at the ends of tracks. On the side surface of the detector, where the cells are oriented horizontally and the manifold is completely filled with scintillator, we anticipate that the monopole will light up all 32 cells in the module. On the top surface of the detector, the cells are vertically oriented and the manifold may or may not be filled with scintillator. If a cell is overfilled, we may see an effect similar to that observed for horizontal cells. Similarly, on the end opposite the APDs, there are end plates, a narrow channel that connects neighboring detector cells, which was required during construction to fill the detector with the scintillator. Under normal conditions, any light leak through this channel is negligible, but Cherenkov light can reflect through these channels strongly enough to generate hits in cells adjacent to the trajectory of the monopole. We collectively label these phenomena as optical crosstalk. The crosstalk becomes significant around $\beta \approx 0.68$, and it can cause the reconstructed monopole track to look wider than expected in the first and last planes. To assess how this apparent track widening influences detection efficiency, we modeled it in our simulations.

Crosstalk is expected to matter only within the first and last few centimeters of the

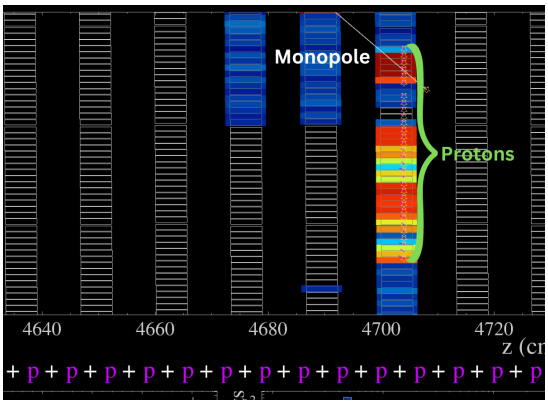


Figure 3.10: The EVD for a event with crosstalk from monopoles above the Cherenkov threshold that is generated by injecting protons together with the monopoles. In this event, the monopoles and the protons enter through the side face and induce crosstalk in the module composed of scintillator filled horizontal cells. This method provides a rough approximation of the actual crosstalk effects produced by monopoles in the scintillator filled fiber manifold.

track. Although accurately simulating crosstalk would require complex modifications to the low-level simulation, an approximate study can be performed by injecting additional particles, such as protons, into cells where crosstalk is anticipated. Our aim with this "worst-case" style of simulation is to show that crosstalk does not substantially degrade selection efficiency, indicating that a more detailed simulation is not necessary. Figure 3.10 presents an event display from this approximate simulation, in which several protons are simulated together with a monopole above the Cherenkov threshold. A more detailed discussion of the reconstruction and of how the crosstalk affects the selection efficiency in this analysis is provided in Chapter 5.

3.8 Simulation of Background

A potential source of background for highly ionizing monopole candidates originates from cosmogenic muon bundles that traverse the FD in a nearly simultaneous and parallel configuration. Such closely spaced tracks can overlap both in space and time, making them

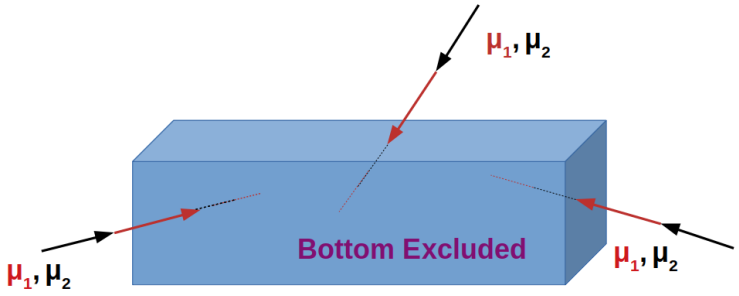


Figure 3.11: A potential background source consists of a pair of muons propagating along an identical trajectory but separated by a temporal offset.

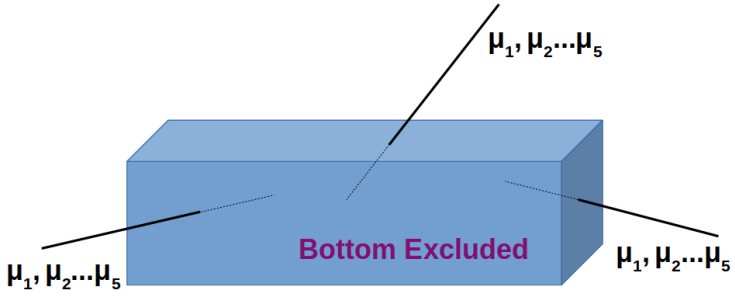


Figure 3.12: A possible background: A 5-muon bundle traveling simultaneously almost along the same trajectory.

appear as one single, strongly ionizing event. To evaluate such a potential background contribution to our data set, we performed simulations of muon pairs and muon bundles with closely matched energies traversing the detector simultaneously, as illustrated schematically in Figures 3.11 and 3.12, respectively. In these simulations, the bottom surface of the detector's generation volume is excluded, reflecting the cosmogenic origin of these events.

For each bundle configuration, muons are generated to enter the detector with the same initial position and nearly identical energies. In most cases, muons are produced simultaneously and follow the same trajectory in FD. In addition, a dedicated sample of two-muon events is generated with a finite time separation between their arrivals at the detector. The different configurations of muon bundle studies are summarized below.

1. **Two Muons with Time Offset:** A sample of 100,000 events is generated in which two muons, each with momentum of 100 ± 5 GeV, are generated at the same entry point, but reach the detector at slightly different times.

2. **Two Muons without Time Offset:** A sample of 100,000 events is generated in which two muons are generated simultaneously, each with momentum of 100 ± 5 GeV, and propagate along the same trajectory.

3. **Muon Bundles:** Samples of 100,000 events are generated each for bundles of 3, 4, and 5 muons. In each case, the muons have momentum of 100 ± 5 GeV, are produced at the same time, and follow the same trajectory.

These configurations are reconstructed and analyzed in more detail for the purpose of estimating the background contribution in the signal region relevant to this analysis, as discussed more extensively in Chapter 5.

Chapter 4

The Ionization-Based Monopole Trigger

Due to its location on the Earth's surface, the FD is continuously exposed to a high flux of cosmic-ray muons, with typical rates of the order of 150 kHz. In this chapter, we describe how the FD avoids recording the full unfiltered data stream, which would quickly exceed the available bandwidth and storage capacity of the DAQ system. Instead, it uses a software-based DDT to efficiently select monopole-like patterns while rejecting the dominant cosmic-ray background. In Section 4.1, we describe the ionization-based monopole trigger in detail. This trigger is designed to identify candidate monopole events based on the through-going and highly ionizing signatures expected from magnetic monopoles, while rejecting the majority of the cosmic-ray background and thus reducing the data rate to a manageable level. Section 4.2 discusses the trigger efficiency, and Section 4.3 summarizes the data set used in this analysis and the total live time during which the monopole trigger was active.

4.1 Ionization-Based Trigger

As previously outlined in the discussion of the NOvA triggering mechanism in Section 2.3, the signals from the detector cells are collected and organized into short time segments of the data. These segments are then transferred to buffer nodes, where they are temporarily stored. Each buffer node holds a complete snapshot of the detector activity over a short time interval, allowing the trigger system to analyze the full detector response in that window. Multiple trigger algorithms run in parallel on the buffered data, each designed to recognize a specific type of physical signature. Since the processing time available is limited, these

algorithms are optimized to be fast and efficient instead of fully reconstructing every event. When a trigger condition is satisfied, a specific time window containing the candidate event is selected and sent for permanent storage. Different trigger algorithms may identify different time regions within the same data segment, and these are recorded separately.

The NOvA FD uses several software-based DDTs [76, 77], including two that are specifically developed for magnetic monopole searches: one based on high-ionization signatures and another based on transit time information [88]. The ionization-based trigger looks for patterns distinguished by large energy deposition, while the time-based trigger selects and records events with velocities significantly below the speed of light. These two trigger categories are defined primarily for organizational convenience within the trigger system, and their selected events partially overlap. In this thesis, we restrict our attention to the ionization-based trigger.

The ionization-based trigger runs continuously, looking for long, through-going tracks with high ionization and roughly uniform energy loss, on top of a background of ordinary cosmic-ray muons. Before a trigger decision can be made, it is necessary to group data that belong to the same event, so that the trigger is evaluated using only a subset of hits within a specific and limited time window within the full 5 ms milliblock (see Section 2.3) of data. This grouping procedure is known as slicing and is described in the following.

4.1.1 Slicing

In the detector, hits produced close to each other in both space and time are grouped into units called *slices*. These slices represent clusters of activity that are likely to originate from the same physical event.

Before complete slices are formed, the hits in an event undergo a series of basic processing steps, as illustrated in Figure 4.1. First, the hits are ordered in time, then those with sufficiently large ADC values (above a threshold of 500 ADC) are retained, followed by

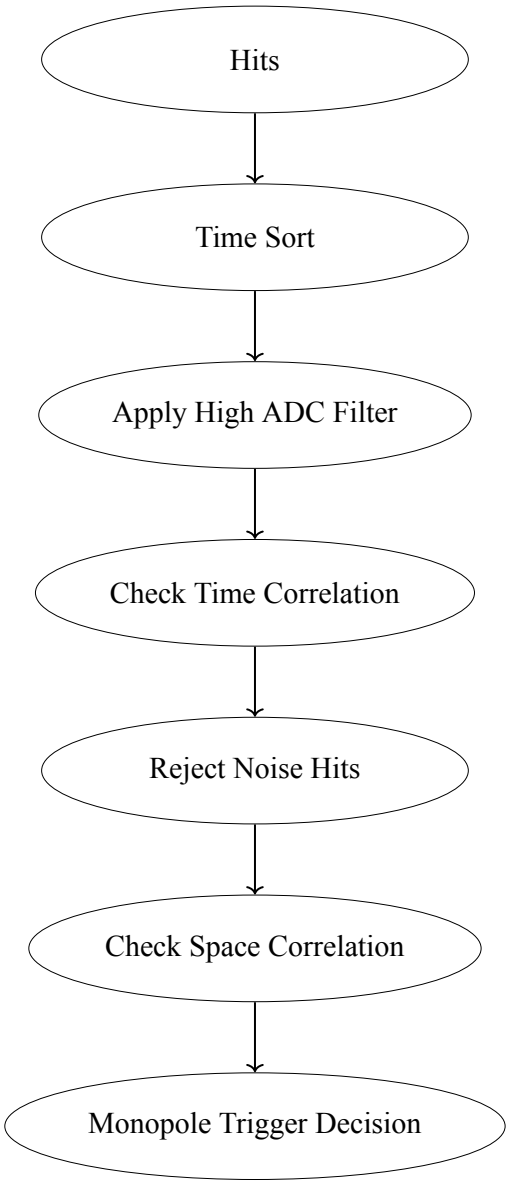


Figure 4.1: Schematic flow of data processing before trigger decision.

clustering hits that are time-correlated, suppressing noise, and finally grouping hits according to their spatial correlation. The requirement of a high-ADC threshold is motivated by the expectation that magnetic monopoles are far more highly ionizing than typical cosmic-ray particles and therefore are predicted to produce correspondingly larger ADC values; accordingly, hits with ADC values below 500 are discarded. In addition, within any short time interval within the slice, there must be a sufficient number of hits, and the activity should be continuous across detector planes without large gaps.

4.1.2 Trigger Selection

Once the slices are defined, a series of variables is computed with the associated hits information to describe their overall properties. These variables are useful in distinguishing between common background activity and potential signal-like events. Based on their behavior, selection conditions are later applied to identify events of interest.

Before moving on to more detailed and stringent selection criteria, each slice must first meet a set of basic requirements to ensure that it corresponds to a physically meaningful event:

- **Minimum activity requirement:** Each slice includes hits from both the XZ and YZ detector views, and must therefore have at least three hits in each view to provide sufficient information for a reliable event reconstruction.

- **Through-going requirement:** Magnetic monopoles, due to their extremely high energies, would traverse the detector without being stopped; the amount of energy they deposit in the detector is negligible compared to their total kinetic energy. For each slice, at least two hits close to two different surfaces are required, in a way that is consistent with a track that fully crosses the detector. A surface hit is defined as a hit that occurs within 35 cells or 15 planes of the detector surface.

- **Space matching requirement:** The hits in both the XZ and YZ views must have at least three overlapping planes. The overlapping planes are defined as:

$$P_{\text{overlap}} = \min\left(P_{\text{xmax}},\, P_{\text{ymax}}\right) - \max\left(P_{\text{xmin}},\, P_{\text{ymin}}\right). \tag{4.1}$$

  Here, P_{xmax} (P_{ymax}) and P_{xmin} (P_{ymin}) represent the maximum and minimum plane indices of the hits in the XZ (YZ) view, respectively. This requirement ensures that the hits are spatially correlated and that enough of them are available for a track to be reconstructed in a later stage of the analysis.

- **Time matching requirement:** Similarly, the hits of a slice in each view must have a time overlap greater than zero. The overlap in time is determined by:

$$T_{\text{overlap}} = \min\left(T_{\text{xmax}},\, T_{\text{ymax}}\right) - \max\left(T_{\text{xmin}},\, T_{\text{ymin}}\right) \tag{4.2}$$

  where T_{xmax} (T_{ymax}) and T_{xmin} (T_{ymin}) represent the maximum and minimum time values of the hits in the XZ (YZ) view, respectively. This requirement ensures that the hits are time-correlated.

These basic requirements filter out random or poorly defined slices. Following this initial filtering, each slice is subjected to a more stringent set of selection criteria, which are designed to increase sensitivity to signal-like events while keeping the overall trigger rate at a manageable level. These criteria are selected to achieve high signal detection efficiency and strong suppression of background activity.

- **Minimum hits along the length of the slice:** Monopoles are expected to produce a relatively larger number of hits along the trajectory. We compute the hit density as the total number of hits divided by the diagonal length of the slice. The diagonal length of the slice is given by

$$l = \sqrt{\Delta X^2 + \Delta Y^2 + \Delta Z^2}, \tag{4.3}$$

where $\Delta X = \max(\text{Cell}_{XZ}) - \min(\text{Cell}_{XZ})$, and $\Delta Y = \max(\text{Cell}_{YZ}) - \min(\text{Cell}_{YZ})$, and $\Delta Z = 1.67 \times [\max(\text{Plane}) - \min(\text{Plane})]$. The factor of 1.67 accounts for the detector geometry, as the plane width (6.65 cm) is 1.67 times the cell width (3.99 cm), ensuring that ΔZ is expressed in units consistent with ΔX and ΔY. The threshold was fixed at 0.44.

- **Minimum cells per slice length in the XZ (YZ) view:** This condition requires a minimum number of cells in a slice divided by the length of the slice in the XZ (YZ) view. A cell with multiple hits at different times is only counted once. The slice length in the XZ (YZ) view is given by $\sqrt{\Delta X^2 + \Delta Z^2}$ ($\sqrt{\Delta Y^2 + \Delta Z^2}$).

- **Maximum standard deviation of hits per plane in the XZ (YZ) view:** Monopoles are expected to produce roughly a uniform number of hits in each plane, and the number of hits per plane should remain approximately constant, resulting in a small standard deviation. In contrast, cosmic-ray showers exhibit a larger variation in the number of hits per plane, and thus a larger standard deviation. This selection is imposed on the standard deviation of the hit count per plane in the XZ (YZ) view. The threshold is set to 1.25 for the XZ view and 1.2 for the YZ view.

- **Maximum ADC-weighted offset from the center in the XZ (YZ) view:** For monopoles, because they are expected to deposit energy uniformly, their ADC-weighted center is expected to be close to the geometrical center (although effects such as light attenuation, electronic noise, and other factors can introduce a small displacement). In contrast, high-energy cosmic muons produce localized high-energy hits through Bremsstrahlung radiation. As a result, their ADC-weighted center is significantly displaced from their geometrical center. The maximum ADC-weighted offset from the center along the Z direction in the XZ (YZ) view is determined using the following

equation:

$$\text{OffCenter}_{\text{max}} = \frac{\sum(\text{ADC}\,(\text{plane} - \text{min_plane}))}{\sum \text{ADC}\,\sum(\text{plane} - \text{min_plane})} - 0.5. \tag{4.4}$$

For both views, the threshold is fixed at 0.13.

- **Minimum fraction of hits in overlapping planes:** For a slice to be reconstructed in 3D during the offline analysis, the hits in the XZ and YZ views must occur within a closely corresponding set of planes. The fraction of hits within a slice that lie in the XZ and YZ overlap planes is given by

$$\frac{\text{Number of hits in overlapping planes}}{\text{Total number of hits in the slice}}, \tag{4.5}$$

where the definition of overlapping planes is given in Equation 4.1. Slices in which only a small proportion of hits are contained within the overlapping planes are discarded. The cut value for this requirement is set to 0.45 in each view.

- **Minimum number of surface hits:** Because monopoles are expected to traverse the detector completely without stopping, a minimum number of surface hits is required. A surface hit is defined as occurring within 35 cells or 15 planes of the detector boundary. The cut is chosen to be 22.

- **Minimum slice length:** Background events that pass the earlier selection can be localized within relatively small regions. To reduce their contribution, a lower threshold is imposed on the 3D slice length, as defined in Equation 4.3. Any slice with a length below 80 cells width (approximately 3.2 m) is rejected.

4.2 Trigger Efficiency

Trigger efficiency is defined as the ratio between the number of monopole events selected by the ionization-based monopole trigger and the total number of monopole events gener-

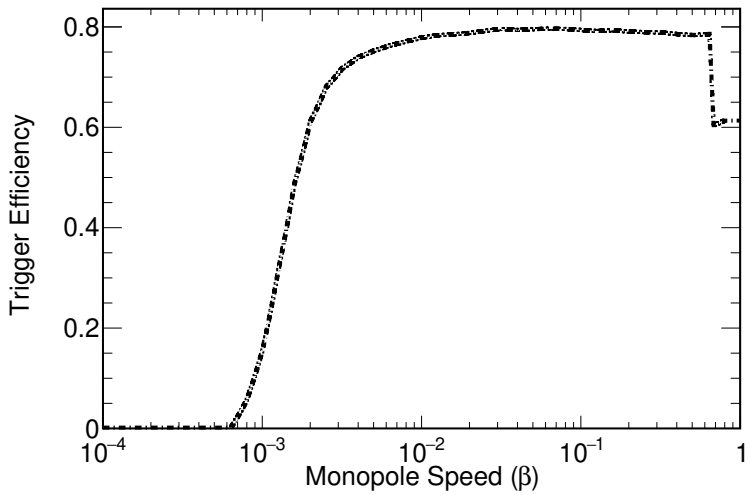


Figure 4.2: Trigger efficiency as a function of monopole velocity.

ated in the MC sample. Figure 4.2 presents the estimated trigger efficiency using simulated monopole samples in the full range of values β. For monopoles with relatively high velocities, the trigger efficiency does not exhibit a further increase, but instead saturates. The dominant source of efficiency loss is their trajectories within the detector. Monopoles moving through the detector on trajectories that are nearly vertical are more likely to pass through the gaps between adjacent planes or to intersect only a few vertical cells, leading to an insufficient number of cell hits for reliable slice reconstruction. Additionally, isotropically distributed monopoles may traverse the detector volume near its corners, which can result in very few or even no recorded hits. Both of these effects result in an insufficient number of hits available for slice formation and, consequently, in a degradation of the trigger efficiency over the entire velocity range. An additional reduction in trigger efficiency for slower monopoles is caused by their smaller energy deposition in the detector; such monopoles do not satisfy the minimum ADC threshold requirement.

The decrease in trigger efficiency observed above the Cherenkov threshold is caused by optical crosstalk. We processed the simulated crosstalk sample (see Section 3.7) with

the trigger algorithm, and it is observed that crosstalk-induced hits in the first few planes lead to failure of one of the trigger criteria. As mentioned in the previous section, the monopole trigger requires a low standard deviation of hits per plane in the XZ and YZ views because monopoles are expected to produce an approximately uniform hit count in each plane. However, in the presence of crosstalk, the first few planes impacted by the excess hits show an increased standard deviation, causing the corresponding slice to fail the particular trigger condition.

4.3 Data Set and Live Time

The magnetic monopole search based on ionization presented in this thesis uses data collected by the NOvA FD from November 2015 through February 2025. The resulting data set corresponds to a total of about 2,904 days during which the detector was actively collecting data. Not all of this time can be used directly for analysis. Each raw data file must pass NOvA detector-specific quality checks to be included in the good quality sample. Some parts of the data are removed if they do not meet the detector quality requirements or if the trigger is not fully operational. After applying these corrections, the effective good live time for the analysis is 2,713 days, hereafter referred to as the detector *live time*.

Chapter 5

The Analysis Strategy

Because the online trigger system does not perform a complete 3D reconstruction, events that meet trigger requirements are subsequently processed during an offline analysis stage, in which more sophisticated reconstruction algorithms are used. In this chapter, we present the complete offline analysis chain. Section 5.1 presents the reconstruction procedure, including 3D tracks, energy, and velocity. This is followed by the evaluation of the overall reconstruction performance and a validation of the method in Sections 5.2 and 5.3, respectively. The signal selection strategy is presented in Section 5.4, which describes both the preselection requirements and the final event selection criteria. The procedure for estimating the background in the signal region, using sideband techniques and muon bundle samples (see Section 3.7), is presented in Section 5.5. Finally, the results, derived from 2713 days of FD data, are reported in Section 5.6.

5.1 Reconstruction

Reconstruction starts by identifying individual detector hits and grouping those that are close in space and time into slices, following a procedure similar to that used at the trigger level. From each slice, two-dimensional (2D) tracks are then reconstructed in both detector views, and these are finally combined to obtain a complete 3D track.

This detailed reconstruction makes it possible to determine key physical quantities that separate monopoles from the cosmic background, including particle velocity, track length, energy loss, etc. These reconstructed quantities form the basis for further analysis with identification of signal-like events.

5.1.1 3D Track Reconstruction

The reconstruction process starts with the formation of slices that contain hits from both XZ and YZ views of the detector. A minimum of three hits are required for each view to proceed, and the hits in the two views must overlap both in position and in time to ensure that they originate from the same physical event. This is evaluated through overlapping planes and time, as discussed in Section 4.1.2.

Once these conditions are satisfied, the 2D tracks in each view are reconstructed separately by fitting a straight line to the corresponding set of hits. The line is obtained by minimizing the sum of squared perpendicular distances between the hits and the track,

$$\chi^2 = \sum_i w_i d_i^2, \tag{5.1}$$

where d_i denotes the distance between the i-th hit and the reconstructed track, and w_i is a weight reflecting the signal strength of that hit. This method ensures that hits with large ADC values contribute more significantly, resulting in a more reliable determination of the monopole trajectory. Following the initial fit, hits that lie far from the fitted track are classified as outliers and removed. A 2D track is then successfully reconstructed if at least three hits remain after this filtering step.

2D tracks from the two views are combined into a 3D track only when they are consistent in space and time. The complete 3D trajectory is then reconstructed by combining the two views and performing linear interpolation along the detector, generating points (x_i, y_i, z_i) that describe the trajectory of the particle.

5.1.2 Reconstruction of Energy Deposition and Velocity

With the 3D tracks reconstructed, the position of each hit along the detector directly gives the distance to the readout end. This distance is used to correct for signal attenuation, providing a calibrated estimate of the deposited energy. In addition, the timing information of

each hit is refined, with hits that lie outside a few standard deviations of the average track time being removed to suppress unrelated detector activity. At the end of this procedure, each track is characterized by its trajectory in the detector, timing information, and energy deposition.

The velocity of the reconstructed track is determined by using the position and time information of the hits along the trajectory. For each hit with coordinates (x_i, y_i, z_i, t_i), the distance from a reference point on the track is calculated. The reference point is chosen as the first hit (with the smallest value of z), given by (x_1, y_1, z_1, t_1). The distance is defined as

$$l_i = \sqrt{(x_i - x_1)^2 + (y_i - y_1)^2 + (z_i - z_1)^2}. \tag{5.2}$$

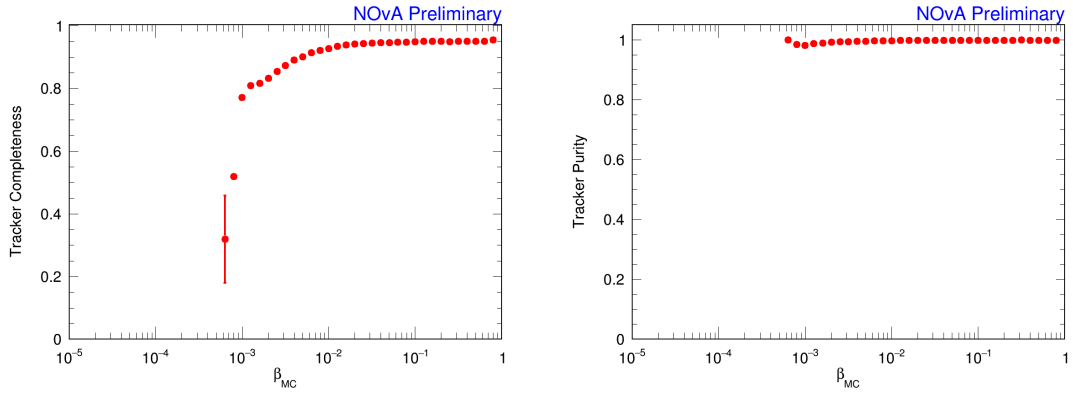
Then a linear fit is performed between l_i and t_i, and the slope of this fit is taken as the reconstructed velocity.

5.2 Reconstruction Performance

To assess the performance of the monopole track reconstruction, we use the overlaid monopole sample (see Section 3.6) to compute two complementary metrics, called track completeness and track purity.

1. **Track Completeness:** Track completeness is defined as the ratio of the number of monopole hits identified on the track to the total number of simulated monopole hits. A completeness value of 1 indicates that all simulated hits are successfully reconstructed, while a value of 0 means that none of the simulated hits are recovered. Figure 5.1a shows the completeness as a function of the generated β.

2. **Track Purity:** Track purity, on the other hand, determines how clean the reconstructed track is, i.e., how free it is from background contamination. It is defined

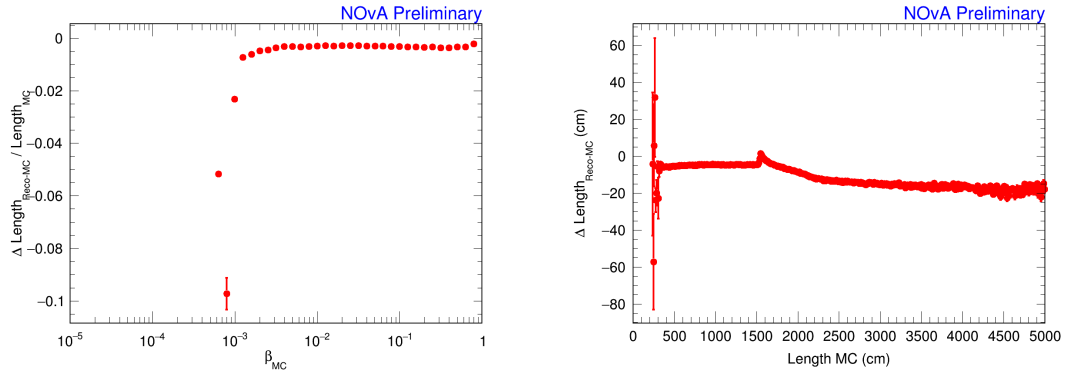


(a) (b)

Figure 5.1: Tracker performance vs. true velocity: (a) completeness in tracks and (b) purity in tracks.

as the ratio of the number of monopole hits to the total number of hits in the reconstructed track, including both monopole and cosmic hits. A purity of 1 indicates that all hits on the track belong to the monopole, whereas a purity of 0 means that none of the hits originate from the monopole. Figure 5.1b shows the purity as a function of the generated β.

For very slow monopoles, there are very few hits for reliable reconstruction of the tracks. As a result, the completeness and purity in this region are low and are affected by large statistical uncertainties, especially for $\beta < 10^{-3}$. In general, the reconstructed tracks exhibit high purity (close to unity) for $\beta > 10^{-3}$, indicating minimal background contamination. The completeness also improves significantly for $\beta > 10^{-2}$, for which most of the monopole hits are successfully recovered. In subsequent analysis, monopole tracks with purity ≥ 0.5 and completeness ≥ 0.5 are classified as signal.



(a) (b)

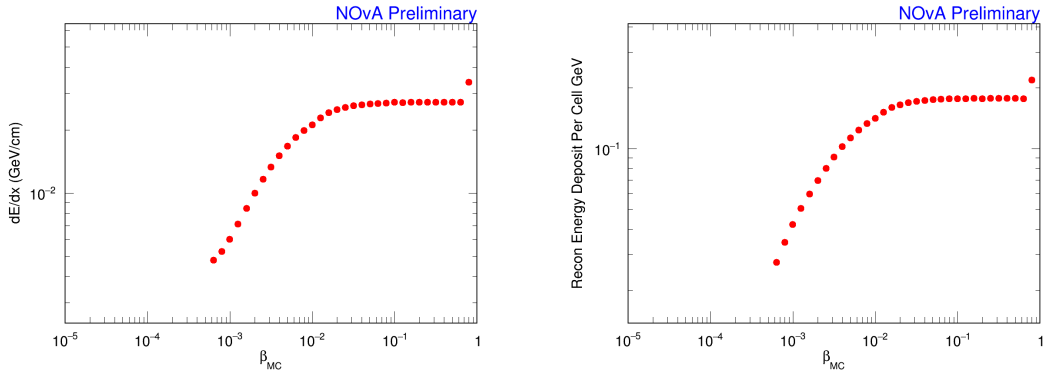
Figure 5.2: Comparison of track length: (a) The relative difference between reconstructed and true track length, obtained by dividing their difference by the true track length, as a function of the true velocity, and (b) the absolute difference between reconstructed and true track length as a function of the true track length. The kink observed in this plot is associated with the dimensions of the FD.

5.3 Reconstruction Validation

In this section, the reconstructed quantities are evaluated against the MC truth information in order to validate the performance of the reconstruction algorithms.

5.3.1 Reconstructed and True Track Length

Figure 5.2a shows the relative error of the reconstructed track length as a function of the true velocity of the MC sample. For $\beta > 10^{-3}$, the reconstructed track length is in good agreement with the MC track length. Figure 5.2b displays the absolute difference between the reconstructed and true track lengths versus the true track length. This distribution demonstrates that the reconstruction performs poorly for short MC tracks and, therefore, the event selection, described in the following sections, requires a condition of more than 20 hits in each view and a minimum track length of 5 m to reject these poorly reconstructed tracks.



(a) (b)

Figure 5.3: Comparison of energy deposition as a function of the true velocity β. (a) dE/dx as a function of the true velocity. (b) Energy deposited per cell as a function of the true velocity. The rise in dE/dx and deposited energy per cell above $\beta \approx 0.68$ is caused by Cherenkov light emission once the Cherenkov threshold is exceeded.

5.3.2 Energy Deposition

The total reconstructed energy deposited by a monopole in the detector is obtained by summing the contributions of all cells traversed by the monopole track. Figure 5.3a displays dE/dx as a function of monopole velocity, where dE/dx is defined as the total reconstructed energy divided by the length of the reconstructed track. Figure 5.3b shows the energy deposited per cell, defined as the total energy divided by the total number of hits, as a function of velocity. In both plots, the Cherenkov effect is clearly visible for $\beta \gtrsim 0.68$.

5.4 Event Selection

At this point, all variables required to distinguish the monopole signal from background events have been reconstructed. The event selection for this search proceeds in two stages: a preselection followed by a final selection. The preselection step applies relatively loose criteria designed to reject obvious background-like events while maintaining high efficiency for the signal. The final selection then imposes more stringent requirements to further sup-

press any remaining background. The data sets used to tune the signal selection criteria are described below.

As discussed in Section 4.3, this analysis uses FD data recorded from 2015 through 2025, corresponding to a total effective live time of 2,713 days. For optimization of event selection criteria, a small fraction of ionization-based triggered data is used, representing roughly 0.5% of the full data set and taken uniformly from the period between 2015 and 2019.

For the signal sample, we use overlaid events that meet the trigger requirements, and we further require that the reconstructed tracks have purity and completeness greater than 50%. With these data and signal samples ready, along with the reconstructed variables, we now specify the preselection criteria used to select candidate events.

5.4.1 Preselection Criteria

The preselection criteria are motivated by our physical understanding of the underlying processes and the distinct characteristics of the signal and background samples. In particular, the requirements are based on the anticipated properties of magnetic monopoles: they produce strong ionization, move slower than light, and pass through the entire detector. Due to the limited number of background events, the selection cuts are kept simple instead of being optimized using a formal figure of merit. The goal is to eliminate maximum background while maintaining signal efficiency as high as possible. The principal variables used to separate the signal from the background are as follows:

1. Long track: A monopole is anticipated to leave a long, straight trajectory and therefore produce a large number of hits along its path. To suppress background events and discard poorly reconstructed monopole tracks, we require that, in each view, the reconstructed tracks must have more than 20 associated hits and a reconstructed length of more than 5 m.

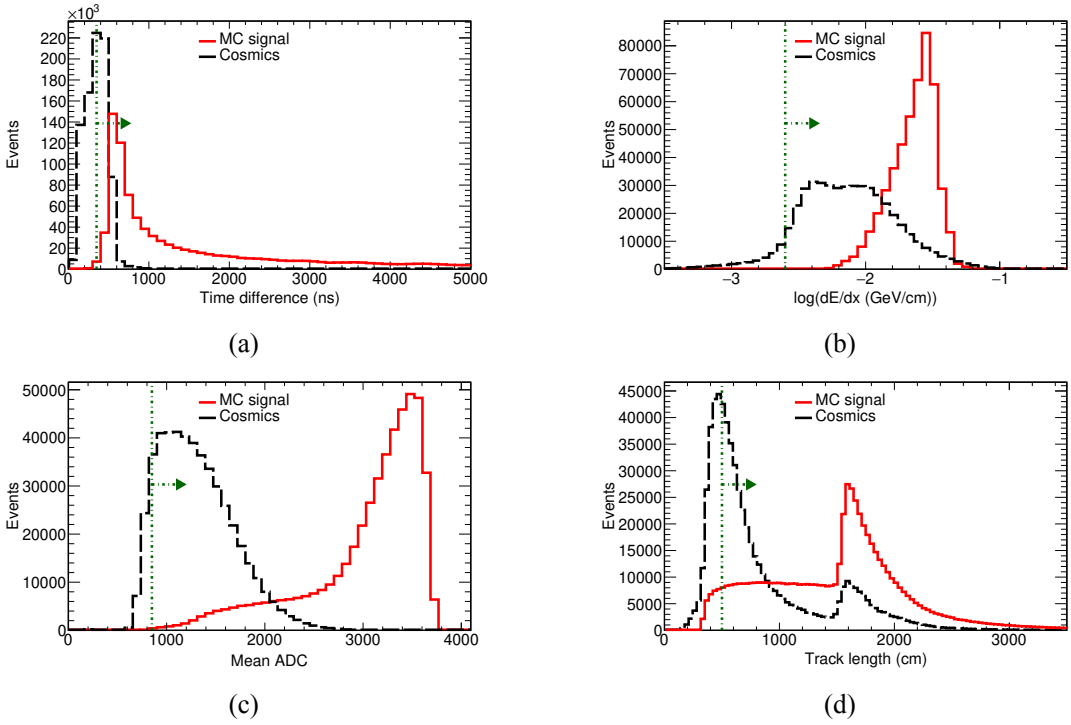


Figure 5.4: Distributions of the: (a) time difference between the first and the last hits, (b) log dE/dx, (c) mean ADC, (d) reconstructed track length. For each distribution here, all other selection requirements are imposed except for the variable shown in that plot.

2. High energy deposition: Monopoles are highly ionizing and deposit a substantial amount of energy in the detector. To distinguish them from the background, we impose a loose selection on the energy deposited per unit length, requiring $dE/dx > 2.5 \times 10^{-3}\,\mathrm{GeV/cm}$. This loose cut ensures minimal dependence on the underlying energy loss model. In addition, monopoles are expected to produce a larger mean ADC, defined as the total ADC divided by the number of hits. Therefore, we also apply a loose cut to the mean ADC, requiring it to be more than 850.

3. Large transit time: Since monopoles move much slower than cosmic muons, they take longer time to pass through the detector. We therefore require the reconstructed velocity to be less than the speed of light and the time difference between the first

	Signal			Background		
Cut	Tracks	Rejected	Percentage	Tracks	Rejected	Percentage
hits in x view > 20	2,001,744	48,971	2.4%	29,032,864	5,508,717	18.9%
hits in y view > 20	1,952,773	39,151	2.0%	23,524,147	4,186,965	17.8%
$dE/dx > 2.5 \times 10^{-3}\,\mathrm{GeV/cm}$	1,913,622	118	0.0062%	19,337,182	15,254,691	78.9%
max(TDC)−min(TDC) $> 350\,\mathrm{ns}$	1,913,504	8,838	0.5%	4,082,491	2,628,952	64.4%
$\beta < 1$	1,904,666	0	0%	1,453,539	438,156	30.1%
track length > 500 cm	1,904,666	94,380	4.9%	1,015,383	225,570	22.2%
exit D < 50 cm	1,810,286	6,797	0.4%	789,813	216,989	27.5%
entry D < 50 cm	1,803,133	6,973	0.4%	517,517	24,031	4.6%
mean ADC > 850	1,796,160	938	0.05%	493,486	45,992	9.3%
Overall Rejection		206,522	10.31%		28,585,370	98.4%

Table 5.1: Summary of preselection criteria applied for track rejection in both signal and background samples.

and last hits on the track to be more than 350 ns.

4. Through-going: Monopoles are penetrating particles and are expected to enter and exit the detector. Therefore, both the entry and exit points of the track must be within 50 cm of two distinct detector surfaces.

Figure 5.4 presents some of the key observables introduced above to distinguish the signal from the background in the preselection stage. The figure shows the distribution of one variable at a time, obtained by applying the full set of preselection criteria except for the requirement on the variable plotted. This procedure is essential to study the behavior of each variable individually while still taking into account the influence of all the other selection cuts. The arrow denotes the specific cut for the variable plotted.

Table 5.1 summarizes the fraction of reconstructed tracks rejected by the preselection requirements: 98.4% of the background tracks and 10.3% of the signal tracks are discarded.

These preselection criteria reduced the background as much as possible while still retaining the maximum signal efficiency.

5.4.2 Final Selection Criteria

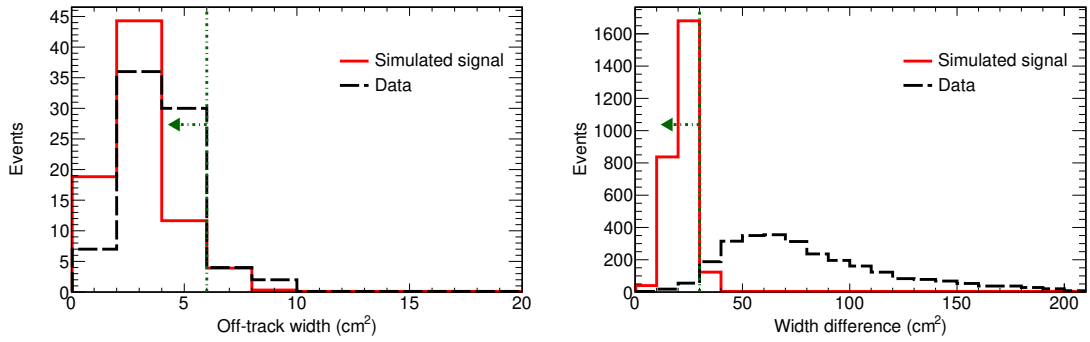
More stringent selection criteria are applied in the final event selection stage to retain the majority of monopole signal events while rejecting background tracks that satisfy the pre-selection requirements.

Track Width

Because of their large mass and momentum, monopoles are not expected to experience significant multiple Coulomb scattering. Nor do they experience hadronic interactions. As a result, they should leave relatively narrow tracks compared to those from Standard Model cosmic rays, which can generate large but irregular energy depositions.

The track width is defined as the mean squared transverse distance of the hits from the fitted track line. It is evaluated by adding the squared perpendicular distances of all hits to the reconstructed trajectory. Based on this quantity, two track-width-related observables are introduced for signal selection:

- Off-track width: defined as the maximum, taken over the XZ and YZ views, of the sum of squared distances to the reconstructed track for all hits whose readout cells are not directly intersected by the fitted track line and then dividing by the total number of hits.
- Width difference: defined as the maximum, taken over the XZ and YZ views, of the difference between the maximum and minimum values of the track width observed along the track.



(a) (b)

Figure 5.5: Distributions of (a) off-track width and (b) width difference for data and the simulated signal sample. In each panel, the simulated event distribution is normalized in area to match the data. The left (right) distribution corresponds to events that pass the trigger and selection criteria 1–4 and 6 (1–5). The dashed vertical line with an arrow indicates the cut value of the variable; this cut is not applied to the events shown in the distributions.

Figure 5.5 presents the distributions of these track width related variables used to differentiate monopole candidates from the cosmic-ray background. The selection criteria are as follows:

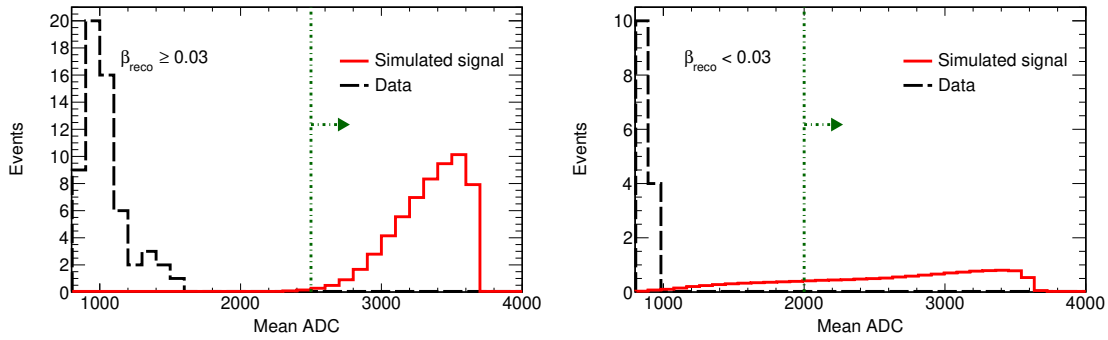
5. Off-track width ≤ 6 cm^2;

6. Width difference ≤ 30 cm^2.

Although only 0.5% of the full data set is used to optimize these selection cuts, the complete data sample is used in Figure 5.5 to display the resulting distributions, thereby providing improved statistics for data.

Mean ADC

The mean ADC serves as the final discriminating variable for identifying monopole candidates in the data set. Due to their substantially higher energy deposition in the detector relative to cosmic rays, monopoles are expected to have larger mean ADC values. Figure 5.6 presents the distribution of the mean ADC, with all selection criteria applied except



(a) (b)

Figure 5.6: Distributions of mean ADC for data and simulated signal events, shown for events with (a) $\beta_{\text{reco}} \geq 0.03$, and (b) $\beta_{\text{reco}} < 0.03$. In each plot, the simulated event distribution is area normalized to the data for visual comparison. In each case, trigger and selection requirements 1–6 have been applied. These plots are used to define the signal region. The dashed vertical line with an arrow indicates the cut value of the variable; note that this cut is not applied to the distribution shown.

the requirement on the mean ADC itself. Selection cuts 5 and 6 suppress the majority of irregular or clustered cosmic-ray-induced activity, resulting in only a small residual background.

Based on this distribution, distinct mean ADC thresholds are defined for the higher and lower-β monopoles to maintain high signal efficiency throughout the entire velocity range. Higher-β monopoles that produce high ionization allow for a more stringent requirement on the mean ADC, whereas lower-β monopoles, which may be less ionizing, require a more relaxed threshold. A study of several β values shows that relaxing the mean ADC requirement for $\beta < 0.03$ results in a negligible efficiency loss for low-β monopoles. The corresponding mean ADC selection requirements are the following:

7. Mean ADC ≥ 2500 for $\beta_{\text{reco}} \geq 0.03$;

8. Mean ADC ≥ 2000 for $\beta_{\text{reco}} < 0.03$.

In summary, the track-width and mean ADC threshold requirements (selection crite-

Ranges with β	Initial Events	Triggered	Preselected	Final selection cuts
2 cm / $\beta = 0.995$	10000	8340	7546	48
0.4 cm / $\beta = 0.9$	10000	8326	7565	4456
0.3 cm / $\beta = 0.85$	10000	8378	7598	5311
0.22 cm / $\beta = 0.8$	10000	8356	7513	5795
0.16 cm / $\beta = 0.75$	10000	8322	7478	6104
0.12 cm / $\beta = 0.7$	10000	8351	7486	6306
Single Monopole	10000	8221	7501	6702

Table 5.2: Selection efficiencies for monopole bundles. In the first column, β represents the monopole velocity, and the values given in centimeters correspond to the maximum transverse ranges of the generated delta rays, which are equal to the radius of the monopole bundle within the custom simulation.

ria 5-8) described in this section form the final set of requirements for the identification and detection of magnetic monopoles and, therefore, specify the signal region used in this analysis. Before showing the resulting selection efficiency, we evaluate how delta rays and optical crosstalk affect the performance of these selection criteria. Both effects can lead to an apparent widening of the reconstructed monopole track above the Cherenkov threshold, which can result in reduced selection efficiency. To evaluate the impact of these effects, we passed the simulated sample for delta rays and crosstalk, as discussed in detail in Section 3.7, through the entire analysis chain.

Impact of Delta Rays on Selection Efficiency

Monopole bundles (see Section 3.7) with different radii are passed through the entire analysis chain. Table 5.2 lists how many monopole bundles of each radius are retained by the fast monopole trigger, by the preselection, and by the final selection criteria. The selection efficiency remains high for tracks whose delta-ray range is 1.6 mm, but it decreases for relatively broader tracks and shows a sharp reduction once the transverse range is about 2 cm.

Events	Initial	Triggered	Preselected	Final selected
Monopole ($\beta = 0.8$) without cross-talk	10000	8221	7501	6702
Monopole ($\beta = 0.8$) with cross-talk	10000	6302	5676	4596
Monopole ($\beta = 0.85$) with cross-talk	10000	6289	5597	4487
Monopole ($\beta = 0.9$) with cross-talk	10000	6257	5624	4519

Table 5.3: Selection efficiencies with crosstalk

Impact of Crosstalk on Selection Efficiency

Simulated crosstalk-induced monopole events (see Section 3.7) are processed through the complete analysis chain. Table 5.3 summarizes the simulated monopole detection efficiency, evaluated both in the presence and absence of crosstalk. For monopoles with velocities above the Cherenkov threshold, the efficiencies under crosstalk conditions are reported at $\beta = 0.8$, $\beta = 0.85$, and $\beta = 0.9$. The inclusion of crosstalk results in an additional reduction in trigger efficiency by approximately 25% (see Figure 4.2) relative to the case without crosstalk. This significant loss mainly arises from the trigger condition based on the standard deviation of hits per plane in the XZ (YZ) view. When crosstalk occurs, the first plane impacted by a cluster of spurious hits increases the measured standard deviation, causing the event to fail this trigger requirement. In addition, crosstalk induces another $\sim 30\%$ reduction in the final selection efficiency compared to configurations without crosstalk. This additional loss in efficiency is predominantly due to the selection requirements imposed on the track width.

5.4.3 Overall Selection Efficiency

The overall efficiency is defined as the ratio of the number of generated monopoles that satisfy all selection requirements, including trigger, preselection, and final selection criteria, to the total number of generated monopoles, with the effects of delta-ray production and optical crosstalk explicitly taken into account. For monopole velocities exceeding the

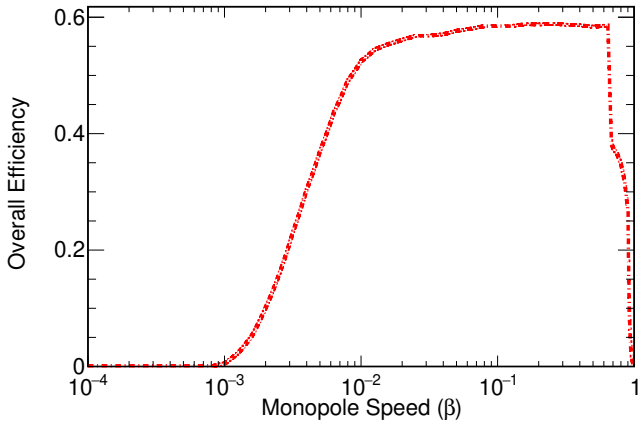


Figure 5.7: Overall efficiency as a function of monopole velocity.

Cherenkov threshold, the overall efficiency decreases, primarily due to the impact of delta-ray production and optical crosstalk. Figure 5.7 shows the overall efficiency as a function of monopole velocity.

5.5 Estimation of Background in Signal Region

The estimation of background contributions in the signal region is achieved by two complementary approaches. The first method is based on dedicated simulations of cosmogenic muon bundle events, as described in Section 3.8, and is used to evaluate the probability of such backgrounds mimicking the monopole signal. The second method relies on a data-driven technique, where the background is extrapolated into the signal region using a side-band study based on the mean ADC distribution. Together, these approaches provide a robust estimate of the expected background, which is discussed below.

5.5.1 Cosmogenic Muon Bundles

In this method, the simulated muon bundles (see Section 3.8) are passed through the complete analysis chain, including trigger, preselection and final selection. However, for this specific study, the final selection criteria are relaxed to obtain sufficient statistics in the

signal region, allowing an estimation of the background contribution arising from this effect. Therefore, the estimates obtained for this study are very conservative. The results for different configurations are summarized below:

1. **Two Muons with Time Offset:** In this configuration, two muons with energies of 100 ± 5 GeV are generated with a time separation and the same initial position. None of these events survives the full selection chain and enters the signal region.

2. **Two Muons Along the Same Trajectory:** Here, two muons with similar energies are generated simultaneously along the same path. After the complete analysis chain, no events are found to meet the signal selection criteria.

3. **Muon Bundles:** Muon bundles consisting of 3, 4, and 5 muons are also simulated and analyzed. Each bundle contains muons with energies of 100 ± 5 GeV, produced simultaneously along the same trajectory. Of 100,000 simulated events for each configuration, no events from the 3-muon sample pass the selection, while 1 event from the 4-muon sample and 13 events from the 5-muon sample are found in the signal region.

Search for Muon Bundles in Cosmics

We searched for candidate 4-muon and 5-muon bundles in the minimum-bias cosmics data collected by the FD. Within a bundle, the muons are expected to enter the detector with random mutual separations of the order of 100 cm, consistent with their origin in extensive air showers and subsequent multiple Coulomb scattering.

In data corresponding to an effective live time of four hours, we identified ten 4-muon bundles with all reconstructed entry points lying within 100 cm of each other; no 5-muon bundles satisfying this criterion were observed. For the purposes of this study, an N-muon bundle is defined as an event in which N distinct tracks are reconstructed. Muons entering

the detector with very small mutual separations may not be resolved individually and thus may not be reconstructed as separate tracks; this effect is incorporated into our study.

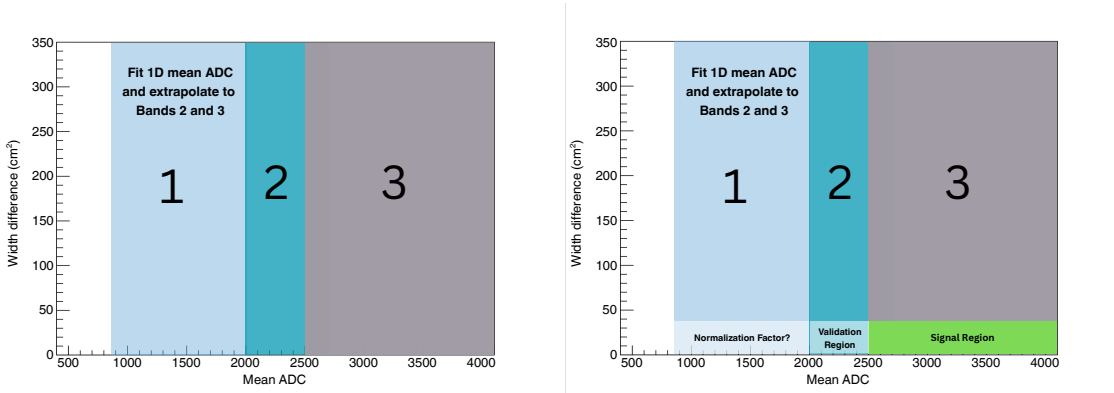
Assuming that multiple scattering can produce similar events in which the muons are distributed with random positions within a 100 cm radius, a toy MC simulation was used to estimate the likelihood that all muons in a bundle enter within a much smaller region. The simulation indicates that 5×10^{-7} of the 4-muon bundles and 5×10^{-8} of the 5-muon bundles have all entry points contained within a radius of 5 cm.

Combining observational data with simulation results, the expected background in the monopole signal region for an exposure of 2,713 days is 8×10^{-7} events from 4-muon bundles and $< 2 \times 10^{-7}$ events at 90% CL from 5-muon bundles. Bundles of even higher multiplicity are expected to have an even smaller probability of remaining sufficiently overlapping to mimic a monopole track. As noted previously, these background estimates are very conservative.

5.5.2 Sideband Study

The mean ADC is chosen as the main observable for the sideband analysis. The background distribution is first determined in the sideband region and then extrapolated to the signal region. As described in Section 5.4.2, the signal region is defined differently for $\beta \geq 0.03$ and $\beta < 0.03$. Therefore, the mean ADC sideband is studied separately for $\beta \geq 0.03$ and $\beta < 0.03$. This analysis is performed on the entire data set within the sideband region, while the signal region remains blinded. Although the background is estimated independently in the $\beta \geq 0.03$ and $\beta < 0.03$ regions, the same procedure is applied in both cases, as summarized below.

The 2D plane, defined by the mean ADC and the width difference after applying all selection criteria except the cuts to these variables themselves, is divided into three distinct regions, as illustrated in Figure 5.8a. In the first region (Band 1), the one-dimensional



(a) (b)

Figure 5.8: Illustration of the background estimation method: (a) the 2D distribution of mean ADC vs. width difference is partitioned into three distinct bands. In Band 1, the corresponding 1D mean ADC distribution is fitted with an exponential decay function, which is then extrapolated to Bands 2 and 3; and (b) indicate the normalization factor associated with the Band 1, as well as the validation and signal regions.

(1D) distribution of the mean ADC is well described by an exponential function. The fit parameters obtained in this region are then used to extrapolate and estimate the background contribution in the higher-ADC regions (Bands 2 and 3).

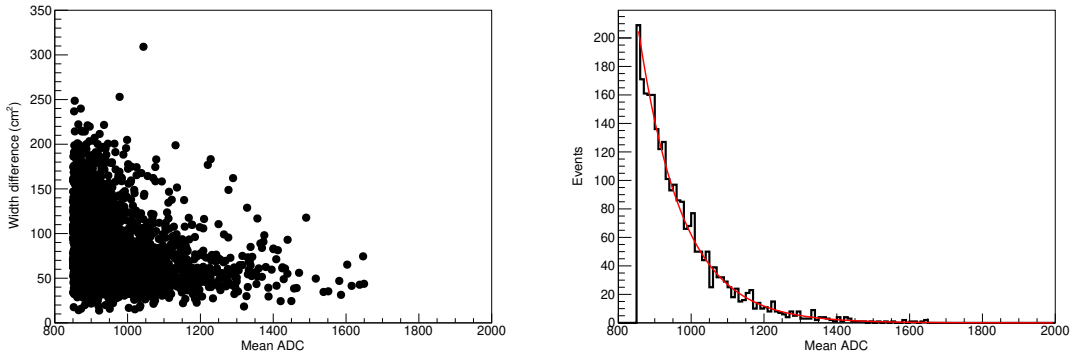
This extrapolation provides a background estimate across the full domain of Bands 2 and 3. To extract the background yield specifically in the regions of interest, such as the validation and signal regions shown in Figure 5.8b, a normalization factor is derived using the event distribution in Band 1:

$$\frac{\text{Number of events with width difference} \leq 30}{\text{Total number of events in Band 1}}. \tag{5.3}$$

This normalization factor is used to rescale the extrapolated background in Bands 2 and 3, yielding the final background estimates in the validation and signal regions, respectively.

Estimation of Background for $\beta \geq 0.03$

In the high-β regime, the 2D space of the mean ADC and the width difference are divided as follows:



(a) (b)

Figure 5.9: Distribution of the sideband sample used to estimate the background for $\beta \geq 0.03$: (a) presents the 2D distribution of events in Band 1, and (b) shows the corresponding 1D distribution of the mean ADC, which is fitted with an exponential function of the form defined in Equation 5.4.

- **Band 1** $(850 <$ **mean ADC** $< 2000)$**:** The background distribution in this region, obtained after applying the trigger and preselection criteria as well as the selection cut on the off-track width, is shown in Figure 5.9a, and its corresponding 1D distribution of the mean ADC is shown in Figure 5.9b.

- **Band 2** $(2000 \leq$ **mean ADC** $< 2500)$**:** This range serves to test the validity of the background extrapolation.

- **Band 3** $($**mean ADC** $\geq 2500)$**:** Within this band, the signal region is determined by applying the normalization factor given in Equation 5.3.

1D mean ADC Distribution and Fit in Band 1

The 1D mean ADC distribution obtained from Band 1 (see Figure 5.9b) is described using an exponential function of the form

$$[P_0]\, e^{-[P_1]x}. \tag{5.4}$$

The resulting best-fit parameters are $P_0 = 2.5 \times 10^5$ and $P_1 = 8.3 \times 10^{-3}$. In this region, the normalization factor obtained from Equation 5.3 is $\frac{57}{2587}$, because 57 of the total 2587 events exhibit a width difference smaller than 30.

Extrapolation to Bands 2 and 3

The fitted exponential function is used to extrapolate the background contribution into Bands 2 and 3. For Band 2, the total background before normalization is found to be 0.2 ± 0.03. Applying the normalization factor yields the expected background in the validation region:

$$N_{\text{validation}} = \frac{57}{2587} \times (0.2 \pm 0.03) = 0.004 \pm 0.0006. \tag{5.5}$$

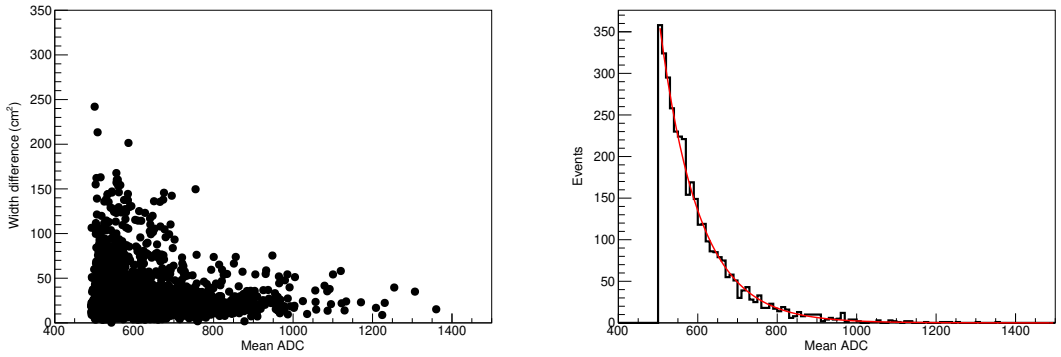
For Band 3, the total background before normalization is estimated as 0.003 ± 0.0008. Using the same normalization factor, the predicted background in the signal region is:

$$N_{\text{signal}} = \frac{57}{2587} \times (0.003 \pm 0.0008) = (7 \times 10^{-5}) \pm (1 \times 10^{-5}). \tag{5.6}$$

5.5.3 Estimation of Background for $\beta < 0.03$

For $\beta < 0.03$, several important changes are introduced. The mean ADC ranges that define the bands are modified, and the signal region is now specified by the mean ADC requirement given below.

- **Band 1 (500 < mean ADC < 1500):** Figure 5.10a presents the 2D scatter distribution of background events within Band 1, while the corresponding 1D distribution of the mean ADC is displayed in Figure 5.10b.
- **Band 2 (1500 $\leq$ mean ADC < 2000):** for validation.
- **Band 3 (mean ADC $\geq$ 2000):** for estimating the background in the signal region.



(a) (b)

Figure 5.10: Distribution of the sideband sample used to estimate the background for $\beta < 0.03$: (a) presents the 2D distribution of events in Band 1, and (b) shows the corresponding 1D distribution of the mean ADC, which is fitted with an exponential function of the form defined in Equation 5.4.

In addition, due to the very limited statistics in the sideband region, several preselection cuts are relaxed for the study $\beta < 0.03$. The trigger requirement is retained, but the preselection is modified by removing the dE/dx cut, the through-going cuts that required track entry and exit points to lie within 50 cm of the detector surface, and the requirement that each view contain more than 20 reconstructed hits. In addition, the mean ADC threshold is reduced from 850 to 500.

1D mean ADC Distribution and Fit in Band 1

The 1D mean ADC distribution is well described by the exponential function of the same form given in Equation 5.4 with best-fit parameters $[P_0] = 7 \times 10^4$ and $[P_1] = 1 \times 10^{-2}$.

Extrapolation to Bands 2 and 3

For $\beta < 0.03$, the extrapolation procedure gives an expected background of 0.10 ± 0.02 events in Band 2 and $(9.0 \pm 2.0) \times 10^{-4}$ events in Band 3. These values are obtained from a sample of 3670 background events in Band 1, selected using relaxed preselection

criteria. However, the final background estimate must instead be normalized to the number of background events observed in Band 1 after the complete set of selection cuts has been imposed.

Once all selection criteria are applied, 14 background events remain in Band 1. Therefore, the extrapolated background predictions for Bands 2 and 3 are scaled by a factor $\frac{14}{3670}$ and the estimated background in the validation region is:

$$N_{\text{validation}} = \frac{14}{3670} \times (0.10 \pm 0.02) = (3 \pm 0.6) \times 10^{-4}, \tag{5.7}$$

Similarly, the estimated background in the signal region is:

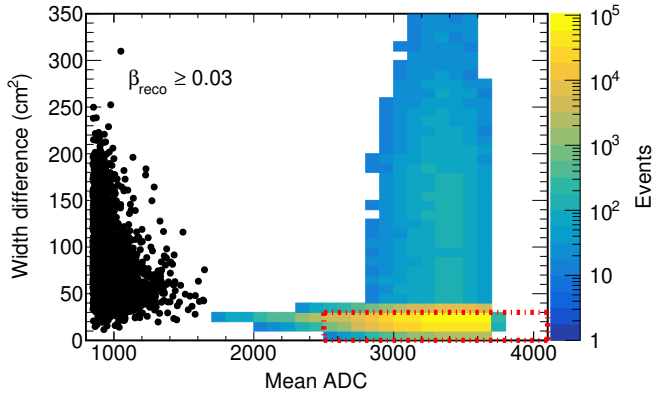
$$N_{\text{signal}} = \frac{14}{3670} \times (9.0 \pm 2.0) \times 10^{-4} = (3 \pm 0.6) \times 10^{-6}. \tag{5.8}$$

5.5.4 Validation of Background Estimates

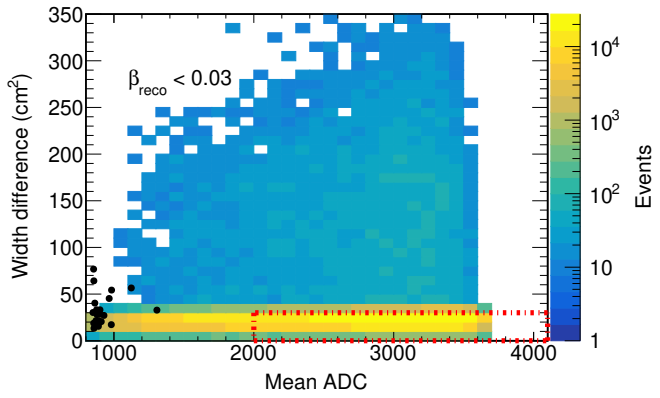
The next step is to verify the background estimation by comparing the predicted background in the validation regions with the corresponding data. For $\beta \geq 0.03$, the expected background in the validation region is the 0.004 ± 0.0006 events, with no events observed in the data. For $\beta < 0.03$, the expected background is $(3 \pm 0.6) \times 10^{-4}$ events in the validation region, and again no events are observed in the data. The lack of observed events is statistically consistent with the background expectations, indicating that the extrapolation method used to estimate these backgrounds is reliable within the stated uncertainties.

5.6 Observation of Data in the Signal Region

After finalizing all event selection criteria and validating the background estimation through the analysis of the sideband regions in the mean ADC distribution, the signal region is unblinded to determine whether any events are observed there in the full data set. This procedure is carried out only after committing to no further optimization or tuning of the



(a)



(b)

Figure 5.11: 2D distributions of simulated events (represented as colored heatmaps) overlaid with unblinded fast-monopole–triggered data (red markers) for (a) $\beta \geq 0.03$ and (b) $\beta < 0.03$. No data events are observed within the signal region, which is indicated by the dotted box.

selection, in order to prevent any potential bias in the analysis. As discussed in the previous section, the predicted background contribution in the signal region is found to be negligibly small. Based on the full data set corresponding to the live time of 2,713 days, no events are found in the specified signal region. Figure 5.11 shows the corresponding distributions for both the data and the simulated signal.

We further examined the candidate events located close to the signal region. For $\beta \geq 0.03$, the events that appear most signal-like are mainly through-going muons that pass near a corner of the detector, producing a track that only just exceeds the 5 m threshold. In contrast, for $\beta < 0.03$ these tracks are not short; instead, the reconstructed tracks in the two views are inconsistent. These events are determined to originate from two distinct tracks that occurred in nearly the same location but at slightly different times, which the reconstruction algorithm erroneously identified as a single track. While these events were already rejected by this analysis, a future analysis could reject them more robustly by implementing improved reconstruction techniques.

Since no events are observed in the signal region and the expected background is very negligible, the next step is to set an upper limit on the possible monopole flux, using our understanding of the monopole detection efficiency and the total exposure time of the detector. The exact statistical method used to derive this limit and the final numerical results is described in the next chapter.

Chapter 6

Results

This chapter gives a brief overview of the procedure used to calculate the upper limit on the magnetic monopole flux. The key factors that go into the calculation are the accessible solid angle, the projected detector area, the detector live time, and the overall detection efficiency. The chapter is organized as follows. Section 6.1 defines the accessible solid angle for a given monopole velocity in terms of the mass threshold above which the monopoles can reach the detector. The projected area, defined as the effective geometric cross section of the detector as seen by an incoming monopole, is briefly described in Section 6.2. The detection efficiency is discussed in greater detail in Section 6.3. Finally, the calculation of the upper flux limit is presented in Section 6.4 based on the observations obtained from the monopole-triggered data sample.

6.1 Accessible Solid Angle

For a fixed monopole mass and velocity β, we define the accessible region Ω as the subset of the incoming directions (solid angle) from which the monopoles can pass through the intervening material and reach the FD. This quantity is evaluated using dedicated numerical simulations that uses a simplified model of the Earth's interior and its density profile.

If the kinetic energy of the monopole is sufficiently large, it can pass completely through the Earth and reach the detector from any direction, giving full 4π angular acceptance. However, at lower energies, monopoles can arrive at the detector only by crossing the atmosphere and detector overburden, which leads to angular acceptance of approximately one half of the sky. The overburden protects the detector components from cosmic rays, and for the

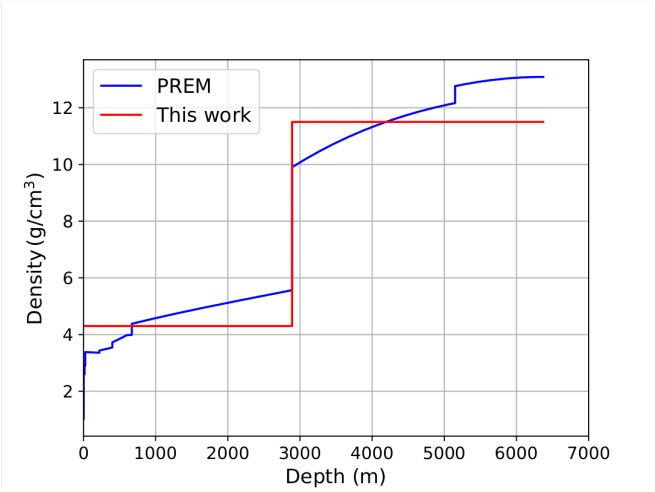


Figure 6.1: The solid curve shows the Earth's density profile as given in Ref. [6]; in this study, we adopt the simplified approximation indicated by the solid line.

FD, the combined concrete and barite roof system offers shielding equivalent to 9.86 feet of Earth [3].

To model this scenario, we used a geometry that includes the FD overburden and a simplified representation of the Earth, assigning effective compositions to its different layers in a procedure similar to that in Ref. [89]. The calculation relies on the stopping powers given in Equations 3.8, 3.10, and 3.14. In this model, the core and mantle of the Earth are treated as iron and silicon, respectively, the overburden is approximated as concrete, the detector is represented by paraffin as a scintillator-like material, and the atmosphere is modeled as air, using standard material definitions available in GEANT4. The density profile of the Earth is complex [6]; however, for our purposes it is sufficient to adopt a simplified model in which each layer is taken to have uniform density, as illustrated in Figure 6.1. With these assumptions, we can estimate the energy loss of the monopoles as they traverse each region. Figure 6.2 presents the stopping power for all materials considered in this work.

For each possible trajectory, we simulate the passage of the monopole through the detector and surrounding materials. Beginning with a very small velocity ($\beta = 10^{-5}$), we

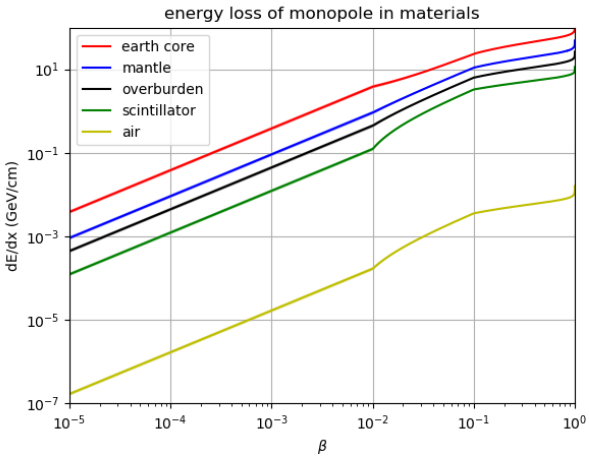
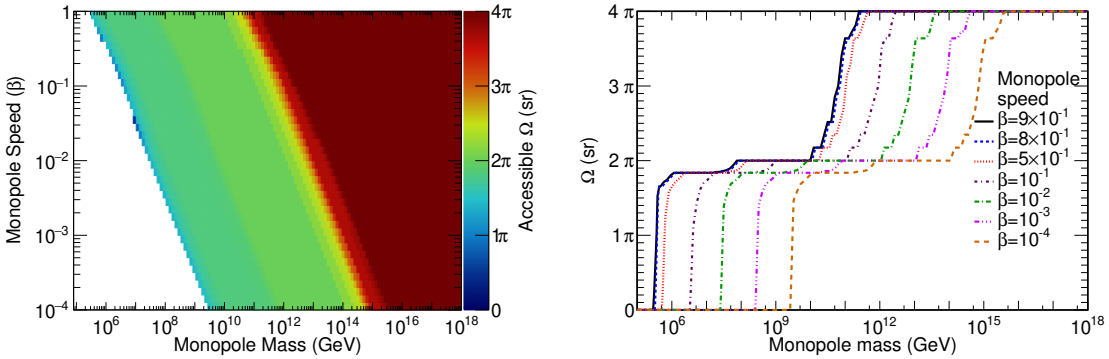


Figure 6.2: Stopping power of the monopole in the five media it passes through before reaching the detector, Earth's mantle and core, detector overburden, scintillator, and atmosphere, as a function of β. The stopping power formulas used in this study is based on the Equations 3.8 and 3.10, with a smooth linear interpolation used in the intermediate velocity range.



(a) (b)

Figure 6.3: (a) Solid angle coverage as a function of monopole velocity and mass. The coverage 4π means a monopole can arrive from any direction and still reach the detector, and (b) solid angle coverage as a function of shows monopole mass for specific monopole speeds, $\beta = 10^{-4}$, 10^{-3}, 10^{-2}, 10^{-1}, 5×10^{-1}, 8×10^{-1}, and 9×10^{-1}.

traced the trajectory, calculated the energy loss step by step, and updated the velocity in every segment. When the monopole leaves the atmosphere, we record its resulting velocity. In this way, we identify the minimum initial velocity needed for a monopole of a given mass to reach the detector along that trajectory. Any monopole with a larger velocity or mass would likewise be capable of reaching the detector. Figure 6.3a shows the solid angle as a function of the monopole mass and velocity, while Figure 6.3b displays the solid angle as a function of mass for selected monopole velocities. For $\beta \geq 10^{-3}$, the threshold mass for full 4π coverage is 10^{15} GeV, and for a 1π region it is 10^{9} GeV. The sensitivity further improves for lower-mass, high-velocity monopoles that can reach the detector through the atmosphere and minimal overburden. Monopoles with masses as low as 10^{7} GeV can reach the detector for $\beta > 0.1$.

6.2 Projected Surface Area

The projected surface area is the shadow area of a surface on a plane perpendicular to a given incoming direction. Thus, the effective area "seen" by an incoming monopole varies with its direction of travel. For a trajectory with unit vector $\hat{v}$, the projected area is given by the sum of the contributions from the detector faces, weighted by the angle between the trajectory and the corresponding surface normals:

$$A_{\text{proj}} = |\hat{v} \cdot \hat{n}_{\text{east}}|\, A_{\text{east}} + |\hat{v} \cdot \hat{n}_{\text{top}}|\, A_{\text{top}} + |\hat{v} \cdot \hat{n}_{\text{north}}|\, A_{\text{north}}. \tag{6.1}$$

Expressed in terms of the polar and azimuthal angles (θ, φ), where the y-axis is taken as the zenith direction and $\varphi = 0$ lies in the YZ-plane, this becomes

$$A_{\text{proj}}(\theta, \varphi) = |\sin\theta \sin\varphi|\, A_{yz} + |\cos\theta|\, A_{xz} + |\sin\theta \cos\varphi|\, A_{xy}. \tag{6.2}$$

To account for all possible incoming directions within the accessible region Ω, we compute

the average projected area as

$$\langle A_{\text{proj}} \rangle_{\Omega} = \frac{1}{\Omega} \int_0^{2\pi} \int_0^{\theta_{\text{max}}} A_{\text{proj}}(\theta', \varphi') \sin\theta' \, d\theta' \, d\varphi', \tag{6.3}$$

where $\theta_{\text{max}} = \arccos\left(1 - \frac{\Omega}{2\pi}\right)$ defines the angular extent of the accessible region.

6.3 Efficiency Factorization

The efficiency shown in Figure 5.7 represents the overall detection efficiency of monopoles with fixed mass and different velocities, averaged in all directions. However, the detection efficiency also depends on the direction of the monopole trajectory, through variations in track length and detector response. For further calculations, it is useful to separate this efficiency into two parts: one that depends on the monopole speed β, and another that depends on the direction of the incoming trajectory,

$$\epsilon(m, \beta, \varphi, \theta) = \epsilon(\beta) \, \epsilon(\varphi, \theta). \tag{6.4}$$

Here, we can neglect any explicit dependence on mass, since no significant variation is expected once the monopole reaches the detector.

6.4 Calculation of Flux Limit

The 90% CL upper limit on the flux, assuming zero background, is given by

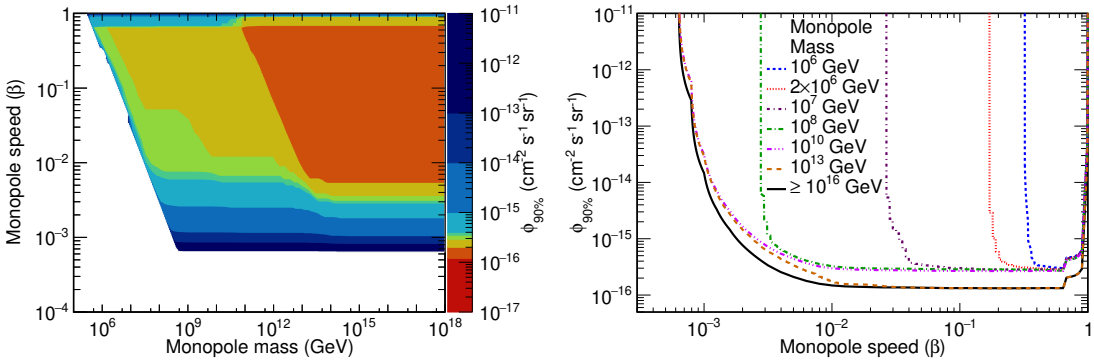
$$\phi_{90\%} = \langle \phi_{90\%} \rangle_{\Omega}(m, \beta) = \frac{\ln(10)}{\langle A_{proj}(\varphi, \theta) \epsilon(\varphi, \theta) \rangle_{\Omega} \epsilon(m, \beta) \Omega \, T} \tag{6.5}$$

where T denotes the total live time (see Section 4.3). The factor $\ln(10)$ represents the upper bound of the 90% CL for a Poisson process with zero observed events. We introduce the solid-angle-averaged acceptance as follows.

$$\langle A_{proj}(\Omega) \epsilon(\Omega) \rangle = \frac{1}{\Omega} \int_{\varphi'=0}^{2\pi} \int_{\theta'=0}^{\arccos\left(1-\frac{\Omega}{2\pi}\right)} A_{proj}(\varphi', \theta') \epsilon(\varphi', \theta') \sin\theta' d\theta' d\varphi' \tag{6.6}$$

$\log_{10}(\beta)$	Heavy	10^{13} GeV	10^{10} GeV	10^{7} GeV	10^{6} GeV
-3.1	3000	5800	6200	—	—
-3.0	150	300	320	—	—
-2.9	33	64	71	—	—
-2.8	15	28	32	—	—
-2.7	7.8	15	17	—	—
-2.6	5.0	9.0	11	—	—
-2.5	3.4	6.0	7.3	—	—
-2.4	2.6	4.4	5.4	—	—
-2.3	2.1	3.4	4.4	—	—
-2.2	1.8	2.7	3.7	—	—
-2.1	1.6	2.1	3.2	—	—
-2.0	1.5	1.7	3.0	—	—
-1.9	1.4	1.6	2.9	—	—
-1.8	1.4	1.6	2.9	—	—
-1.7	1.4	1.5	2.8	—	—
-1.6	1.4	1.4	2.8	—	—
-1.5	1.4	1.4	2.8	16	—
-1.4	1.4	1.4	2.8	3.7	—
-1.3	1.4	1.4	2.8	3.4	—
-1.2	1.4	1.4	2.7	3.2	—
-1.1	1.4	1.4	2.7	3.1	—
-1.0	1.4	1.4	2.7	3.0	—
-0.9	1.4	1.4	2.7	3.0	—
-0.8	1.3	1.3	2.7	2.9	—
-0.7	1.3	1.3	2.7	2.9	—
-0.6	1.3	1.3	2.7	2.9	—
-0.5	1.3	1.3	2.6	2.9	—
-0.4	1.3	1.3	2.7	2.9	3.5
-0.3	1.4	1.4	2.7	2.9	3.2
-0.2	1.3	1.3	2.7	2.9	3.0
-0.15	1.9	1.9	3.9	4.2	4.4
-0.1	2.0	2.0	4.0	4.3	4.4
-0.05	2.5	2.5	5.0	5.3	5.4
-0.01	27	27	52	57	57
-0.004	140	140	270	300	300
-0.0022	760	760	1500	1600	1600

Table 6.1: 90% CL upper limits on the magnetic monopole flux in units of $10^{-16}\text{cm}^{-2}\text{s}^{-1}\text{sr}^{-1}$. *Heavy* denotes monopoles with masses above 10^{16} GeV that are capable of traversing the entire Earth.



(a) (b)

Figure 6.4: Flux limit as a function of (a) monopole velocity and mass, and (b) monopole velocity β for fixed monopole masses. This figure provides a graphical representation of the data listed in Table 6.1.

We determine this upper limit at every point in the monopole mass and velocity parameter space, as shown in Figure 6.4a. Representative flux limits are listed in Table 6.1, and Figure 6.4b provides a visual summary of these limits. The quoted limits are conservative, as they are based on conservative assumptions for both the effective live time and the selection efficiency.

In particular, the estimates include a 10% decrease in the nominal dE/dx, as described in Section 3.2, to cover systematic uncertainties in the energy deposition. In addition, a 10% increase in the monopole energy loss in the Earth is assumed when calculating the minimum monopole mass capable of reaching the FD at a given velocity and incident angle. A further 1% reduction in the live time is applied to account for periods with incomplete trigger live time information.

In summary, we present upper limits on the monopole flux as a function of monopole mass over the velocity range $7 \times 10^{-4} < \beta < 0.995$. Within specific regions of the speed-mass parameter space, these limits are the most stringent constraints reported to date. For the highest velocities considered, the search is sensitive to monopoles with masses as low as 2×10^5 GeV. For very massive monopoles capable of reaching the detector from above

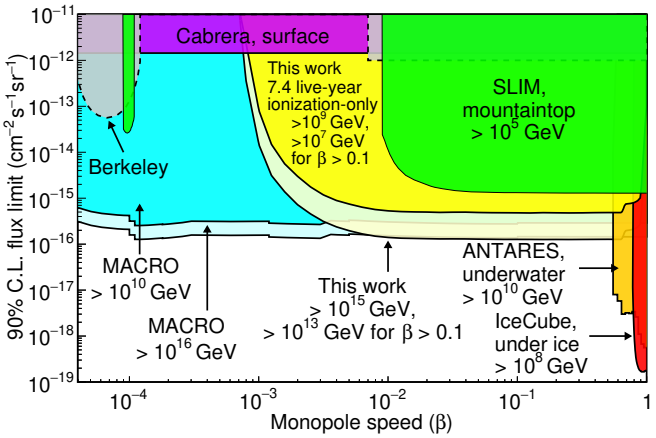


Figure 6.5: Upper limits on magnetic monopole flux for several experiments. In each region, the experiment with the strongest mass limit (least overburden) is shown above the others [7, 8, 9, 10, 11, 12]. Results from our search are shown in the regions labeled "This work." We report the most stringent limit, $\phi_{90\%} < 8 \times 10^{-16}\,\mathrm{cm^{-2}s^{-1}sr^{-1}}$, in the range $0.005 < \beta < 0.8$, corresponding to monopoles with masses greater than 10^9 GeV for all speeds, and greater than 10^7 GeV for $\beta > 0.1$. In the same range of β, for higher-mass monopoles capable of traversing the Earth, we set a flux limit $\phi_{90\%} < 2 \times 10^{-16}\,\mathrm{cm^{-2}s^{-1}sr^{-1}}$, corresponding to monopoles with masses greater than 10^{15} GeV and 10^{13} GeV for $\beta > 0.1$.

or traversing the Earth from below, we obtain a 90% CL upper limit on the flux of $\phi_{90\%} < 2 \times 10^{-16}\,\mathrm{cm^{-2}s^{-1}sr^{-1}}$ for monopoles with $0.005 < \beta < 0.8$. Over the same velocity interval, we set a 90% CL upper limit of $\phi_{90\%} < 8 \times 10^{-16}\,\mathrm{cm^{-2}s^{-1}sr^{-1}}$ for low-mass monopoles that can reach the detector through its minimal overburden.

The combination of NOvA's large fiducial volume and relatively small overburden provides enhanced sensitivity to slower and lower-mass monopoles that were not accessible in previous searches. This minimal-overburden region is illustrated in Fig. 6.5, where the result of this work is compared with the results of earlier experiments. The dependence on overburden is explicitly represented, with experiments characterized by a smaller overburden, and therefore by sensitivity to lower monopole masses appearing towards the top of the stack. The constraints reported here are complementary to our earlier results obtained using the transit-time-based trigger, which probe a lower range of monopole velocities [88].

The analysis is sensitive to sub-relativistic, highly ionizing particles, and the same dataset can be reinterpreted in the context of other hypothetical, strongly ionizing objects that would produce similar signatures, including quark nuggets [90, 91, 92] and microscopic black holes [93, 94, 95]. A detailed reinterpretation of these results within such alternative frameworks is left for future work.

Chapter 7

Neutrino Oscillation

Neutrinos are among the most fascinating and elusive particles in the Standard Model of particle physics. Neutrinos were first proposed by Wolfgang Pauli in 1930 to preserve energy and momentum conservation in beta decay [96], and were initially assumed to be massless particles traveling at the speed of light in vacuum. Although they are electrically neutral and interact only weakly with matter, they play a crucial role in our understanding of fundamental physics and the evolution of the Universe. One of the most remarkable discoveries in neutrino physics is the phenomenon of neutrino oscillation, which demonstrates that neutrinos can change from one flavor to another as they propagate. This observation provides clear evidence that neutrinos have non-zero mass and provides one of the first clear indications of physics beyond the Standard Model in neutrino sector.

This chapter provides an overview of the neutrino oscillations. We first discuss the theoretical framework of neutrinos in Section 7.1, then describe how they interact with matter, and explain their production and detection mechanisms in Section 7.2. The formalism of two- and three-flavor mixing in vacuum is developed in Section 7.4, followed by a discussion of matter effects in Section 7.5. We conclude in Section 7.7 by outlining the open questions that continue to shape current research in this area.

7.1 Neutrinos in Standard Model

The Standard Model of particle physics provides a successful framework for describing all known fundamental particles and three of the four fundamental forces: electromagnetism, the weak interaction, and the strong interaction. The matter constituents of the Standard

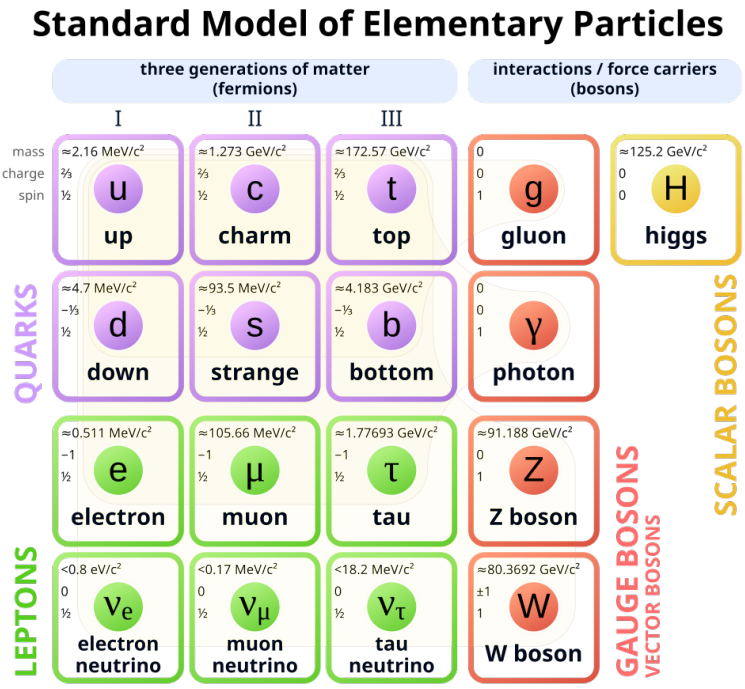


Figure 7.1: Overview of the particles of the Standard Model, grouped into fermions (quarks and leptons) and bosons (gauge bosons and the Higgs boson). Image adapted from the wikipedia [13].

Model are fermions, which are divided into two groups: quarks and leptons, as shown schematically in Fig. 7.1. Quarks combine to form protons, neutrons, and other hadrons, and they interact through the strong force mediated by gluons. Leptons include electron, muon, and tau, along with their corresponding neutrinos. The fundamental forces are mediated by bosons: the photon mediates electromagnetism, the W^+, W^-, and Z^0 bosons mediate the weak interaction, and eight gluons mediate the strong interaction. The Higgs boson completes the model by generating masses for the W and Z bosons as well as for the fermions via the Higgs mechanism.

Within the Standard Model, there are three flavors of neutrinos: the electron neutrino (ν_e), the muon neutrino (ν_μ), and the tau neutrino (ν_τ) [97, 98, 99]. Neutrinos interact only

through the weak force. They couple to $W^{\pm}$ and Z^0 bosons via Charge Current (CC) and Neutral Current (NC) interactions, respectively.

In CC interactions, a neutrino is converted into its corresponding charged lepton through the W-boson exchange (for example, $\nu_\mu + n \rightarrow \mu^- + p$). In contrast, NC interactions proceed via Z-boson exchange and preserve the neutrino flavor (for example, $\nu + N \rightarrow \nu + N$). It is crucial to emphasize that neutrinos are produced and detected as flavor eigen states, identified by the flavors of their associated charged leptons (e, μ, τ).

Because they are electrically neutral and interact only via the weak force, neutrinos can travel through ordinary matter with almost no scattering. As a result, neutrinos carry direct information from the innermost regions of stars, supernovae, the Sun, and other extreme cosmic sources. This makes them exceptional messengers for probing phenomena that cannot be accessed by other means. Detecting neutrinos yields crucial insights into the early universe, core-collapse supernovae, high-energy astrophysical processes, and the fundamental characteristics of elementary particles.

In the original formulation of the Standard Model, neutrinos were assumed to be exactly massless. However, measurements of neutrino oscillations in solar, atmospheric, reactor, and accelerator experiments [100, 101, 102, 103, 104] demonstrate that neutrinos possess nonzero masses, thereby providing clear evidence for physics beyond the Standard Model.

7.2 Neutrino Production and Detection

Neutrinos are produced in a wide variety of natural and man-made processes and are, after photons, the second most abundant particle in the universe.Among astrophysical sources, the Sun is the primary producer of neutrinos: nuclear fusion reactions, predominantly the proton-proton chain, produce an intense flux of ν_e, providing a direct probe of the dynamics of the solar interior.High-energy neutrinos are also created in the Earth's atmosphere when

cosmic rays collide with air nuclei, producing secondary mesons such as pions and kaons that decay into muon and electron neutrino.

The core-collapse of a massive star in supernovae is another key origin, where enormous numbers of neutrinos are produced.Intense artificial neutrino sources also exist, such as nuclear reactors, where beta decays of fission fragments emit large numbers of electron antineutrinos ($\bar{\nu}_e$), and particle accelerators, which generate collimated neutrino beams by directing high-energy protons onto fixed targets to create pions and kaons that subsequently decay, resulting in nearly pure flavor beams ideal for oscillation and interaction studies.

Neutrinos interact solely via the weak force, resulting in extremely small interaction cross sections. Therefore, even the very intense natural and man-made neutrino sources discussed above yield only a tiny number of detectable events, making experimental observation difficult. This requires the use of neutrino experiments with very large and highly active detectors. In experiments, neutrinos are detected indirectly by observing secondary charged particles (leptons or hadrons) produced when a neutrino scatters off a target nucleus or electron, and then measuring the properties of neutrinos from the resulting reaction products.

One of the most commonly used methods is Cherenkov detection using water or ice. When a charged particle generated in a neutrino interaction moves faster than the speed of light in that medium, it produces Cherenkov radiation at a well-defined angle. Experiments such as Super-Kamiokande, which uses a huge water tank lined with thousands of photomultiplier tubes to detect Cherenkov light and reconstruct its direction, energy, and flavor [105]. Ice-based detectors such as IceCube follow the same principle, installing photo detectors far below the Antarctic surface on the ice to detect high-energy astrophysical neutrinos [106]. Another important category of detectors uses the liquid scintillator as the interaction medium. In these setups, charged particles generated in neutrino interactions excite the scintillator molecules, which subsequently return to their ground state by emitting

scintillation light. Experiments such as KamLAND, Borexino, and NOvA use this method to obtain excellent energy resolution and very low energy thresholds [107, 108, 109].

Another highly effective detection technique is based on Liquid Argon Time Projection Chambers (LArTPCs). This method provides fine 3D images of the tracks of charged particles generated in neutrino interactions. In these detectors, ionization electrons drift in a uniform electric field and are captured on segmented readout planes, allowing for detailed reconstruction of the event topology and calorimetric measurements. Experiments such as ICARUS and the future DUNE detectors use LArTPCs to accurately measure the final states of the neutrino interaction and to investigate neutrino oscillations with high resolution event-by-event reconstruction [110, 111].

For very low-energy neutrinos, such as those coming from the Sun or supernovae, additional methods and dedicated detector materials are often used. Historically, radiochemical experiments used large quantities of chlorine or gallium-based substances, in which neutrino interactions generate radioactive isotopes that can be isolated and counted, to determine neutrino flux [112, 113]. Coherent elastic neutrino–nucleus scattering (CEvNS), theoretically predicted decades ago but only confirmed experimentally in recent years, is now being investigated with cryogenic detectors and low-threshold scintillators, where the tiny nuclear recoil signals must be detected with extremely low background and very high sensitivity [114].

7.3 Evidence of Neutrino Flavor Oscillations

Neutrino oscillation is a quantum mechanical phenomenon in which neutrinos convert from one flavor state to another as they propagate [115, 116]. An early indication that neutrinos can change from one flavor to another came from measurements of the solar neutrino flux. In the late 1960s, the Homestake experiment, led by Raymond Davis Jr. and John Bahcall,

consistently measured only about one third of the theoretically predicted flux of solar electron neutrinos. This discrepancy in the observed neutrino flux, known as the solar neutrino problem, provided one of the earliest and strongest hints of new physics in the neutrino sector [117, 118].

In addition to the solar neutrino problem, more evidence came from atmospheric neutrinos produced by cosmic rays interacting with Earth's atmosphere. The Super-Kamiokande experiment revealed that neutrinos traveling different path lengths appeared to vanish at different rates. This dependence of the disappearance rate on travel distance provides strong evidence for neutrino flavor oscillations [100, 119].

A significant development in neutrino oscillation study was achieved when the Sudbury Neutrino Observatory (SNO), using heavy water (D_2O), was able to measure both the flux of electron neutrinos and the total flux of all active neutrino flavors, thus solving the long-standing solar neutrino problem [102]. SNO reported that a significant fraction of solar electron neutrinos convert into muon and tau neutrinos on their way to Earth. When combined with atmospheric neutrino data from Super-Kamiokande [100], these results offered compelling evidence for neutrino oscillations and thus for nonzero neutrino masses.

Subsequent reactor- and accelerator-based experiments, including KamLAND [103], Daya Bay [120], the Reactor Experiment for Neutrino Oscillation (RENO) [121], Double Chooz [122], KEK to Kamioka (K2K) [123], the Main Injector Neutrino Oscillation Search (MINOS) [124], Tokai to Kamioka (T2K) [125], and NOvA [109], have further refined these measurements with high precision, thus providing a reliable framework for the three-flavor neutrino oscillation. Next generation long-baseline experiments such as Deep Underground Neutrino Experiment (DUNE) [126] and Hyper-Kamiokande [127] are designed to study even more fundamental aspects.

7.4 Neutrino Oscillation in Vacuum

The fundamental reason for neutrino oscillations is that the flavor eigenstates (ν_α), which participate in weak interactions, are different from the mass eigenstates (ν_i). Instead, each flavor eigenstate is a linear superposition of mass eigenstates with distinct masses. As these mass components propagate, their phases evolve at different rates, leading to relative phase shifts that are observed experimentally as neutrino oscillations [115, 128].

The relation between the flavor and the mass eigenstate bases is defined by a unitary mixing matrix. In a framework with N flavors, this mixing is represented by a $N \times N$ unitary matrix U, which can be parametrized in terms of $N(N-1)/2$ mixing angles and $(N-1)(N-2)/2$ CP-violating phases.The general relations between flavor and mass eigenstates can be expressed as

$$|\nu_\alpha\rangle = \sum_{i=1}^{N} U_{\alpha i}\, |\nu_i\rangle\,, \qquad |\nu_i\rangle = \sum_{\alpha=1}^{N} U^*_{\alpha i}\, |\nu_\alpha\rangle\,. \tag{7.1}$$

where the index α denotes flavor eigenstates, while i labels the corresponding mass eigenstates.

The evolution of a mass eigenstate $|\nu_i\rangle$ is governed by the Schrödinger equation, leading to a phase factor $e^{-iE_i t}$ as it propagates in time. For ultra-relativistic neutrinos, working in natural units $\hbar = c = 1$ and using $t \simeq L$ (since $v \simeq c$), the energy can be approximated as $E_i \simeq E + m_i^2/(2E)$. Thus, after propagating over a distance L, the phase factor becomes

$$e^{-iE_i t} \simeq e^{-iE_i L} = e^{-iEL}\, e^{-i\frac{m_i^2 L}{2E}}. \tag{7.2}$$

Thus, the time development of a flavor eigenstate can be written as

$$|\nu_\alpha(t)\rangle = \sum_{i=1}^{N} U_{\alpha i}\, e^{-iEL}\, e^{-i\frac{m_i^2 L}{2E}}\, |\nu_i\rangle, \tag{7.3}$$

where $U_{\alpha i}$ denote the elements of the leptonic mixing matrix [129, 130]. As a result, a neutrino produced initially in the flavor state $|\nu_\alpha\rangle$ will change as it propagates, and at a

later time t the probability of observing it in the flavor state ν_β is determined by the overlap between the time-evolved state and the final flavor state $|\nu_\beta\rangle$ [131]:

$$P_{\nu_\alpha \to \nu_\beta} = |\langle \nu_\beta \,|\, \nu_\alpha(t)\rangle|^2 . \tag{7.4}$$

The global phase factor e^{-iEL} is identical for all mass eigenstates and thus cancels out of the transition probabilities, and only the relative phases remain physically meaningful, as will become clear in the two- and three-flavor formalisms discussed below.

7.4.1 Two Flavor Formalism

In the most basic treatment of neutrino oscillations, it is sufficient to consider only two neutrino flavors. Within this framework, the flavor eigenstates $|\nu_\alpha\rangle$ and $|\nu_\beta\rangle$ can be expressed as linear combinations of two mass eigenstates, $|\nu_1\rangle$ and $|\nu_2\rangle$. Their mixing is characterized by a single real mixing angle θ, such that the transformation from the mass basis to the flavor basis is given by

$$\begin{pmatrix} \nu_\alpha \\ \nu_\beta \end{pmatrix} = \begin{pmatrix} \cos\theta & \sin\theta \\ -\sin\theta & \cos\theta \end{pmatrix} \begin{pmatrix} \nu_1 \\ \nu_2 \end{pmatrix} . \tag{7.5}$$

This unitary 2×2 matrix clearly shows that every flavor state is a quantum superposition of the mass eigenstates, with coefficients determined by the mixing angle.

The time evolution of an initially produced state $|\nu_\alpha\rangle$ is described by

$$|\nu_\alpha(t)\rangle = \cos\theta\, e^{-i\frac{m_1^2 L}{2E}} |\nu_1\rangle + \sin\theta\, e^{-i\frac{m_2^2 L}{2E}} |\nu_2\rangle. \tag{7.6}$$

To find the probability that the neutrino is detected in the flavor state β, we project the time-evolved state onto

$$|\nu_\beta\rangle = -\sin\theta\,|\nu_1\rangle + \cos\theta\,|\nu_2\rangle. \tag{7.7}$$

The transition probability for a neutrino to oscillate from flavor α to flavor β as

$$P_{\nu_\alpha \to \nu_\beta} = \sin^2(2\theta)\, \sin^2\left(\frac{\Delta m^2 L}{4E}\right), \tag{7.8}$$

where $\Delta m^2 = m_2^2 - m_1^2$. The corresponding survival probability for the initial flavor state is

$$P_{\nu_\alpha \to \nu_\alpha} = 1 - \sin^2(2\theta)\, \sin^2\left(\frac{\Delta m^2 L}{4E}\right). \tag{7.9}$$

These expressions highlight several key features. The mixing angle θ determines the oscillation amplitude: when $\theta = 0$ there is no mixing, whereas $\theta = \pi/4$ yields the maximal mixing. The mass squared difference Δm^2 governs the oscillation frequency, with larger Δm^2 leading to faster oscillations. For application in experiments, the oscillatory term is commonly rewritten as

$$\sin^2\left(\frac{\Delta m^2 L}{4E}\right) = \sin^2\left[1.27\, \frac{\Delta m^2(\mathrm{eV}^2)\, L(\mathrm{km})}{E(\mathrm{GeV})}\right], \tag{7.10}$$

which shows that it depends on quantities that can be measured directly.

The two-flavor approximation thus provides a simple yet powerful way to describe neutrino oscillations. However, to fully describe the neutrino oscillation effects measured in solar, atmospheric, reactor, and accelerator experiments, the two-flavor approximation is insufficient. In these cases, a full three-flavor treatment is required, incorporating three mixing angles, up to three CP-violating phases, and two independent mass-squared differences to capture the observed oscillation phenomena, which is discussed next.

7.4.2 Three Flavor Formalism

In realistic situations, oscillations involve all three neutrino flavors, so a complete description must use the full three-flavor framework. Within this formalism, the flavor eigenstates $|\nu_\alpha\rangle$ (with $\alpha = e, \mu, \tau$) are related to the mass eigenstates $|\nu_i\rangle$ (with $i = 1, 2, 3$) by a unitary mixing matrix U:

$$|\nu_\alpha\rangle = \sum_{i=1}^{3} U_{\alpha i} |\nu_i\rangle. \tag{7.11}$$

The matrix U is the Pontecorvo–Maki–Nakagawa–Sakata (PMNS) matrix, which is

conventionally written as

$$U \;=\; R_{23}\, S_{13}\, R_{12}, \tag{7.12}$$

where R_{ij} denotes a real rotation by an angle θ_{ij} in the ij-plane, and S_{ij} is the corresponding complex rotation that incorporates CP violation. In this parameterization, the PMNS matrix is fully specified by the three mixing angles θ_{12}, θ_{23}, θ_{13} and the CP-violating phase δ_{CP} as

$$U \;=\; \underbrace{\begin{pmatrix} 1 & 0 & 0 \\ 0 & c_{23} & s_{23} \\ 0 & -s_{23} & c_{23} \end{pmatrix}}_{R_{23}} \underbrace{\begin{pmatrix} c_{13} & 0 & s_{13}e^{-i\delta_{\text{CP}}} \\ 0 & 1 & 0 \\ -s_{13}e^{i\delta_{\text{CP}}} & 0 & c_{13} \end{pmatrix}}_{S_{13}} \underbrace{\begin{pmatrix} c_{12} & s_{12} & 0 \\ -s_{12} & c_{12} & 0 \\ 0 & 0 & 1 \end{pmatrix}}_{R_{12}}. \tag{7.13}$$

Multiplying these rotation matrices leads to the usual three-flavor PMNS matrix:

$$U = \begin{pmatrix} c_{12}c_{13} & s_{12}c_{13} & s_{13}e^{-i\delta_{\text{CP}}} \\ -s_{12}c_{23} - c_{12}s_{23}s_{13}e^{i\delta_{\text{CP}}} & c_{12}c_{23} - s_{12}s_{23}s_{13}e^{i\delta_{\text{CP}}} & s_{23}c_{13} \\ s_{12}s_{23} - c_{12}c_{23}s_{13}e^{i\delta_{\text{CP}}} & -c_{12}s_{23} - s_{12}c_{23}s_{13}e^{i\delta_{\text{CP}}} & c_{23}c_{13} \end{pmatrix}, \tag{7.14}$$

with $c_{ij} = \cos\theta_{ij}$ and $s_{ij} = \sin\theta_{ij}$.

In vacuum, the time evolution of a neutrino state is described by

$$|\nu(t)\rangle = \sum_{i=1}^{3} U_{\alpha i}\, e^{-iE_i t}\, |\nu_i\rangle. \tag{7.15}$$

Using Equations 7.2 and 7.4, the probability that a neutrino created as ν_α is later observed as ν_β is given by

$$\begin{aligned} P_{\alpha\beta} = \delta_{\alpha\beta} &- 4\sum_{i>j} \Re\big(U^*_{\alpha i}U_{\beta i}U_{\alpha j}U^*_{\beta j}\big)\sin^2\!\left(\frac{\Delta m^2_{ji}L}{4E}\right) \\ &+ 2\sum_{i>j} \Im\big(U^*_{\alpha i}U_{\beta i}U_{\alpha j}U^*_{\beta j}\big)\sin\!\left(\frac{\Delta m^2_{ji}L}{2E}\right). \end{aligned} \tag{7.16}$$

where $\Delta m^2_{ji} \equiv m^2_j - m^2_i$. The survival probability, which is the probability that a neutrino is observed with the same flavor as at production is given by

$$P_{\nu_\alpha\to\nu_\alpha} = 1 \;-\; 4\sum_{j>i} |U_{\alpha i}U_{\alpha j}|^2 \sin^2\!\left(\frac{\Delta m^2_{ji}L}{4E}\right). \tag{7.17}$$

For antineutrinos, the associated flavor states are expressed as

$$|\bar{\nu}_\alpha\rangle = \sum_{i=1}^{3} U_{\alpha i}\,|\bar{\nu}_i\rangle,$$

which leads to a corresponding oscillation probability,

$$\begin{aligned} P_{\bar{\nu}_\alpha\to\bar{\nu}_\beta} = \delta_{\alpha\beta} &- 4\sum_{j>i} \Re\big(U_{\alpha i}U^*_{\beta i}U^*_{\alpha j}U_{\beta j}\big)\sin^2\left(\frac{\Delta m^2_{ji}L}{4E}\right) \\ &+ 2\sum_{j>i} \Im\big(U_{\alpha i}U^*_{\beta i}U^*_{\alpha j}U_{\beta j}\big)\sin\left(\frac{\Delta m^2_{ji}L}{2E}\right). \end{aligned} \tag{7.18}$$

These three-flavor neutrino oscillation frameworks highlight several key features. The CP-violating phase δ_{CP} appears through the imaginary components of certain products of PMNS matrix elements, giving rise to a difference between neutrino and antineutrino oscillation probabilities expressed as

$$\Delta P_{\alpha\beta} = P_{\nu_\alpha\to\nu_\beta} - P_{\bar{\nu}_\alpha\to\bar{\nu}_\beta} = 4\sum_{j>i} \Im\big(U^*_{\alpha i}U_{\beta i}U_{\alpha j}U^*_{\beta j}\big)\sin\left(\frac{\Delta m^2_{ij}L}{2E}\right). \tag{7.19}$$

In contrast, survival probabilities (where $\alpha = \beta$) depend exclusively on the real parts of these PMNS combinations and therefore are insensitive to CP violation.

The discussion so far has focused on neutrino oscillations in vacuum, where flavor transitions are determined by mixing angles, mass-squared differences, and the propagation distance. In many realistic situations, however, neutrinos travel through media such as the Sun, Earth, or dense astrophysical environments instead of empty space. Their interactions with the surrounding matter through coherent forward scattering, particularly with electrons, modify the effective oscillation parameters and can significantly change the transition probabilities. This effect is essential for understanding solar, atmospheric, and long-baseline neutrino experiments. Next, we discuss the neutrino oscillations in matter and the corresponding resonance conditions.

7.5 Neutrino Oscillation in Matter

When neutrinos propagate through a medium, their evolution is influenced by coherent forward scattering with the particles present in that environment. This effect becomes especially important in dense regions such as the Sun, the Earth, and the interior of core-collapse supernovae, where matter can strongly modify the oscillation behavior. The effective Hamiltonian in the presence of matter was first derived by Wolfenstein and later extended by Mikheyev and Smirnov, resulting in what is now known as the Mikheyev–Smirnov-Wolfenstein (MSW) effect [132, 133]. In matter, the extra potential term in the Hamiltonian modify the effective mass-squared splittings and mixing angles. As a result, neutrino flavor conversion can experience resonant amplification, producing pronounced matter induced oscillation phenomena that play a crucial role in understanding solar neutrino observations, atmospheric neutrinos crossing the Earth, and long-baseline accelerator experiments.

We now derive the effective Hamiltonian that describes neutrino propagation in a medium. Neutrinos interact with matter via weak interaction, and since these interactions are defined in the flavor basis, we must formulate the propagation Hamiltonian in the flavor basis as well. In this basis, the total Hamiltonian is split into two parts: a vacuum term, obtained by transforming the Hamiltonian from the mass basis to the flavor basis via the mixing matrix U, and an additional interaction term arising from coherent forward scattering on electrons, protons, and neutrons in matter. The effective Hamiltonian that governs neutrino propagation in matter can therefore be expressed as

$$H = U H_0 U^\dagger + H_{\text{matter}}, \tag{7.20}$$

where H_{matter} represents the effective potential of CC interactions and NC interactions. Because NC interactions are identical for all active flavors, they do not affect neutrino oscilla-

tions. The only standard interaction that alters oscillation behavior is the coherent forward scattering of ν_e through CC interactions with electrons present in the medium [133, 132, 134]. This yields an effective potential that alters the Hamiltonian in the flavor basis. The corresponding matter contribution is

$$H_{\text{matter}} = \pm V \begin{pmatrix} 1 & 0 & 0 \\ 0 & 0 & 0 \\ 0 & 0 & 0 \end{pmatrix}. \tag{7.21}$$

Here

$$V = \pm\sqrt{2}\, G_F N_e, \tag{7.22}$$

where G_F is the Fermi constant and N_e denotes the electron number density. The $+$ sign corresponds to neutrinos, while the $-$ sign corresponds to antineutrinos. Using Equations 7.20 and 7.21, the Hamiltonian in the flavor basis can be written as

$$H = \frac{1}{2E}\, U\, \text{diag}(m_1^2, m_2^2, m_3^2)\, U^\dagger + V\, \text{diag}(1,0,0). \tag{7.23}$$

The oscillation probability in matter can be written using the following quantities:

$$\Delta \equiv \frac{\Delta m^2_{31} L}{4E}, \qquad \alpha \equiv \frac{\Delta m^2_{21}}{\Delta m^2_{31}}, \qquad A \equiv \frac{2EV}{\Delta m^2_{31}}. \tag{7.24}$$

Under these definitions, the $\nu_\mu \to \nu_e$ appearance probability in matter for long-baseline experiments can be approximated by

$$\begin{aligned} P_{\nu_\mu \to \nu_e} \simeq\; & 4\, s^2_{13}\, s^2_{23}\, \frac{\sin^2\big[(1-A)\Delta\big]}{(1-A)^2} \\ & + 8\, c_{12} s_{12}\, c_{23} s_{23}\, s_{13}\, \alpha\, \cos(\Delta + \delta_{\text{CP}})\, \frac{\sin(A\Delta)\, \sin\big[\Delta(1-A)\big]}{A(1-A)}. \end{aligned} \tag{7.25}$$

Figure 7.2 displays the $\nu_\mu \to \nu_e$ appearance probability in NOvA for the two possible neutrino mass orderings: the Normal Hierarchy (NH) and the Inverted Hierarchy (IH). The solid curves represent the prediction in vacuum, while the dashed and dotted curves show how matter effects modify the oscillation probability for ν and $\bar{\nu}$ in each hierarchy. In the

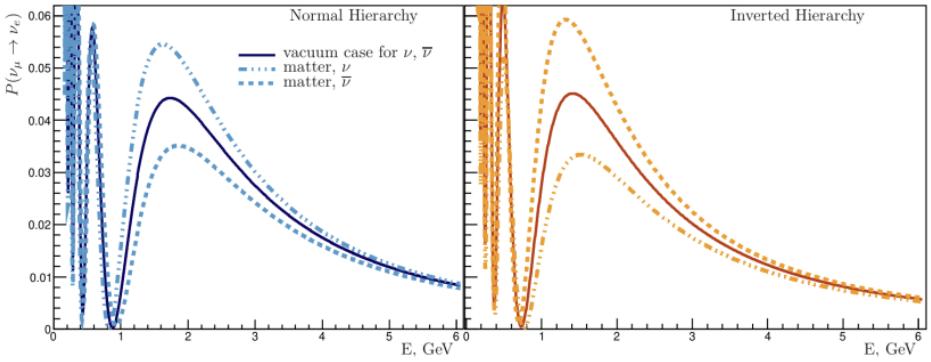


Figure 7.2: The impact of matter on the $\nu_\mu \to \nu_e$ oscillation probability for both neutrinos and antineutrinos in NOvA, illustrated for normal and inverted mass orderings, assuming $\delta_{CP} = 0$. Figure adapted from Ref. [14].

NH scenario, the third mass eigenstate is the heaviest ($m_3 > m_1, m_2$), corresponding to a positive atmospheric mass-squared splitting ($\Delta m^2_{31} > 0$). Under these circumstances, matter effects enhance the neutrino appearance probability, giving rise to the larger amplitude curves in the left panel. In contrast, in the IH case, the third mass eigenstate is the lightest ($m_3 < m_1, m_2$), implying $\Delta m^2_{31} < 0$. This change in sign reverses the effective matter potential, boosting the antineutrino appearance probability instead, as shown in the right panel.

The distinct behaviors of neutrinos and antineutrinos in the NH and IH scenarios allow present and future experiments to take advantage of these differences in order to determine the mass ordering. In the following section, we review the measurements that constrain each oscillation parameter, highlighting the complementary contributions of solar, atmospheric, reactor, and accelerator observations.

7.6 Measurement of Oscillation Parameters

Neutrino oscillation parameters have been probed by several experiments using a wide range of natural and artificial neutrino sources, each offering complementary sensitivity

to different features of three-flavor mixing. Observations from SNO [102, 135], Super-Kamiokande [136], and Borexino [137] have been crucial to accurately determine the mixing angle θ_{12} and the mass-squared splitting Δm^2_{21}. When these are combined with long-baseline reactor measurements from KamLAND [138], the sign of Δm^2_{21} is fixed through the MSW matter effect, and the resulting constraints on the solar neutrino oscillation parameters are constrained.

Reactor neutrinos offer another essential way for probing oscillation parameters. Short-baseline reactor experiments, such as Daya Bay [120], RENO [121], and Double Chooz [122], have observed the disappearance of $\bar{\nu}_e$ over baselines of roughly 1–2 km, resulting in the most precise measurement to date of the mixing angle θ_{13}. Longer-baseline experiments, including KamLAND and the JUNO [139], are sensitive to the oscillation pattern driven by Δm^2_{21} and aim to determine both Δm^2_{21} and θ_{12} with high precision. In addition, because of its high energy resolution, JUNO will deliver a precise measurement of the neutrino mass hierarchy.

Atmospheric neutrinos are produced in the upper atmosphere, with a spectrum that ranges from a few hundred MeV to several tens of TeV, and propagate over distances comparable to the Earth's diameter. Experiments such as Super-Kamiokande [140], IceCube [141] and KM3NeT/ORCA [142] take advantage of this wide energy range and baseline to determine θ_{23} and $|\Delta m^2_{32}|$ with high precision. As neutrinos travel through the Earth, the combined influence of vacuum oscillations and matter effects makes atmospheric measurements particularly sensitive to the neutrino mass ordering. Although the exact value of θ_{23} and its octant are still not completely determined, the combined results from atmospheric and accelerator experiments now restrict these parameters to the level of a few percent.

Long-baseline accelerator experiments, in turn, produce precisely controlled neutrino beams and enable investigations of both ν_μ disappearance and ν_e appearance channels. Experiments T2K [143] and NOvA [144] currently yield some of the most stringent limits on

atmospheric oscillation parameters, specifically θ_{23}, $|\Delta m^2_{32}|$ and δ_{CP}. Forthcoming experiments such as DUNE [145] are expected to greatly enhance the sensitivity to δ_{CP}, determine the octant θ_{23}, and establish mass ordering with strong statistical significance.

Oscillation Parameter	Best-Fit Value
$\sin^2\theta_{12}$	$0.308^{+0.012}_{-0.011}$
Δm^2_{21}	$(7.49^{+0.19}_{-0.19}) \times 10^{-5}$ eV^2
$\sin^2\theta_{13}$	$0.02215^{+0.00056}_{-0.00058}$
$\sin^2\theta_{23}$	$0.470^{+0.017}_{-0.013}$
Δm^2_{31}	$(2.513^{+0.021}_{-0.019}) \times 10^{-3}$ eV^2
δ_{CP} ($^\circ$)	212^{+26}_{-41}

Table 7.1: Best-fit values of neutrino oscillation parameters from NuFIT 6.0 assuming normal mass ordering [15].

Table 7.1 summarizes the current best-fit values of the neutrino oscillation parameters of NuFIT 6.0, assuming normal mass ordering. Measurements from solar, atmospheric, reactor, and accelerator measurements have confirmed the three-flavor neutrino oscillation paradigm with remarkable accuracy. However, several key parameters remain only loosely constrained, and resolving these outstanding issues is a central goal of existing and next-generation neutrino oscillation experiments. In the next section, we highlight the main open questions and discuss their consequences for particle physics and cosmology.

7.7 Open Questions in the Neutrino Oscillation Sector

Although the three-flavor framework of neutrino oscillations is now well established, several key properties of neutrinos remain unknown. A key open question is the neutrino mass ordering. Determining it is crucial for interpreting neutrinoless double-beta decay searches [146], precisely measuring CP violation, and establishing the absolute mass scale of neutrinos. Oscillation measurements have clearly shown the presence of two distinct mass-squared differences, but the sign of Δm^2_{31} has not yet been determined, leaving room

for two possible hierarchies, NH and IH.

The octant of the atmospheric mixing angle θ_{23} remains undetermined: it is still unclear whether its true value lies in the lower octant ($\theta_{23} < 45°$) or in the upper octant ($\theta_{23} > 45°$), even though current data favor nearly maximal mixing [147, 144]. This angle governs the mixing between muon neutrinos and tau neutrinos. A maximum value of $\theta_{23} = 45°$ corresponds to a symmetry $\mu - \tau$ in the lepton sector, while any deviation from maximal mixing signals the breaking of this symmetry. Therefore, resolving this ambiguity is important as it can shed light on the flavor that governs the observed pattern of neutrino mixing.

The exact value of the CP-violating phase δ_{CP} in neutrino oscillations is still unknown. Current experiments have not yet provided strong enough evidence to confirm CP violation in the lepton sector, so more sensitive future measurements are needed to determine δ_{CP} accurately.

Long-baseline accelerator experiments, which probe both appearance and disappearance channels, are best suited to address these outstanding issues. Ongoing efforts such as NOvA, T2K, JUNO, and IceCube, together with upcoming projects such as DUNE and Hyper-Kamiokande, are expected to clarify them with high statistical significance in the near future.

In addition to these main unknowns, several other important issues remain open. These include the exact degree of unitarity of the PMNS matrix, the possibility of sterile neutrinos, the presence of non-standard neutrino interaction, and the value of the absolute neutrino mass scale. Even though we cannot directly measure all of these quantities with oscillation experiments, if new physics exists, it may reveal itself as discrepancies between measurements made at different energies and across different baselines. The broad experimental program using reactor, solar, atmospheric, and accelerator neutrinos therefore provides a complementary path to investigate such new physics. The following chapter focuses on scalar non-standard neutrino interactions, which can additionally modify neutrino propaga-

tion, and we present a dedicated phenomenological study of these effects there.

Chapter 8

Probing Scalar Non-Standard Interactions at the P2SO Experiment

Neutrino non-standard interactions (NSI), which arise as subleading contributions, can alter the oscillation pattern by introducing additional neutrino–matter couplings beyond those predicted by the Standard Model. Studies show that these interactions also impact the precise determination of oscillation parameters [148], which is a central objective of both current and next-generation neutrino experiments. Therefore, it is essential to constrain the allowed regions of NSI parameters and examine how such interactions impact the measurement of standard neutrino oscillation parameters.

In this chapter, we concentrate on scalar NSI in the context of upcoming experiments such as Protvino to Super-ORCA (P2SO) and DUNE, where neutrinos couple to a scalar field that can substantially modify their oscillation behavior [149]. The chapter is organized as follows. Section 8.1 presents the theoretical framework of NSI, covering both the vector and scalar scenarios. Section 8.2 outlines the simulation details for P2SO and DUNE, together with the corresponding experimental setup. The impact of scalar NSI on oscillation probabilities is investigated in Section 8.3. Finally, Sections 8.4 and 8.5 examine the experimental sensitivity to scalar NSI and discuss their consequences for the determination of oscillation parameters, respectively.

8.1 Introduction to Non-Standard Interaction

The current and next-generation neutrino experiments are primarily aimed at achieving unprecedented precision in the measurement of neutrino mixing parameters. However, as

outlined in the previous chapter, several fundamental questions remain unresolved, including neutrino mass ordering, the octant of θ_{23}, and the precise value of δ_{CP}. In addition, the tensions among global-fit results, along with the broader search for physics beyond the Standard Model, provide strong motivation to investigate frameworks that extend or modify the standard three-flavor oscillation scenario.

One of the most fascinating possibilities involves NSI, the couplings between neutrinos and matter fields that emerge naturally in many BSM frameworks [148, 150]. NSI can alter neutrino propagation in matter and introduce degeneracies that complicate the interpretation of oscillation experiments.

NSI are commonly categorized into vector and scalar types: vector NSI modify the effective matter potential experienced by neutrinos, whereas scalar NSI generate mass-like contributions through couplings to scalar fields, thereby affecting the neutrino mass matrix and its evolution in matter. Both types of effects are discussed below.

8.1.1 Vector NSI Formalism

Vector NSI arise from effective four-fermion operators that modify the coherent forward scattering of neutrinos with matter fermions as they propagate. These interactions alter the effective matter potential on the flavor basis, extending the standard MSW contribution to a matrix structure that includes both diagonal and off-diagonal terms. The strength of these additional interactions with matter fermions (electrons, up and down quarks) is parameterized by dimensionless coefficients $\varepsilon_{\alpha\beta}$, defined relative to the Fermi constant G_F. As a result, NSI add an extra contribution to the Hamiltonian that governs neutrino propagation, which can alter oscillation probabilities and strongly affect how standard oscillation parameters are extracted from experimental data. In a model-independent framework, the

effective Lagrangian describing vector NSI can be written as [148]

$$\mathcal{L}_{\text{NSI}}^{\text{NC}} = -2\sqrt{2}\, G_F \sum_{f,\, P,\, \alpha,\, \beta} \varepsilon_{\alpha\beta}^{f,P} \left(\bar{\nu}_\alpha \gamma^\mu P_L \nu_\beta\right) \left(\bar{f}\, \gamma_\mu P\, f\right), \tag{8.1}$$

where $f \in \{e, u, d\}$ denote the background fermions, $\alpha, \beta \in \{e, \mu, \tau\}$ label the neutrino flavors, $P = P_L, P_R$ are the chirality projection operators and $\varepsilon_{\alpha\beta}^{f,P}$ quantify the strength of the new interactions.

To connect this Lagrangian to the effective Hamiltonian relevant for neutrino oscillations, one considers the forward coherent scattering of neutrinos in a background medium. In this limit, the interaction does not change the neutrino momentum but induces a phase shift, which can be interpreted as an effective potential. The relevant contribution arises from the expectation value of the fermion current,

$$\langle \bar{f}\, \gamma^\mu P\, f \rangle, \tag{8.2}$$

which, for an unpolarized and non-relativistic medium, simplifies to

$$\langle \bar{f}\, \gamma^\mu P\, f \rangle \simeq \delta^{\mu 0}\, N_f, \tag{8.3}$$

where N_f denotes the fermion number density [133, 148].

Substituting this result into Eq. 8.1, the interaction effectively reduces to a flavor-dependent potential term acting on the neutrino states,

$$\mathcal{L}_{\text{NSI}}^{\text{NC}} = -2\sqrt{2}\, G_F \sum_{f,\alpha,\beta} \varepsilon_{\alpha\beta}^{f}\, N_f\, \bar{\nu}_\alpha \gamma^0 P_L \nu_\beta. \tag{8.4}$$

This term directly contributes to the effective Hamiltonian, yielding

$$H_{\text{VNSI}} = \sqrt{2}\, G_F \sum_{f} N_f\, \varepsilon_{\alpha\beta}^{f}. \tag{8.5}$$

Thus, vector NSI introduces an additional flavor-dependent matter potential through the vector current interaction with the background medium. The full Hamiltonian governing neutrino propagation in the presence of vector NSI can therefore be written as

$$H_{\text{eff}} = \frac{1}{2E}\left[U_{\text{PMNS}}\begin{pmatrix}0 & 0 & 0\\ 0 & \Delta m^2_{21} & 0\\ 0 & 0 & \Delta m^2_{31}\end{pmatrix}U^{\dagger}_{\text{PMNS}} + \sqrt{2}\,G_F\,N_e\begin{pmatrix}1+\varepsilon_{ee} & \varepsilon_{e\mu} & \varepsilon_{e\tau}\\ \varepsilon^*_{e\mu} & \varepsilon_{\mu\mu} & \varepsilon_{\mu\tau}\\ \varepsilon^*_{e\tau} & \varepsilon^*_{\mu\tau} & \varepsilon_{\tau\tau}\end{pmatrix}\right]. \tag{8.6}$$

The unit entry in the ee component represents the standard MSW contribution, associated with the CC potential felt by electron neutrinos as specified in Equation 7.21. Every other term corresponds to the strength of the vector NSI, described by $\varepsilon_{\alpha\beta}$. The diagonal terms break lepton flavor universality, while the off-diagonal ones are flavor-changing. The former are real, the latter are complex, can interfere with the standard CP-violating phase, and may be parameterized as

$$\varepsilon_{\alpha\beta} = |\varepsilon_{\alpha\beta}|\, e^{i\phi_{\alpha\beta}}\,. \tag{8.7}$$

Because H_{VNSI} appears in the Schrödinger-like evolution equation for neutrinos, even small $\varepsilon_{\alpha\beta}$ can significantly modify oscillation probabilities over long baselines or in dense media, generating degeneracies between standard and non-standard effects such as the CP phase or mass ordering. Hence, NSI can affect the determination of the mixing parameters, complicating precision oscillation measurements and motivating dedicated searches in current and future neutrino experiments.

In the remainder of this chapter, we first introduce the scalar NSI framework and present a detailed phenomenological study of scalar NSI in the context of next-generation experiments such as P2SO [151].

8.1.2 Scalar NSI Formalism

New physics may also appear through scalar interactions, where neutrinos interact with matter fermions by exchanging a scalar mediator [149, 152]. In this case, the low-energy effec-

tive Lagrangian contains a Yukawa-type interaction between neutrinos and matter fermions.

$$\mathcal{L}_s^{\text{eff}} \propto y_f \, Y_{\alpha\beta} \left[\bar{\nu}_\alpha(p_3) \, \nu_\beta(p_2)\right] \left[\bar{f}(p_1) \, f(p_4)\right], \tag{8.8}$$

Here, y_f represents the Yukawa coupling between the scalar mediator ϕ and a matter fermion f, while $Y_{\alpha\beta}$ specifies the flavor structure associated with the neutrino–scalar coupling. Unlike vector-current operators, the scalar bilinear $\bar{\nu}_\alpha \nu_\beta$ cannot be rearranged via a Fierz transformation into a vector current that would yield the standard matter potential. As a result, scalar NSI do not modify the matter potential term in the effective Hamiltonian. Instead, they generate direct corrections to the neutrino mass matrix, which in turn modify mixing parameters that control oscillation phenomena.

In the non-relativistic limit for background fermions, the scalar bilinear reduces to the fermion number density as

$$\bar{u}_f u_f = \bar{u}_f \gamma^0 u_f = 2 \, \xi^\dagger \xi \simeq N_f, \tag{8.9}$$

so that the Dirac equation becomes

$$\bar{\nu}_\beta \left[i\partial_\mu \gamma^\mu + \left(M_{\beta\alpha} + \sum_f \frac{N_f \, y_f \, Y_{\alpha\beta}}{m_\phi^2} \right) \right] \nu_\alpha = 0, \tag{8.10}$$

where $M_{\beta\alpha}$ is the Dirac mass matrix of neutrinos. We therefore identify a matter-dependent correction to the mass matrix,

$$\delta M \equiv \sum_f \frac{N_f \, y_f \, Y}{m_\phi^2}. \tag{8.11}$$

Now, the effective Hamiltonian in the presence of scalar NSI can be written as

$$H \simeq \frac{M_{\text{eff}} M_{\text{eff}}^\dagger}{2E} \pm V, \tag{8.12}$$

where we have defined $M_{\text{eff}} \equiv M + \delta M$ and V denotes the standard matter potential arising from the MSW effect. Equation 8.12 explicitly shows that the scalar interaction enters through a correction of the neutrino mass matrix rather than as an additional potential term.

It is convenient to parameterize δM as

$$\delta M = \sqrt{|\Delta m^2_{31}|} \begin{pmatrix} \eta_{ee} & \eta_{e\mu} & \eta_{e\tau} \\ \eta_{\mu e} & \eta_{\mu\mu} & \eta_{\mu\tau} \\ \eta_{\tau e} & \eta_{\tau\mu} & \eta_{\tau\tau} \end{pmatrix}, \tag{8.13}$$

where normalization by $\sqrt{|\Delta m^2_{31}|}$ yields dimensionless parameters $\eta_{\alpha\beta}$, which can thus be directly compared to the atmospheric mass-squared scale. In terms of the underlying couplings,

$$\eta_{\alpha\beta} = \frac{1}{m^2_\phi \sqrt{|\Delta m^2_{31}|}} \sum_f N_f \, y_f \, Y_{\alpha\beta}. \tag{8.14}$$

Assuming that δM is Hermitian, the diagonal elements $\eta_{\alpha\alpha}$ are real, while the off-diagonal elements may in general be complex. In this analysis, we restrict our attention to the diagonal parameters η_{ee}, $\eta_{\mu\mu}$, and $\eta_{\tau\tau}$. We consider three separate cases, each with only one nonzero diagonal entry at a time. The corresponding expressions for M_{eff}, which we use in constructing the modified Hamiltonian for these three cases, are given by:

$$\textbf{Case I: } M_{\text{eff}} = U \, \text{diag}(m_1, m_2, m_3) \, U^\dagger + \sqrt{|\Delta m^2_{31}|} \, \text{diag}(\eta_{ee}, 0, 0) \tag{8.15}$$

$$\textbf{Case II: } M_{\text{eff}} = U \, \text{diag}(m_1, m_2, m_3) \, U^\dagger + \sqrt{|\Delta m^2_{31}|} \, \text{diag}(0, \eta_{\mu\mu}, 0) \tag{8.16}$$

$$\textbf{Case III: } M_{\text{eff}} = U \, \text{diag}(m_1, m_2, m_3) \, U^\dagger + \sqrt{|\Delta m^2_{31}|} \, \text{diag}(0, 0, \eta_{\tau\tau}) \tag{8.17}$$

Since $\eta_{\alpha\beta}$ depends explicitly on the background fermion densities N_f, scalar NSI effects are intrinsically matter-density dependent. In principle, one should rescale η when comparing experiments with different density profiles. However, in long-baseline configurations, the mean matter densities within the Earth are similar enough that we omit this rescaling in our numerical study.

8.2 Simulation and Experimental Setup

In this work, we investigate how sensitive long-baseline neutrino experiments are to scalar NSI. For this purpose, we performed a detailed simulation using the `GLoBES` (General Long Baseline Experiment Simulator) framework [153, 154]. `GLoBES` enables realistic modeling of experimental configurations, incorporating neutrino fluxes, oscillation probabilities, interaction cross sections, detector effects, and systematic uncertainties. The simulation generates predicted event spectra for different oscillation scenarios, which then serve as the basis for the statistical analysis.

8.2.1 Experimental Setups

We consider two long-baseline experiments: the proposed P2SO experiment and the DUNE experiment. The main features of these setups are summarized below.

Protvino-to-Super-ORCA (P2SO)

The P2SO experiment aims to send a neutrino beam from Protvino, Russia, to the Super-ORCA detector at the KM3NeT site in the Mediterranean Sea. Although KM3NeT was originally designed for the detection of high-energy astrophysical neutrinos, its Super-ORCA configuration provides a densely instrumented volume suitable for precision accelerator neutrino measurements.

The neutrino beam is produced at the 1.5 km-circumference U-70 synchrotron in Protvino, delivering a beam power of 450 kW, corresponding to 4×10^{20} protons on target per year. The baseline for Super-ORCA is approximately 2595 km, which increases sensitivity to matter effects.

Super-ORCA is a megaton-scale water Cherenkov detector with a densely instrumented geometry optimized for neutrinos in the few-GeV range. Its large fiducial volume and

excellent flavor identification make it ideal for studying ν_μ disappearance and ν_e appearance channels, and for probing the neutrino mass ordering and CP-violating phase.

In our simulations, we assume a total run-time of six years, divided equally between neutrino and antineutrino modes. Detector efficiencies, energy resolutions, and systematic uncertainties are implemented following the specifications provided in the P2SO design studies. This ensures a realistic assessment of the sensitivity of the experiment to both standard and non-standard oscillation parameters.

Deep Underground Neutrino Experiment (DUNE)

DUNE is a next-generation long-baseline neutrino experiment based at Fermilab. The aim is to use a high-intensity neutrino beam, a near detector located 574 m underground and 60 m downstream of the beam source, and a far detector located 1300 km away at the Sanford Underground Research Facility in South Dakota.

The far detector will consist of LArTPC modules, providing a total mass of 40 kt. LArTPC technology will deliver excellent spatial and calorimetric resolution, fully 3D event reconstruction, and robust particle identification through characteristic energy loss patterns, allowing for precise measurements of ν_e appearance and ν_μ disappearance.

The aim is to generate a neutrino beam using 120 GeV protons with an initial beam power of 1.2 MW, corresponding to 1.1×10^{21} protons on target per year. The wide band beam spectrum will cover both the first and second oscillation maxima at 1300 km, thus improving sensitivity to δ_{CP} and to matter effects. In our simulations, we assume a total exposure of 13 years, with equal time allocated to neutrino and antineutrino running. Detector efficiencies, energy resolutions, systematic uncertainties, and background rates follow the specifications of the DUNE technical design report [155, 156].

8.2.2 GLoBES Simulation and Statistical Framework

Using the defined experimental configurations, we perform simulations in `GLoBES`, which computes expected event rates by combining the neutrino flux, oscillation probabilities, interaction cross sections, detector response, and systematic uncertainties.

Event Rate Calculation

For each energy bin i and each oscillation channel, the expected event yield is given by

$$N_i(\vec{\omega}) = T \int_{E_i^{\min}}^{E_i^{\max}} \Phi(E)\, P_{\alpha\beta}(E, \vec{\omega})\, \sigma_\beta(E)\, \epsilon(E)\, R(E, E')\, dE, \tag{8.18}$$

where T denotes the exposure (detector mass multiplied by running time), $\Phi(E)$ is the neutrino flux, $P_{\alpha\beta}$ the oscillation probability, $\sigma_\beta(E)$ the interaction cross section, $\epsilon(E)$ the detector efficiency, and $R(E, E')$ the energy resolution function. The vector $\vec{\omega}$ represents the set of oscillation parameters together with any NSI parameters.

Definition of the χ^2 Function

To estimate the experimental sensitivities, we adopt a Poisson log-likelihood approach and assume that it is distributed as χ^2. The statistical contribution to χ^2 is given by

$$\chi^2_{\text{stat}} = 2 \sum_{i=1}^{n} \left[N_i^{\text{test}} - N_i^{\text{true}} - N_i^{\text{true}} \ln \left(\frac{N_i^{\text{test}}}{N_i^{\text{true}}} \right) \right], \tag{8.19}$$

where N_i^{test} and N_i^{true} denote the expected number of events in the test and true spectra, respectively, and the index i labels the reconstructed energy bins.

Inclusion of Systematic Uncertainties

Systematic uncertainties are implemented via the pull method [157, 158]:

$$N_i^{\text{test}} \to N_i^{\text{test}} \left(1 + \sum_k \pi_i^k \xi_k \right), \tag{8.20}$$

Systematics	P2SO	DUNE
Sig-norm ν_e	5%	2%
Sig-norm ν_μ	5%	5%
Bkg-norm	12%	5% to 20%
Sig-shape	11%	-
Bkg-shape	4% to 11%	-

Table 8.1: The systematic uncertainties included in our analysis are listed here. "norm" denotes the normalization uncertainty, "Sig" refers to the signal, and "Bkg" refers to the background.

where nuisance parameters ξ_k denote fractional systematic effects. The total χ^2 is given by

$$\chi^2 = \chi^2_{\text{stat}} + \sum_k (\xi_k/\sigma_k)^2, \tag{8.21}$$

and is minimized with respect to all ξ_k. In this work, we include both overall normalization and shape uncertainties for the signal and background samples. The systematic error assumptions adopted for P2SO and DUNE are listed in Table 8.1.

Parameter Marginalization

To incorporate uncertainties in the parameters, we marginalize over all oscillation parameters that are not under investigation, using Gaussian priors when suitable. The sensitivity is given by

$$\Delta\chi^2 = \chi^2_{\text{test}} - \chi^2_{\text{true}},$$

interpreted using the Wilks' Theorem.

Inclusion of Non-Standard Interactions

For scalar NSI studies, the modified Hamiltonian is used to compute $P_{\alpha\beta}$. The NSI parameters are included in $\vec{\omega}$ and fixed or marginalized, allowing direct comparison with the standard oscillation hypothesis.

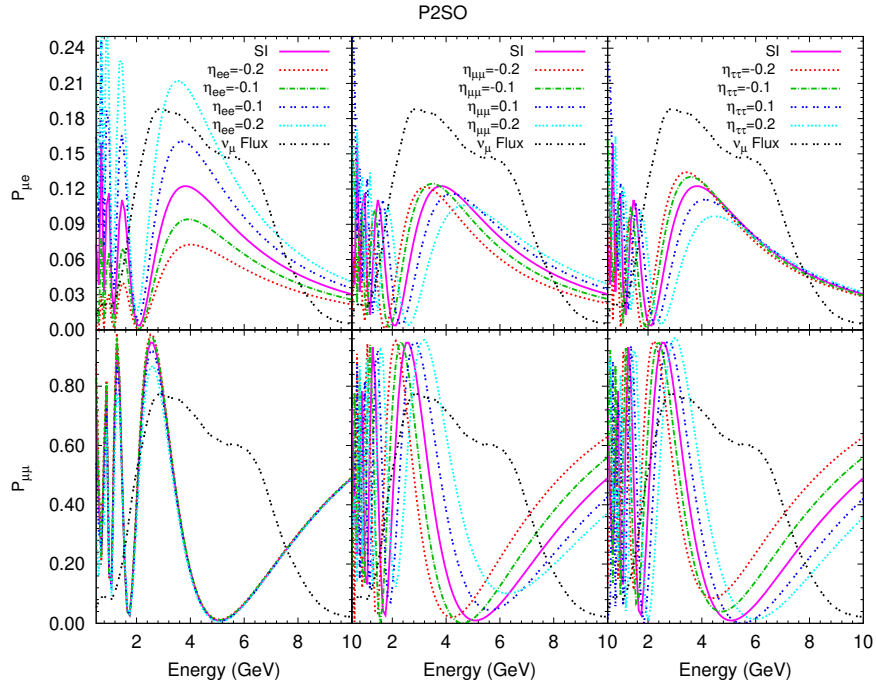


Figure 8.1: Electron neutrino appearance (disappearance) probability as a function of energy for P2SO experiment in upper (lower) panel.

8.3 Oscillation Probabilities in the Presence of Scalar NSI

The formalism of neutrino oscillation in matter, including the role of the effective matter potential and its impact on flavor conversion, has already been discussed in Chapter 7. As emphasized there, matter effects play a crucial role in long-baseline experiments, where coherent forward scattering modifies both the effective mass-squared differences and mixing angles. Since scalar NSI introduce additional modifications to the neutrino mass matrix, their effects can significantly alter the oscillation probabilities in matter. Therefore, a detailed study of oscillation probabilities in the presence of scalar NSI is essential to understand how these new interactions appear in realistic experimental setups and how they can be constrained.

To compute the neutrino oscillation probabilities in the presence of scalar NSI, we have

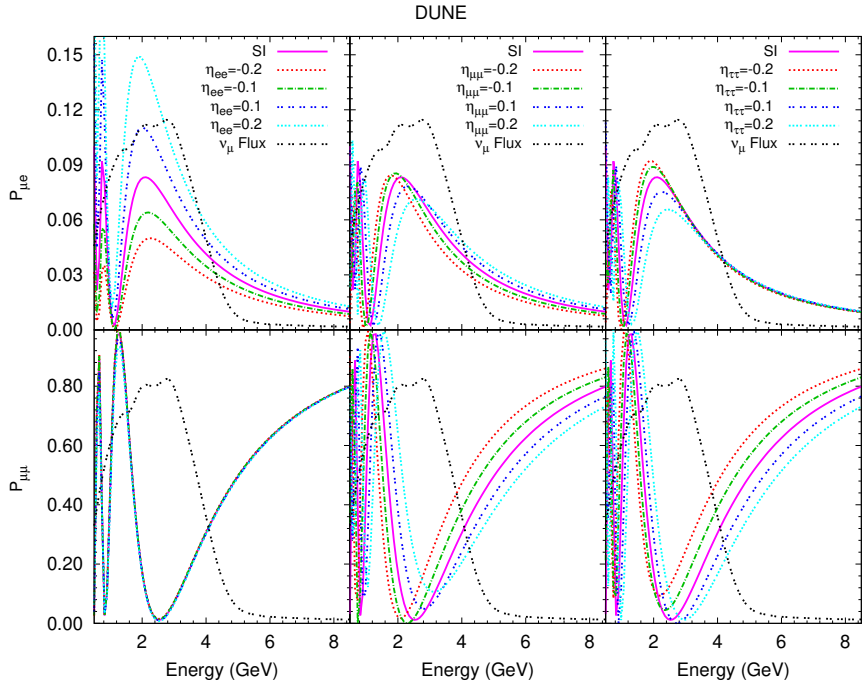


Figure 8.2: Electron neutrino appearance (disappearance) probability as a function of neutrino energy for DUNE experiment in upper (lower) panel.

modified the probability engine of GLoBES. The resulting probabilities are presented in Figure 8.1 for P2SO and in Figure 8.2 for DUNE, considering neutrinos and assuming normal mass ordering. In each case, we vary one diagonal scalar NSI parameter at a time while keeping the others fixed at zero.

In both figures, the upper panels correspond to the appearance channel ($\nu_\mu \to \nu_e$), while the lower panels represent the disappearance channel ($\nu_\mu \to \nu_\mu$). Within each row, the left, middle, and right panels show the effects of η_{ee}, $\eta_{\mu\mu}$, and $\eta_{\tau\tau}$, respectively. Each panel compares the standard three-flavor oscillation probability with the probabilities obtained in the presence of scalar NSI. For illustration, we consider representative values of the diagonal scalar NSI parameters, ± 0.1 and ± 0.2. The energy dependence of the flux ν_μ for each experiment is also shown as a reference.

Parameters	True values $\pm$ 1σ
$\sin^2\theta_{12}$	$0.303^{+0.012}_{-0.011}$
$\sin^2\theta_{13}$	$0.02203^{+0.00056}_{-0.00059}$
$\sin^2\theta_{23}$	$0.572^{+0.018}_{-0.023}$
$\delta_{\rm CP}[^\circ]$	197^{+42}_{-25}
Δm^2_{21} [10^{-5} eV^2]	$7.41^{+0.21}_{-0.20}$
Δm^2_{31} [10^{-3} eV^2]	$2.511^{+0.028}_{-0.027}$

Table 8.2: Oscillation parameter values with their corresponding 1σ errors considered in our analysis [16].

Unless stated otherwise, all results are obtained assuming a normal mass ordering with $m_1 = 10^{-5}$ eV. The input values of the oscillation parameters used in our simulations are summarized in Table 8.2. Throughout this study, we activate only a single scalar NSI parameter at a time, as defined in Equation 8.15, 8.16, and 8.17, while all other NSI parameters are fixed to zero.

From Figure 8.2 and Figure 8.1, we observe that sensitivity to η_{ee} predominantly arises from the appearance channel, while both the appearance and disappearance channels exhibit sensitivity to $\eta_{\mu\mu}$ and $\eta_{\tau\tau}$. Among the three diagonal parameters, η_{ee} is expected to yield the strongest sensitivity.

We also notice distinct features associated with the sign of the scalar NSI parameters. In the appearance channel, negative (positive) values of η_{ee} suppress (enhance) the oscillation probability relative to the standard case. In contrast, the behavior is reversed for $\eta_{\mu\mu}$ and $\eta_{\tau\tau}$. In addition, in the disappearance (appearance) channel, the position of the first oscillation minimum (maximum) shifts in opposite directions for positive and negative values of $\eta_{\mu\mu}$ and $\eta_{\tau\tau}$. In the disappearance channel, the probability at the first oscillation minimum deviates from zero for positive (negative) values of $\eta_{\mu\mu}$ ($\eta_{\tau\tau}$).

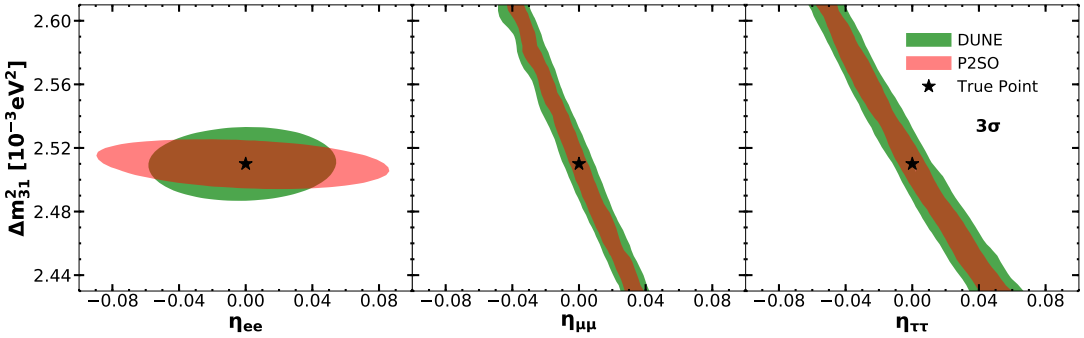


Figure 8.3: Allowed values of Δm^2_{31} at 3σ CL when scalar NSI is fitted in the theory with the standard three flavour scenario in the data.

8.4 Sensitivity to Scalar NSI

We begin by investigating how well P2SO and DUNE can constrain diagonal scalar NSI parameters. The standard procedure is to assume the conventional three-flavor framework in the true event spectrum used for χ^2, introduce scalar NSI only in the test spectrum, and then plot χ^2 as a function of the scalar NSI parameters. Before presenting these sensitivity curves, it is important to clarify how Δm^2_{31} affects the resulting bounds on the scalar NSI couplings. For this purpose, in Figure 8.3 we show the 3σ allowed region in the plane η (test)–Δm^2_{31} (test), assuming the standard three-flavor scenario in the true spectrum. The left, middle and right panels correspond to η_{ee}, $\eta_{\mu\mu}$, and $\eta_{\tau\tau}$, respectively. In producing this figure, all parameters not explicitly displayed (with the exception of $\delta_{\rm CP}$) are marginalized, using Gaussian priors determined by their 1σ uncertainties given in Table 8.2. The parameter $\delta_{\rm CP}$ is marginalized without any prior. The green (red) shaded region shows the parameter space allowed by DUNE (P2SO). In every panel, the y-axis range is set to the current 3σ interval for Δm^2_{31} from NuFIT 5.2.

From the figure, we observe that for the parameter η_{ee}, the standard scenario cannot be reproduced using scalar NSI if Δm^2_{31} takes values outside its current 3σ interval. Because, in this case the allowed regions for both DUNE and P2SO do not extend beyond the dis-

played range of Δm^2_{31} on the y-axis. In contrast, for $\eta_{\mu\mu}$ and $\eta_{\tau\tau}$, the standard scenario can be fitted with a scalar NSI even when Δm^2_{31} lies outside its current 3σ allowed range. This is evident from the fact that for these two parameters, the contours stretch beyond the plotted y-axis limits of Δm^2_{31}. We have explicitly checked that this situation does not occur with any other parameter. As a result, when setting the limits in $\eta_{\mu\mu}$ and $\eta_{\tau\tau}$, the value of Δm^2_{31} at which the function χ^2 reaches its minimum can fall outside the current allowed range within 3σ. We have explicitly checked that this issue does not occur for any of the other parameters. Hence, it is essential to treat minimization with respect to this parameter with particular care when deriving the bounds on $\eta_{\mu\mu}$ and $\eta_{\tau\tau}$. If we perform the minimization with a prior corresponding to the uncertainty 1σ in Δm^2_{31}, there is a possibility that the χ^2 minimizer will be trapped in a local minimum close to the true value. Conversely, if we minimize this parameter without any prior, the global χ^2 minimum may occur at values of Δm^2_{31} lying outside its currently allowed 3σ range. To avoid this problem, we adopt a systematic sampling, rather than a random sampling, of this parameter: we vary Δm^2_{31} only within its current 3σ allowed region and then select the corresponding minimum of χ^2. It is important to emphasize that the current 3σ interval for Δm^2_{31} has been obtained within the standard three-flavor framework. If, instead, this parameter were determined assuming scalar NSI in the theoretical description, the allowed 3σ range could be broadened to include larger values of Δm^2_{31}. To account for such a possibility, one might consider minimizing this parameter with a flat prior. Since we currently have no evidence that this is the case, we choose to vary Δm^2_{31} only within its presently established 3σ range.

In Figure 8.4, we present the constraints on the diagonal scalar NSI parameters obtained using the approach outlined in the previous paragraph. The left, middle, and right panels display the limits on η_{ee}, $\eta_{\mu\mu}$, and $\eta_{\tau\tau}$, respectively. In each panel, the blue curve corresponds to the constraint from DUNE, while the red curve indicates the constraint from the P2SO experiment. From the figure we see that stringent bounds can be obtained on these

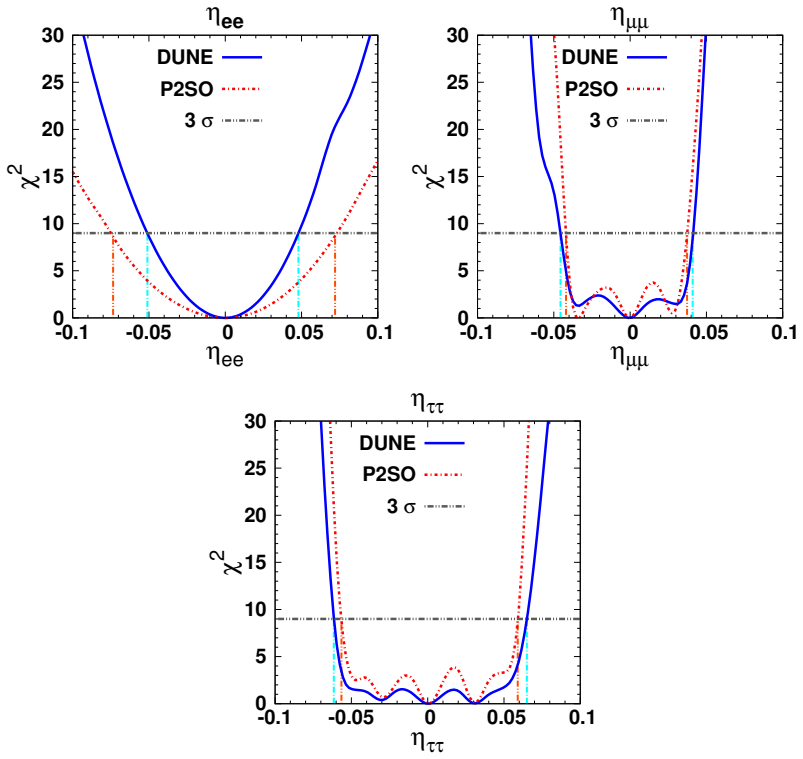


Figure 8.4: Bounds on the scalar NSI diagonal parameters ($\eta_{ee}, \eta_{\mu\mu}$ and $\eta_{\tau\tau}$) from DUNE and P2SO experiments.

parameters from both experiments. DUNE is better than P2SO to constrain the parameter η_{ee} in 3σ CL While in the cases of $\eta_{\mu\mu}$ and $\eta_{\tau\tau}$, the limits of P2SO and DUNE are similar. The sensitivity limits of the parameters at 3σ CL are shown in Table 8.3. The table shows that the bounds from DUNE and P2SO are more or less similar except the case of η_{ee}.

Parameters	DUNE	P2SO
η_{ee}	[-0.051, 0.048]	[-0.075, 0.073]
$\eta_{\mu\mu}$	[-0.0457,0.041]	[-0.042, 0.038]
$\eta_{\tau\tau}$	[-0.061, 0.065]	[-0.057, 0.059]

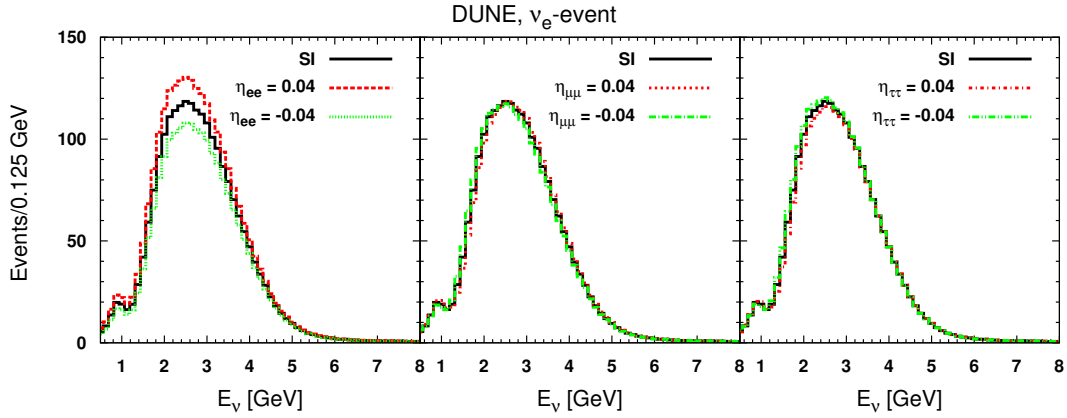
Table 8.3: Sensitivity limits on the scalar NSI parameters at 3σ CL from DUNE and P2SO experiment.

8.5 Impact of Scalar NSI on Event Rates and Precision Measurements

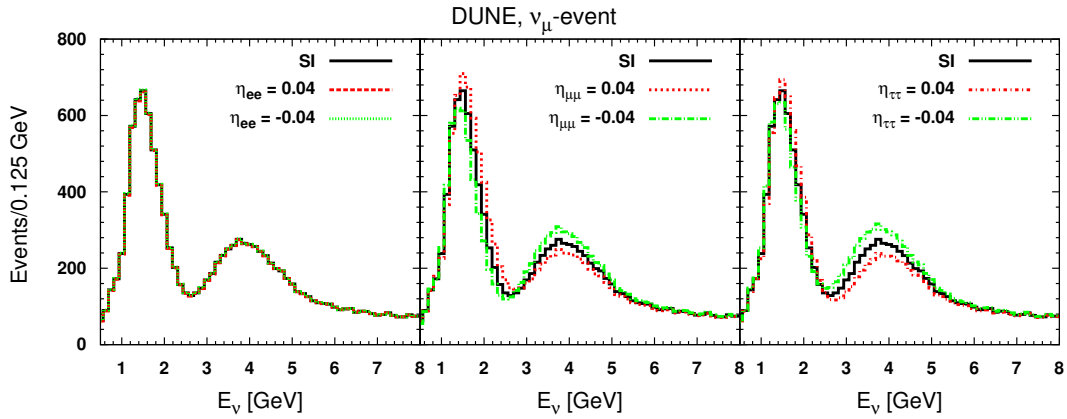
In this section, we examine the impact of scalar NSI on precision measurements at P2SO and DUNE. Because scalar NSI modify the neutrino mass matrix, they can imitate or distort the extraction of the standard oscillation parameters. At P2SO and DUNE, matter effects are substantial and the oscillation pattern is determined with high statistics, so even small scalar-induced corrections can shift the position and alter the height of the oscillation maxima and minima. This in turn influences the sensitivity to CP violation, the determination of mass ordering, and the resolution of the θ_{23} octant. The appearance channel ($\nu_\mu \to \nu_e$), which is the main channel for accessing the CP phase, is especially sensitive to η_{ee}, while both appearance and disappearance data constrain θ_{23} and Δm^2_{31} via $\eta_{\mu\mu}$ and $\eta_{\tau\tau}$. As a result, scalar NSI can generate new parameter degeneracies, enlarge the allowed regions in the oscillation parameter space, and potentially bias the extracted parameter values if they are neglected. It is therefore crucial to quantify the impact of scalar NSI to ensure the reliability of precision oscillation measurements at upcoming long-baseline experiments.

8.5.1 Effect on Event Spectra

To demonstrate how the appearance and disappearance channels help constrain the diagonal scalar NSI parameters, Figure 8.5 shows the predicted DUNE event spectra as functions of neutrino energy, comparing the standard oscillation case with scenarios including scalar NSI. For this illustration, we adopt $|\eta_{ee}| = |\eta_{\mu\mu}| = |\eta_{\tau\tau}| = 0.04$, values that are within the current 3σ experimental limits summarized in Table 8.3. The upper panel displays the appearance ($\nu_\mu \to \nu_e$) event rates, while the lower panel shows the disappearance ($\nu_\mu \to \nu_\mu$) rates. The solid black curves correspond to the standard-oscillation prediction, whereas the red (green) dashed curves represent positive (negative) scalar NSI, with parameter values



(a)



(b)

Figure 8.5: Number of neutrino events as a function of neutrino energy in the DUNE experiment for (a) the appearance channel and (b) the disappearance channel.

$+0.04$ (-0.04). Comparing these spectra reveals how scalar NSI alter both the shape and overall normalization of the event distributions in each channel, thereby influencing the accuracy with which the oscillation parameters can be determined.

From the figure, it is evident that the scalar NSI parameter η_{ee} has a significant impact on ν_e appearance events, while it induces only a modest modification in ν_e disappearance events. In contrast, for the parameters $\eta_{\mu\mu}$ and $\eta_{\tau\tau}$, a substantial effect is predominantly observed in the disappearance channel. In addition, the scalar NSI parameters can either

enhance or suppress the event rates, depending on their sign. For example, in the appearance channel, the event rates increase (decrease) for positive (negative) values of η_{ee}.

8.5.2 Effect on Precision Measurement of θ_{23} and Δm^2_{31}

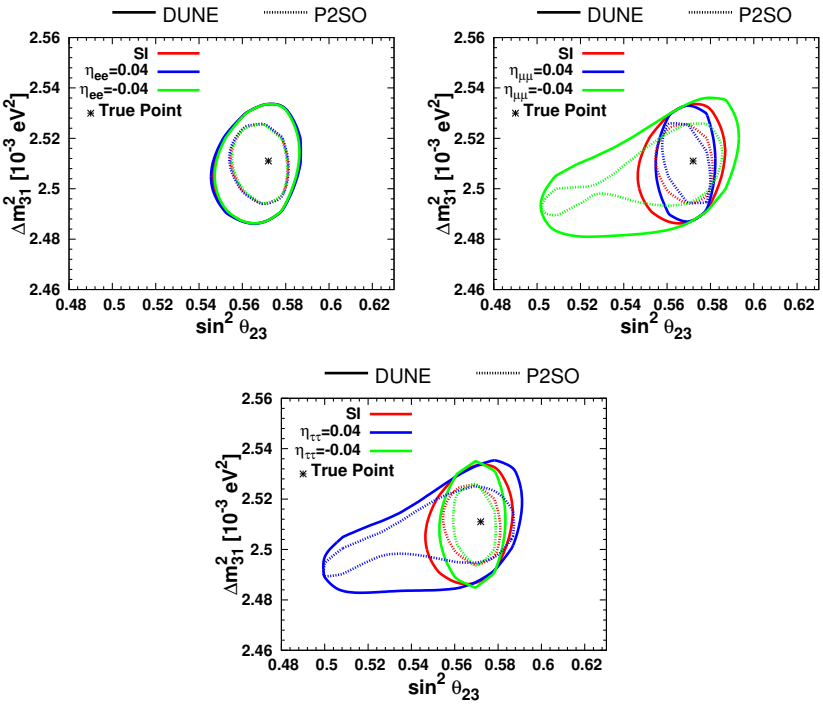


Figure 8.6: Allowed region between $\sin^2\theta_{23} - \Delta m^2_{31}$ at 3σ CL in standard and in presence of scalar NSI parameters for DUNE and P2SO experiment.

We now examine how scalar NSI affects the precision in determining the atmospheric mixing angle θ_{23} and the mass-squared difference Δm^2_{31}. By comparing the allowed regions in the θ_{23}–Δm^2_{31} plane with and without scalar NSI, we quantify possible degradations in sensitivity, shifts in the best-fit values, and the emergence of new parameter degeneracies. This provides a direct assessment of the extent to which scalar NSI effects could bias the precision measurements expected from current and future long-baseline experiments.

Figure 8.6 displays the allowed region in the test-parameter plane spanned by $\sin^2\theta_{23}$

and Δm^2_{31} at 3σ CL, obtained by fixing all three scalar NSI parameters to ± 0.04 in both the true and test spectra entering the χ^2 analysis. The true values of $\sin^2\theta_{23}$ and Δm^2_{31} are indicated by a star. All other oscillation parameters (except for $\delta_{\rm CP}$), which are not explicitly shown in the panels, are marginalized using random sampling with Gaussian priors corresponding to their 1σ uncertainties. The parameter $\delta_{\rm CP}$ is varied with a flat prior. The solid curves correspond to the DUNE experiment, while the dashed curves correspond to P2SO. In each panel, the red curve represents the standard interaction scenario, whereas positive (negative) values of the NSI parameters are represented by blue (green) curves.

In the standard interaction case, the allowed region is more constrained for P2SO than for DUNE. The effects of the three scalar NSI parameters are clearly distinguishable from each other. For η_{ee}, there is no significant impact on the precision of θ_{23} and Δm^2_{31}. A stronger effect is seen for $\eta_{\mu\mu}$ and $\eta_{\tau\tau}$. For negative values of $\eta_{\mu\mu}$, the allowed parameter region enlarges, while for $\eta_{\tau\tau}$ the allowed region increases for positive values of $\eta_{\tau\tau}$. In both cases, the sensitivity to $\sin^2\theta_{23}$ is degraded, while the precision on Δm^2_{31} remains largely unaffected. Importantly, the values of Δm^2_{31} in 3σ CL remain well within the current allowed range reported by NuFit 5.2. Therefore, when scalar NSI are included in both the true and test hypotheses, it is sufficient to marginalize over Δm^2_{31} using a Gaussian prior with its 1σ uncertainty.

To be consistent with Figure 8.4, in the subsequent discussion, where we examine how well P2SO and DUNE can determine unknowns related to the standard oscillation parameters in the presence of scalar NSI, we systematically marginalize over Δm^2_{31} across its current 3σ range. Throughout this analysis, the scalar NSI parameters are fixed to ± 0.04 in both the true and test setups.

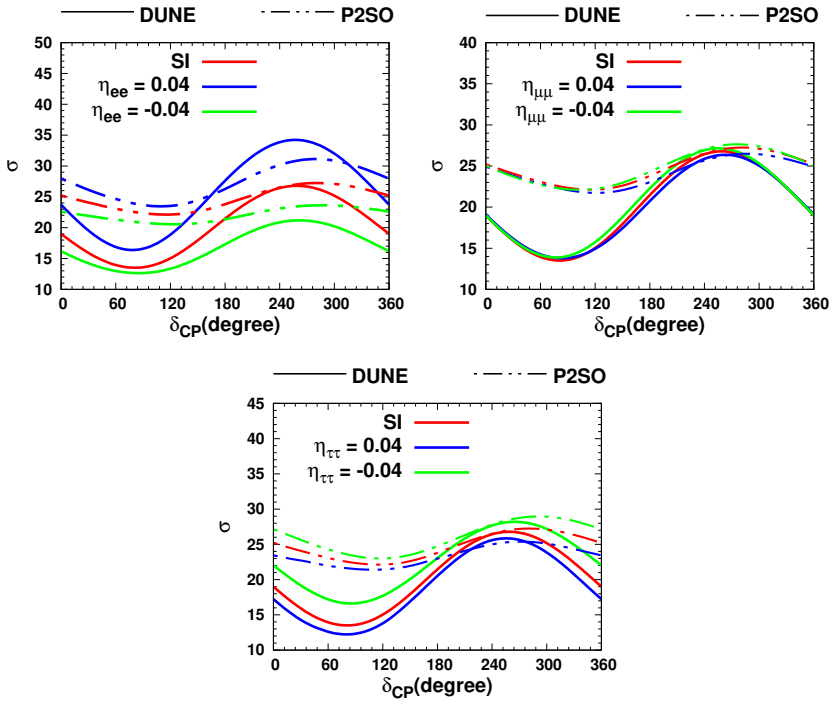


Figure 8.7: Mass hierarchy sensitivity of the scalar NSI diagonal parameters ($\eta_{ee}, \eta_{\mu\mu}$ and $\eta_{\tau\tau}$) for the DUNE and P2SO experiments.

8.5.3 Sensitivity to Mass Ordering

Here, we investigate the sensitivity to the neutrino mass ordering in the presence of scalar NSI, as presented in Figure 8.7, where the sensitivity is shown as a function of the true value of $\delta_{\rm CP}$. This figure demonstrates how well the experiments can identify the correct mass ordering. The sensitivity is obtained by assuming that the normal ordering is the true hierarchy and testing it against the inverted ordering. For the inverted ordering, we set $m_3 = 10^{-5}$ eV and compute the remaining masses as $m_1 = \sqrt{m_3^2 + \Delta m_{31}^2}$ and $m_2 = \sqrt{m_1^2 + \Delta m_{21}^2}$. The solid and dashed lines represent DUNE and P2SO, respectively. In every panel, the standard scenario is indicated by the red curve, while the blue (green) curve corresponds to $\eta_{\alpha\alpha} = +0.04\ (-0.04)$. The left, central, and right panels illustrate the impact of η_{ee}, $\eta_{\mu\mu}$, and $\eta_{\tau\tau}$, respectively.

Appearance channel event difference (Normal ordering - Inverted ordering)			
Experiments	$\eta = 0.04$	$\eta = 0$	$\eta = -0.04$
P2SO (η_{ee})	6992	6273	5609
DUNE (η_{ee})	360	244	150
P2SO ($\eta_{\tau\tau}$)	5336	6273	7510
DUNE ($\eta_{\tau\tau}$)	151	244	343

Table 8.4: Appearance channel event difference for P2SO and DUNE for $\delta_{CP}^{\text{true}} = 90^o$. These events corresponds to 3 years running of P2SO and 6.5 year running of DUNE.

From the figure, we observe that both experiments exhibit very strong sensitivity to the neutrino mass ordering. Throughout almost the entire δ_{CP} range, the P2SO setup provides better sensitivity than DUNE in the standard scenario. Including scalar NSI alters the mass-ordering sensitivity more strongly for η_{ee} than for $\eta_{\mu\mu}$ or $\eta_{\tau\tau}$, and the sensitivity may increase or decrease with the sign of $\eta_{\alpha\beta}$. Compared to the standard three-flavor framework, a positive (negative) value of η_{ee} enhances (reduces) the sensitivity. For $\eta_{\tau\tau}$, the behavior is reversed. This behavior is summarized in Table 8.4, which presents the difference in the number of events (N) between normal ordering and inverted ordering in the appearance channel for $\delta_{\text{CP}}(\text{true}) = 90^\circ$ for both P2SO and DUNE. The event rates for normal ordering are computed at the true values of the oscillation parameters, whereas the event rates for inverted ordering are obtained at the point corresponding to the minimum of χ^2.

From this table, we see that the value of N increases (decreases) relative to the standard scenario when η_{ee} is positive (negative), whereas the opposite trend is observed for $\eta_{\tau\tau}$. This behavior accounts for the enhanced (reduced) mass-ordering sensitivity in the presence of a positive (negative) η_{ee} and a negative (positive) $\eta_{\tau\tau}$.

8.5.4 Sensitivity to CP Violation

Here, we evaluate the sensitivity to CP violation in the lepton sector. High sensitivity to CP violation is crucial for detecting small deviations from CP conservation, thereby testing the Standard Model and its extensions, and for probing whether leptonic CP violation can

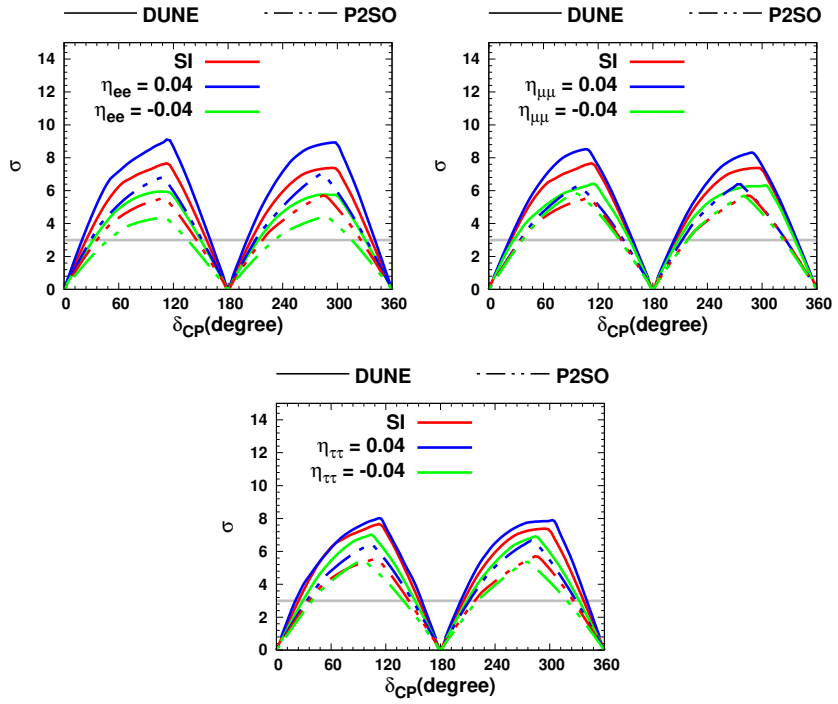


Figure 8.8: CPV sensitivity of the scalar NSI diagonal parameters ($\eta_{ee}, \eta_{\mu\mu}$ and $\eta_{\tau\tau}$) for DUNE and P2SO experiment.

explain the matter–antimatter asymmetry in the universe. We characterize the sensitivity by the expected significance with which $\delta_{\rm CP}$ can be distinguished from CP-conserving values, taking into account both statistical and systematic uncertainties.

Figure 8.8 displays the sensitivity to CP violation as a function of the true value of $\delta_{\rm CP}$ for the DUNE and P2SO experiments. Specifically, it illustrates the capability of these experiments to exclude the CP-conserving values of $\delta_{\rm CP}$. For each assumed true value of $\delta_{\rm CP}$, we compute the minimum χ^2 obtained when the test values of $\delta_{\rm CP}$ are fixed to the CP-conserving hypotheses, 0° and 180°. The solid and dashed curves correspond to the sensitivities of DUNE and P2SO, respectively. In each panel, the red curves represent the standard interaction scenario, while the blue and green curves correspond to scenarios with scalar NSI parameters set to $+0.04$ and -0.04, respectively. The left, middle, and right

panels show results for the parameters η_{ee}, $\eta_{\mu\mu}$, and $\eta_{\tau\tau}$, respectively.

From these results, it can be concluded that, under standard interaction assumptions, the DUNE experiment shows greater CPV sensitivity than the P2SO experiment. The impact of the scalar NSI parameters is strongly parameter dependent. The parameters η_{ee} and $\eta_{\mu\mu}$ produce a substantially larger modification of the CPV sensitivity than $\eta_{\tau\tau}$. A positive value of $\eta_{\alpha\alpha}$ improves the CPV sensitivity, whereas a negative value leads to a reduction in the sensitivity.

8.5.5 Sensitivity for Octant of θ_{23}

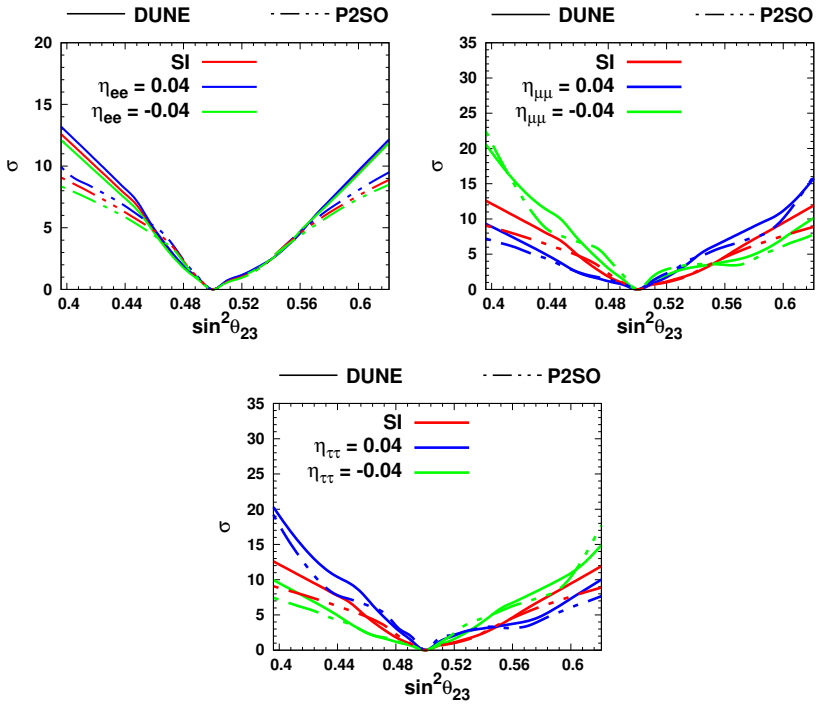


Figure 8.9: Octant sensitivity of the scalar NSI diagonal parameters ($\eta_{ee}, \eta_{\mu\mu}$ and $\eta_{\tau\tau}$) for DUNE and P2SO experiments.

Determining the octant of θ_{23} (whether $\theta_{23} < 45°$ or $\theta_{23} > 45°$) is crucial for understanding the underlying flavor structure of neutrinos and the origin of their masses and mixings.

The value of θ_{23} directly affects the pattern of atmospheric neutrino oscillations and therefore provides insight into whether the mixing between muon and tau neutrinos is exactly maximal or not. A deviation from maximal mixing, along with a clear identification of the octant, can discriminate among competing theoretical models of neutrino mass generation and flavor symmetries, many of which predict specific ranges or correlations for θ_{23}. In addition, the octant of θ_{23} is correlated with other key oscillation parameters, such as the CP-violating phase δ_{CP} and the neutrino mass ordering, thus resolving the octant ambiguity improves global fits of neutrino parameters and enhances the physics reach of current and future long-baseline experiments. Therefore, the sensitivity to the octant of θ_{23} is an essential benchmark to assess the capability of any experimental setup to obtain a complete picture of neutrino oscillations.

Figure 8.9 presents the octant sensitivity as a function of the true value of $\sin^2\theta_{23}$. To obtain this figure, when the true $\sin^2\theta_{23}$ lies in the lower octant, the test $\sin^2\theta_{23}$ is scanned over the higher octant and vise versa. In each panel, the red curve corresponds to the standard scenario, while the blue (green) curve corresponds to $\eta_{\alpha\alpha} = +0.04\ (-0.04)$. The left, middle and right panels illustrate the cases for η_{ee}, $\eta_{\mu\mu}$, and $\eta_{\tau\tau}$, respectively.

From the figure, it can be concluded that in the standard scenario, the sensitivity of DUNE is slightly higher than that of P2SO. When taking into account the subleading scalar NSI parameters, η_{ee} has the weakest impact on sensitivity. In contrast, the parameters $\eta_{\mu\mu}$ and $\eta_{\tau\tau}$ induce a pronounced modification of the sensitivity. For $\eta_{\mu\mu}$, the sensitivity improves for positive values and decreases for negative values. This behavior is inverted in the presence of $\eta_{\tau\tau}$, for which positive values reduce the sensitivity and negative values enhance it.

8.6 Conclusion

In this chapter, we studied the scalar NSI in the proposed P2SO experiment and compare its sensitivity to DUNE. Scalar NSI modify the neutrino mass terms in the oscillation Hamiltonian, introducing dependence on the absolute neutrino mass scale and extending the parameter space by three real and three complex parameters. We focused on the real parameters η_{ee}, $\eta_{\mu\mu}$, and $\eta_{\tau\tau}$ and their impact on both the scalar NSI constraints and the determination of the standard oscillation parameters.

At both the probability and event levels, the appearance channel mainly drives the sensitivity to η_{ee}, while the disappearance channel dominates for $\eta_{\mu\mu}$ and $\eta_{\tau\tau}$. We find that DUNE provides a stronger constraint on η_{ee}, whereas both experiments show comparable sensitivity to $\eta_{\mu\mu}$ and $\eta_{\tau\tau}$. For the latter two parameters, the constraints depend significantly on the treatment of Δm^2_{31}, which requires minimization over its current range 3σ. The effect of the lightest neutrino mass is negligible for $m_1 < 0.01$ eV, but becomes relevant for larger values.

We also found that non-zero $\eta_{\mu\mu}$ and $\eta_{\tau\tau}$ significantly worsen the precision of θ_{23}, while the precision of Δm^2_{31} remains largely unchanged. In contrast, η_{ee} has little effect on the precision of either parameter. The strongest impact on mass-ordering and CP-violation sensitivities arises from η_{ee}, while the largest modification to θ_{23} octant sensitivity is observed for $\eta_{\tau\tau}$. Depending on the signs of the scalar NSI parameters, these sensitivities can either improve or deteriorate relative to the standard three-flavor scenario.

Overall, the study of NSIs provides an important framework for probing physics beyond the Standard Model through neutrino oscillation experiments. Both vector and scalar NSI can introduce significant modifications to neutrino propagation, influencing the precise determination of oscillation parameters and the extraction of key unknown quantities. As upcoming long-baseline experiments such as DUNE, P2SO, and Hyper-Kamiokande reach

unprecedented precision, they will become highly sensitive to these potential new physics contributions. Therefore, investigating NSI not only helps in constraining possible new interactions but also supports a reliable interpretation of forthcoming neutrino oscillation data, both within and beyond the standard three-flavor framework.

Chapter 9

Summary

In summary, this thesis presents two complementary strategies for probing physics beyond the Standard Model: direct searches for extremely rare exotic particles such as magnetic monopoles, and probing scalar NSI in next-generation experiments like P2SO, whose sensitivity is compared with that of DUNE. While magnetic monopole searches focus on discovering completely new particles with distinctive experimental signatures, the NSI framework explores possible modifications to neutrino propagation and mixing behavior.

Magnetic monopoles are hypothetical particles predicted in several extensions of the Standard Model, including GUTs. Their discovery would have profound implications for our understanding of fundamental interactions, in particular charge quantization and the structure of gauge theories.

This study investigates the sensitivity of the NOvA detector, located on the Earth's surface, to highly ionizing magnetic monopoles. Within this framework, monopoles are expected to produce highly distinctive signatures in the liquid scintillator, because their large effective charge leads to intense ionization and significant light emission while traversing detector materials. In the detector, this appears as a characteristic track with an exceptionally high light yield, accompanied by additional phenomena such as Cherenkov radiation for very fast monopoles.

The key challenge in this study is extracting the monopole signal from an intense cosmic-ray background, which includes a cosmic muon rate of 150 kHz. NOvA uses a dedicated data-driven monopole trigger that continuously looks for monopole-like patterns, specifically, highly ionizing, through-going particles in the cosmic flux, while keeping the over-

all trigger rate very low. We have implemented novel simulation and analysis techniques to recognize this highly ionizing signature and, using 2,713 days of data, NOvA sets a world-leading limit on low-mass monopoles. We obtain the most stringent bound to date of 8×10^{-16} cm^{-2} s^{-1} sr^{-1} (90% CL) in the velocity range $0.005 < \beta < 0.8$, which corresponds to monopoles with masses higher than 10^9 GeV at all speeds and higher than 10^7 GeV for $\beta > 0.1$. Over the same β interval, for higher-mass monopoles that can traverse the Earth, we derive an upper flux limit of 2×10^{-16} cm^{-2} s^{-1} sr^{-1} (90% CL), corresponding to monopole masses greater than 10^{15} GeV and 10^{13} GeV for $\beta > 0.1$.

The second part of this thesis examines the role of scalar NSI in upcoming long-baseline neutrino experiments, specifically P2SO and DUNE. Scalar NSI provides a well-motivated extension of the neutrino sector beyond the Standard Model. They affect neutrino oscillations by directly modifying the neutrino mass matrix. This modification arises from effective Yukawa-like couplings to a scalar mediator, which generate density-dependent shifts in the neutrino masses. These interactions are typically described by dimensionless parameters $\eta_{\alpha\beta}$, which quantify their strength relative to the Fermi constant. This work demonstrates that scalar NSI can significantly impact the extraction of oscillation parameters, making it crucial to place stringent constraints on these interactions.

At the probability level, the sensitivity to η_{ee} arises primarily from the appearance channel, whereas the sensitivities to $\eta_{\mu\mu}$ and $\eta_{\tau\tau}$ are mainly governed by the disappearance channel. DUNE provides a tighter bound on η_{ee} than P2SO, while the two experiments yield similar constraints on $\eta_{\mu\mu}$ and $\eta_{\tau\tau}$. The event-level analysis shows that the appearance channel predominantly determines the sensitivity to η_{ee}, whereas the disappearance channel governs the sensitivities to $\eta_{\mu\mu}$ and $\eta_{\tau\tau}$.

In the presence of scalar NSI, the precision on the mixing angle θ_{23} deteriorates significantly for non-zero values of $\eta_{\mu\mu}$ and $\eta_{\tau\tau}$, while the precision on Δm^2_{31} remains largely unaffected. In contrast, for non-zero η_{ee}, the precisions of both Δm^2_{31} and θ_{23} are essentially

unchanged relative to the standard three-flavor oscillation framework without scalar NSI.

Regarding sensitivities, the impact of scalar NSI on the sensitivities to the neutrino mass ordering and to leptonic CP violation is found to be most pronounced for η_{ee}, in comparison with the corresponding effects of $\eta_{\mu\mu}$ and $\eta_{\tau\tau}$. In contrast, the modification of the octant sensitivity of θ_{23} is largest for $\eta_{\tau\tau}$. Depending on the relative signs of the scalar NSI parameters, these sensitivities may be either enhanced or reduced compared to those predicted in the standard three-flavor oscillation framework.

Together, these complementary beyond the Standard Model investigations of magnetic monopoles and scalar NSI in the neutrino sector highlight the broad discovery potential of current and next generation neutrino experiments and offer a promising route to achieving deeper understanding of fundamental interactions and the underlying structure of the Universe.

References

[1] Arttu Rajantie. Introduction to Magnetic Monopoles. *Contemp. Phys.*, 53:195–211, 2012.

[2] Laura Patrizii and Maurizio Spurio. Status of searches for magnetic monopoles. *Annual Review of Nuclear and Particle Science*, 65:279–302, 2015.

[3] D. S. Ayres et al. The NOvA Technical Design Report. 10 2007.

[4] Zukai Wang. *Search for Magnetic Monopoles with the NOvA Far Detector*. PhD thesis, Physics - Graduate School of Arts and Sciences, University of Virginia, Virginia U., 2015.

[5] A Aurisano, C Backhouse, R Hatcher, N Mayer, J Musser, R Patterson, R Schroeter, and A Sousa. The nova simulation chain. *Journal of Physics: Conference Series*, 664(7):072002, dec 2015.

[6] Adam M. Dziewonski and Don L. Anderson. Preliminary reference earth model. *Physics of the Earth and Planetary Interiors*, 25(4):297–356, 1981.

[7] B. Cabrera. First results from a superconductive detector for moving magnetic monopoles. *Physical Review Letters*, 48:1378–1381, 1982.

[8] S. Balestra et al. Magnetic monopole search with the slim experiment. *European Physical Journal C*, 55:57, 2008.

[9] M. et al. Ambrosio. Final results of magnetic monopole searches with the macro experiment. *European Physical Journal C*, 25:511–522, 2002.

[10] Philippe H. Eberhard, Ronald R. Ross, Luis W. Alvarez, and Robert D. Watt. Search for magnetic monopoles in lunar material. *Phys. Rev. D*, 4:3260–3272, Dec 1971.

[11] A. Albert et al. Search for magnetic monopoles with the complete antares dataset, 2025.

[12] R. Abbasi et al. Search for relativistic magnetic monopoles with eight years of ice-cube data. *Phys. Rev. Lett.*, 128:051101, Feb 2022.

[13] Wikipedia Commons. Standard model of elementary particles. https://commons.wikimedia.org/wiki/File.

[14] L. Kolupaeva, O. Samoylov, and I. Shandrov. Matter effect in neutrino oscillations for long-baseline experiments. *Phys. Part. Nucl. Lett.*, 14(7):975–980, 2017.

[15] Ivan Esteban, M. C. Gonzalez-Garcia, Michele Maltoni, Ivan Martinez-Soler, João Paulo Pinheiro, and Thomas Schwetz. Nufit-6.0: updated global analysis of three-flavor neutrino oscillations. *Journal of High Energy Physics*, 2024(12):216, 2024.

[16] Ivan Esteban, M. C. Gonzalez-Garcia, Michele Maltoni, Thomas Schwetz, and Albert Zhou. The fate of hints: updated global analysis of three-flavor neutrino oscillations. *JHEP*, 09:178, 2020.

[17] Petrus Peregrinus of Maricourt. *Epistola de magnete*. 1269. Early treatise on magnetism.

[18] R. Norman. *The Newe Attractive: London, 1581*. English Experience. Its Record in early printed Books published in Facsimile. Theatrum Orbis Terrarum. Norwood, N.J.

[19] W. Gilbert and P. Short. *Gulielmi Gilberti ... De magnete, magneticisque corporibus, et de magno magnete tellure: physiologia noua plurimis et argumentis, et experimentis demonstrata*. Biblioteca digital Dioscórides. excudebet Petrus Short, 1600.

[20] André-Marie Ampère. Sur la détermination expérimentale des relations qui existent entre les forces électrodynamiques. *Annales de Chimie et de Physique*, 15:59–76, 1820.

[21] Michael Faraday. On some new electro-magnetical motions, and on the theory of magnetism. *Philosophical Transactions of the Royal Society*, 121:163–194, 1831.

[22] James Clerk Maxwell. A dynamical theory of the electromagnetic field. *Philosophical Transactions of the Royal Society of London*, 155:459–512, 1865.

[23] Pierre Curie. Sur la possibilité d'existence de la conductibilité magnétique et du magnétisme libre. *Journal de Physique Théorique et Appliquée*, 3:415–417, 1894.

[24] P. A. M. Dirac. Quantised singularities in the electromagnetic field. *Proceedings of the Royal Society of London A*, 133(821):60–72, 1931.

[25] G. 't Hooft. Magnetic monopoles in unified gauge theories. *Nuclear Physics B*, 79:276–284, 1974.

[26] A. M. Polyakov. Particle spectrum in quantum field theory. *JETP Letters*, 20:194–195, 1974.

[27] J. Preskill. Magnetic monopoles. *Annual Review of Nuclear and Particle Science*, 34:461–530, 1984.

[28] J. D. Jackson. *Classical Electrodynamics*, volume 3rd edition. 1999. Textbook.

[29] Paul Langacker. Grand unified theories and proton decay. *Physics Reports*, 72:185–385, 1981.

[30] Ya. M. Shnir. *Magnetic Monopoles*. Springer, 2005.

[31] John Preskill. Cosmological production of superheavy magnetic monopoles. *Physical Review Letters*, 43:1365–1368, 1979.

[32] M. A. Acero et al. Search for slow magnetic monopoles with the nova detector on the surface. *Phys. Rev. D*, 103:012007, Jan 2021.

[33] S. Abubakar et al. Ionization-based search for magnetic monopoles using the nova far detector. *Phys. Rev. D*, Apr 2026.

[34] M. G. et al. Aartsen. Search for relativistic magnetic monopoles with icecube. *European Physical Journal C*, 74:2938, 2014.

[35] V. Aynutdinov et al. Search for relativistic magnetic monopoles with the baikal neutrino telescope. *Astropart. Phys.*, 29:366, 2008.

[36] B. et al. Acharya. Search for magnetic monopoles with the moedal forward trapping detector in 13 tev proton-proton collisions at the lhc. *Physical Review Letters*, 118:061801, 2017.

[37] V. A. Rubakov. Adler-bell-jackiw anomaly and fermion number breaking in the presence of a magnetic monopole. *Nuclear Physics B*, 203:311–348, 1982.

[38] Curtis G. Callan Jr. Monopole catalysis of baryon decay. *Nuclear Physics B*, 212:391–400, 1983.

[39] S. Dawson and A. N. Schellekens. Monopole catalysis of proton decay in so(10) grand unified models. *Phys. Rev. D*, 27:2119–2128, May 1983.

[40] T.F. Walsh, P. Weisz, and Tai Tsun Wu. Monopole catalysis of proton decay. *Nuclear Physics B*, 232(2):349–355, 1984.

[41] W. W. M. Allison et al. Search for proton decay via magnetic monopole catalysis in the soudan detector. *Phys. Rev. D*, 31:140, 1985.

[42] R. Becker-Szendy et al. New magnetic monopole flux limits from the imb proton decay detector. *Phys. Rev. D*, 49:2169–2173, Mar 1994.

[43] T. Kajita et al. Search for nucleon decay catalyzed by magnetic monopoles in kamiokande. *Physical Review D*, 42:366–372, 1990.

[44] M. Ambrosio et al. Search for nucleon decays induced by gut magnetic monopoles with the macro experiment. *The European Physical Journal C*, 26(2):163–172, December 2002.

[45] M. G. Aartsen et al. (IceCube Collaboration). Search for non-relativistic magnetic monopoles with icecube. *Eur. Phys. J. C*, 74:2938, 2014.

[46] K. Choi et al. (Super-Kamiokande Collaboration). Search for gut monopoles at super-kamiokande. *Phys. Rev. D*, 88:052002, 2013.

[47] E. N. Parker. The origin of magnetic fields. *Astrophysical Journal*, 160:383–404, 1970.

[48] Fred C. Adams, Marco Fatuzzo, Katherine Freese, Gregory Tarlé, Richard Watkins, and Michael S. Turner. Extension of the parker bound on the flux of magnetic monopoles. *Phys. Rev. Lett.*, 70:2511–2514, Apr 1993.

[49] S. Orito et al. Search for supermassive magnetic monopoles with plastic track detectors. *Physical Review Letters*, 66:1951–1954, 1991.

[50] Yu. F. Novoseltsev et al. Search for magnetic monopoles with the baksan underground scintillation telescope. *Nuclear Physics B (Proc. Suppl.)*, 151:337–340, 2006.

[51] J. L. Thron et al. (Soudan 2 Collaboration). Search for nucleon decay and magnetic monopoles with the soudan 2 detector. *Physical Review D*, 46:4846–4854, 1992.

[52] M. R. Krishnaswamy et al. Search for magnetic monopoles at the kolar gold fields experiment. *Physics Letters B*, 142:99–102, 1984.

[53] V. Aynutdinov et al. Search for relativistic magnetic monopoles with the baikal neutrino telescope. *Astroparticle Physics*, 29:366, 2008.

[54] R. Abbasi et al. Search for relativistic magnetic monopoles with the amanda-ii detector. *European Physical Journal C*, 69:361–378, 2010.

[55] S. Adrián-Martínez et al. (ANTARES Collaboration). Search for relativistic magnetic monopoles with the antares neutrino telescope. *Astroparticle Physics*, 35:634–640, 2012.

[56] R. Abbasi et al. (IceCube Collaboration). Search for relativistic magnetic monopoles with icecube. *Physical Review D*, 87:022001, 2013.

[57] A. Drukier and S. Nussinov. Monopole pair creation in energetic collisions: Is it possible? *Physical Review Letters*, 49:102–105, 1982.

[58] Y. M. Cho and D. Maison. Monopole configuration in weinberg-salam model. *Physics Letters B*, 391:360–365, 1997.

[59] K. Kimm, J. H. Yoon, and Y. M. Cho. Finite energy electroweak dyon. *European Physical Journal C*, 75:67, 2015.

[60] J. Ellis, N. E. Mavromatos, and T. You. The price of an electroweak monopole. *Physics Letters B*, 756:29–35, 2016.

[61] Y. M. Cho, K. Kimm, and J. H. Yoon. Gravitationally coupled electroweak monopole. *Physics Letters B*, 761:203–208, 2016.

[62] G. Aad et al. (ATLAS Collaboration). Search for magnetic monopoles in $\sqrt{s} = 7$ tev pp collisions with the atlas detector. *Phys. Rev. Lett.*, 109:261803, 2012.

[63] B. Acharya et al. Search for highly ionizing particles in pp collisions during lhc run 2 using the full moedal detector. *Phys. Rev. Lett.*, 134:071802, Feb 2025.

[64] A. Abulencia et al. (CDF Collaboration). Direct search for dirac magnetic monopoles in $p\bar{p}$ collisions. *Physical Review Letters*, 96:201801, 2006.

[65] B. Abbott et al. (D0 Collaboration). Search for magnetic monopoles in $p\bar{p}$ collisions. *Physical Review Letters*, 81:524–529, 1998.

[66] M. Bertani et al. Search for magnetic monopoles at the fermilab tevatron using nuclear track detectors. *Europhysics Letters*, 12:613–618, 1990.

[67] G. Abbiendi et al. (OPAL Collaboration). Search for dirac magnetic monopoles in e^+e^- collisions with the opal detector at lep2. *Phys. Lett. B*, 663:37–42, 2008.

[68] K. Kinoshita et al. Search for highly ionizing particles in e^+e^- collisions. *Physical Review D*, 46:R881–R884, 1992.

[69] K. Kinoshita et al. Search for highly ionizing particles at high-energy colliders. *Physics Letters B*, 228:543–548, 1989.

[70] P. Musset et al. Search for magnetic monopoles in e^+e^- collisions at petra. *Physics Letters B*, 128:333–338, 1983.

[71] D. Fryberger, T. Coan, K. Kinoshita, and P. B. Price. Search for highly ionizing particles in high-energy collisions. *Physical Review D*, 29:1524–1535, 1984.

[72] A. Aktas et al. (H1 Collaboration). A direct search for stable magnetic monopoles produced in positron-proton collisions at hera. *Eur. Phys. J. C*, 41:133–141, 2005.

[73] A. Aktas et al. (H1 Collaboration). Search for magnetic monopoles in ep collisions at hera. *European Physical Journal C*, 41:133–141, 2005.

[74] G. R. Kalbfleisch et al. Limits on production of magnetic monopoles utilizing samples from the d0 and cdf detectors at the fermilab tevatron. *Phys. Rev. D*, 69:052002, 2004.

[75] A Norman. The nova data acquisition system. *Journal of Physics: Conference Series*, 396(1):012035, dec 2012.

[76] A. Norman et al. Performance of the NOνA Data Acquisition and Trigger Systems for the full 14 kT Far Detector. *J. Phys. Conf. Ser.*, 664:082041, 2015.

[77] M Fischler, C Green, J Kowalkowski, A Norman, M Paterno, and R Rechenmacher. Nova event building, buffering and data-driven triggering from within the daq system. *Journal of Physics: Conference Series*, 396(1):012020, dec 2012.

[78] Donald E. Groom. Magnetic monopole search. *Physics Reports*, 140(6):323–342, 1986.

[79] Steven P. Ahlen. Stopping power of magnetic monopoles. *Physical Review D*, 17(1):229–233, 1978.

[80] Steven P. Ahlen. The calculation of the stopping power of very heavy ions. *Reviews of Modern Physics*, 52(1):121–173, 1980.

[81] S. Agostinelli et al. Geant4—a simulation toolkit. *Nuclear Instruments and Methods in Physics Research Section A*, 506(3):250–303, 2003.

[82] J. B. Birks. The theory and practice of scintillation counting. *Proceedings of the Physical Society. Section A*, 64(10):874–877, 1951.

[83] C. N. Chou. The nature of the saturation effect of fluorescent scintillators. *Physical Review*, 87(5):904–905, 1952.

[84] N. Anfimov, A. Antoshkin, A. Aurisano, O. Samoylov, and A. Sotnikov. Simulation of light production and propagation in the nova detector. *Journal of Instrumentation*, 15:C06066, 2020.

[85] I. Frank and Ig. Tamm. *Coherent Visible Radiation of Fast Electrons Passing Through Matter*. Springer Berlin Heidelberg, Berlin, Heidelberg, 1991.

[86] D. R. Tompkins. Total energy loss and cherenkov emission from monopoles. *Physical Review*, 138(2A):A248–A252, 1965.

[87] M. J. Berger. ESTAR, PSTAR, and ASTAR: Computer programs for calculating stopping-power and range tables for electrons, protons, and helium ions, December 1992.

[88] M. A. Acero et al. Search for slow magnetic monopoles with the nova detector on the surface. *Phys. Rev. D*, 103:012007, Jan 2021.

[89] J. Derkaoui, G. Giacomelli, T. Lari, A. Margiotta, M. Ouchrif, L. Patrizii, V. Popa, and V. Togo. Energy losses of magnetic monopoles and of dyons in the earth. *Astroparticle Physics*, 9(2):173–183, 1998.

[90] Edward Witten. Cosmic Separation of Phases. *Phys. Rev. D*, 30:272–285, 1984.

[91] J. D. Bjorken and L. D. McLerran. Explosive quark matter and the ”centauro” event. *Phys. Rev. D*, 20:2353–2360, Nov 1979.

[92] A. Chodos, R. L. Jaffe, K. Johnson, C. B. Thorn, and V. F. Weisskopf. New extended model of hadrons. *Phys. Rev. D*, 9:3471–3495, Jun 1974.

[93] Nima Arkani–Hamed, Savas Dimopoulos, and Gia Dvali. The hierarchy problem and new dimensions at a millimeter. *Phys. Lett. B*, 429(3–4):263–272, June 1998.

[94] Philip C. Argyres, Savas Dimopoulos, and John March-Russell. Black holes and sub-millimeter dimensions. *Phys. Lett. B*, 441(1–4):96–104, November 1998.

[95] Roberto Emparan, Gary T. Horowitz, and Robert C. Myers. Black holes radiate mainly on the brane. *Phys. Rev. Lett.*, 85(3):499–502, July 2000.

[96] W. Pauli. Letter to the physical society of t”ubingen. 1930.

[97] Sheldon L. Glashow. Partial-symmetries of weak interactions. *Nucl. Phys.*, 22:579–588, 1961.

[98] Steven Weinberg. A model of leptons. *Phys. Rev. Lett.*, 19:1264–1266, 1967.

[99] Abdus Salam. Weak and electromagnetic interactions. In N. Svartholm, editor, *Elementary Particle Theory: Relativistic Groups and Analyticity*, volume 8 of *Proceedings of the Nobel Symposium*, pages 367–377, Stockholm, 1968. Almqvist and Wiksell.

[100] Y. Fukuda et al. Evidence for oscillation of atmospheric neutrinos. *Phys. Rev. Lett.*, 81:1562–1567, 1998.

[101] Y. Fukuda et al. Measurement of the solar neutrino energy spectrum using neutrino-electron scattering. *Phys. Rev. Lett.*, 81:1158–1162, 1998.

[102] Q. R. Ahmad et al. (SNO Collaboration). Direct evidence for neutrino flavor transformation from neutral-current interactions in the sudbury neutrino observatory. *Phys. Rev. Lett.*, 89:011301, 2002.

[103] K. Eguchi et al. (KamLAND Collaboration). First results from kamland: Evidence for reactor antineutrino disappearance. *Phys. Rev. Lett.*, 90:021802, 2003.

[104] M. H. Ahn et al. Indications of neutrino oscillation in a 250-km long-baseline experiment. *Phys. Rev. Lett.*, 90:041801, 2003.

[105] S. Fukuda et al. The super-kamiokande detector. *Nucl. Instrum. Meth. A*, 501:418–462, 2003.

[106] M. G. Aartsen et al. First observation of pev-energy neutrinos with icecube. *Phys. Rev. Lett.*, 111(2):021103, 2013.

[107] K. Eguchi et al. First results from kamland: Evidence for reactor anti-neutrino disappearance. *Phys. Rev. Lett.*, 90:021802, 2003.

[108] G. Alimonti et al. The borexino detector at the laboratori nazionali del gran sasso. *Nucl. Instrum. Meth. A*, 600:568–593, 2009.

[109] M. A. Acero et al. First measurement of neutrino oscillation parameters using neutrinos and antineutrinos by nova. *Phys. Rev. Lett.*, 123:151803, 2019.

[110] S.andothers Amerio. Performanceoftheicarust600liquidargontimeprojectionchamberattheundergrou *Nucl.Instrum.Meth.A*, 527:329–410, 2004.

[111] B. Abi et al. Deep underground neutrino experiment (dune), far detector technical design report, volume i: Introduction to dune. *JINST*, 15(08):T08008, 2020.

[112] B. T. Cleveland et al. Measurement of the solar electron neutrino flux with the homestake chlorine detector. *Astrophys. J.*, 496:505–526, 1998.

[113] J. N. Abdurashitov and title = others.

[114] D. Akimov et al. Observation of coherent elastic neutrino-nucleus scattering. *Science*, 357(6356):1123–1126, 2017.

[115] B. Pontecorvo. Mesonium and antimesonium. *Zh. Eksp. Teor. Fiz.*, 33:549–551, 1957. [Sov. Phys. JETP 6 (1958) 429].

[116] Z. Maki, M. Nakagawa, and S. Sakata. Remarks on the unified model of elementary particles. *Prog. Theor. Phys.*, 28:870–880, 1962.

[117] R. Davis, D. S. Harmer, and K. C. Hoffman. Search for neutrinos from the sun. *Phys. Rev. Lett.*, 20:1205–1209, 1968.

[118] J.N. Bahcall. Neutrino astrophysics. *Cambridge University Press*, 1989.

[119] Takaaki Kajita. Nobel lecture: Discovery of atmospheric neutrino oscillations. *Rev. Mod. Phys.*, 88:030501, 2016.

[120] D. Adey et al. Measurement of the Electron Antineutrino Oscillation with 1958 Days of Operation at Daya Bay. *Phys. Rev. Lett.*, 121:241805, 2018.

[121] G. Bak et al. Measurement of Reactor Antineutrino Oscillation Amplitude and Frequency at RENO. *Phys. Rev. Lett.*, 121:201801, 2018.

[122] Y. Abe et al. Double Chooz θ13 measurement via total neutron capture detection. *Nature Phys.*, 16:558–564, 2020.

[123] M. H. Ahn et al. Indications of neutrino oscillation in a 250-km long-baseline experiment. *Phys. Rev. Lett.*, 90:041801, 2003.

[124] P. Adamson et al. Measurement of neutrino oscillations with the minos detectors in the numi beam. *Phys. Rev. Lett.*, 101:131802, 2008.

[125] K. Abe et al. Indication of electron neutrino appearance from an accelerator-produced off-axis muon neutrino beam. *Phys. Rev. Lett.*, 107:041801, 2011.

[126] B. Abi et al. Deep underground neutrino experiment (dune), far detector technical design report, volume ii: Dune physics. *JINST*, 15:T08010, 2020.

[127] K. Abe et al. Hyper-Kamiokande Design Report. *arXiv:1805.04163*, 2018.

[128] V. N. Gribov and B. Pontecorvo. Neutrino astronomy and lepton charge. *Phys. Lett. B*, 28:493, 1969.

[129] Ziro Maki, Masami Nakagawa, and Shoichi Sakata. Remarks on the unified model of elementary particles. *Prog. Theor. Phys.*, 28:870–880, 1962.

[130] S. M. Bilenky and B. Pontecorvo. Lepton mixing and neutrino oscillations. *Phys. Rept.*, 41:225–261, 1978.

[131] Carlo Giunti and Chung W. Kim. *Fundamentals of Neutrino Physics and Astrophysics*. Oxford University Press, Oxford, UK, 2007.

[132] S. P. Mikheyev and A. Yu. Smirnov. Resonance Amplification of Oscillations in Matter and Spectroscopy of Solar Neutrinos. *Sov. J. Nucl. Phys.*, 42:913–917, 1985.

[133] L. Wolfenstein. Neutrino oscillations in matter. *Phys. Rev. D*, 17:2369–2374, 1978.

[134] ”Nötzold, D. and Raffelt, G. G. Neutrino Dispersion at Finite Temperature and Density. *Nucl. Phys. B*, 307:924–936, 1988.

[135] B. Aharmim et al. Combined Analysis of all Three Phases of Solar Neutrino Data from the Sudbury Neutrino Observatory. *Phys. Rev. C*, 88:025501, 2013.

[136] K. Abe et al. Solar Neutrino Measurements in Super-Kamiokande-IV. *Phys. Rev. D*, 94:052010, 2016.

[137] M. Agostini et al. Spectroscopy of geoneutrinos from 2056 days of Borexino data. *Phys. Rev. D*, 101:012009, 2020.

[138] S. Abe et al. Precision Measurement of Neutrino Oscillation Parameters with KamLAND. *Phys. Rev. Lett.*, 100:221803, 2008.

[139] F. An et al. Neutrino Physics with JUNO. *J. Phys. G*, 43:030401, 2016.

[140] K. Abe et al. Atmospheric Neutrino Oscillation Analysis with External Constraints in Super-Kamiokande I–IV. *Phys. Rev. D*, 97:072001, 2018.

[141] M. G. Aartsen et al. Measurement of Atmospheric Neutrino Oscillations at 6–56 GeV with IceCube DeepCore. *Phys. Rev. Lett.*, 120:071801, 2018.

[142] S. Adrian-Martinez et al. Letter of intent for KM3NeT 2.0. *J. Phys. G*, 43:084001, 2016.

[143] K. Abe et al. Constraint on the matter–antimatter symmetry-violating phase in neutrino oscillations. *Nature*, 580:339–344, 2020.

[144] M. A. Acero et al. An Improved Measurement of Neutrino Oscillation Parameters by the NOvA Experiment. *Phys. Rev. D*, 106:032004, 2022.

[145] B. Abi et al. Long-Baseline Neutrino Facility (LBNF) and Deep Underground Neutrino Experiment (DUNE). *JINST*, 15:T08008, 2020.

[146] Stefano Dell'Oro, Simone Marcocci, Matteo Viel, and Francesco Vissani. Neutrinoless double beta decay: 2015 review. *Adv. High Energy Phys.*, 2016:2162659, 2016.

[147] K. Abe et al. Constraint on the matter–antimatter symmetry-violating phase in neutrino oscillations. *Nature*, 580:339–344, 2020.

[148] Tommy Ohlsson. Status of non-standard neutrino interactions. *Rept. Prog. Phys.*, 76:044201, 2013.

[149] Shao-Feng Ge and Stephen J. Parke. Scalar nonstandard interactions in neutrino oscillation. *Phys. Rev. Lett.*, 122(21):211801, 2019.

[150] Yasaman Farzan and Mariam Tortola. Neutrino oscillations and non-standard interactions. *Front. in Phys.*, 6:10, 2018.

[151] Dinesh Kumar Singha, Rudra Majhi, Lipsarani Panda, Monojit Ghosh, and Rukmani Mohanta. Study of scalar non standard interaction at protvino to super-orca experiment. *Phys. Rev. D*, 2024.

[152] K. S. Babu, Garv Chauhan, and P. S. Bhupal Dev. Neutrino nonstandard interactions via light scalars in the earth, sun, supernovae, and the early universe. *Phys. Rev. D*, 101:095029, May 2020.

[153] P. Huber, M. Lindner, and W. Winter. Simulation of long-baseline neutrino oscillation experiments with globes (general long baseline experiment simulator). *Comput. Phys. Commun.*, 167:195–202, 2005.

[154] P. Huber, J. Kopp, M. Lindner, M. Rolinec, and W. Winter. New features in the simulation of neutrino oscillation experiments with globes 3.0: General long baseline experiment simulator. *Comput. Phys. Commun.*, 177:432–438, 2007.

[155] DUNE Collaboration. Deep underground neutrino experiment (dune) conceptual design report. Technical report, 2015. Available at: https://dune.bnl.gov or the DUNE document database.

[156] DUNE Collaboration. Deep underground neutrino experiment (dune) technical design report. Technical report, 2020. CERN Yellow Reports: Monographs, CERN-2020-XXX; arXiv:2002.XXX [physics.ins-det].

[157] G. L. Fogli, E. Lisi, A. Marrone, D. Montanino, and A. Palazzo. Getting the most from the statistical analysis of solar neutrino oscillations. *Phys. Rev. D*, 66:053010, 2002.

[158] Patrick Huber, Manfred Lindner, and Walter Winter. Superbeams versus neutrino factories. *Nucl. Phys. B*, 645:3–48, 2002.